On the Structure of Premixed Flames Subjected to Extreme Levels of Turbulence

by

Aaron William Skiba

A dissertation submitted in partial fulfillment
of the requirements for the degree of
Doctor of Philosophy
(Aerospace Engineering)
in The University of Michigan
2017

Doctoral Committee:

Professor James F. Driscoll, Chair
Dr. Campbell D. Carter, Air Force Research Laboratory
Assistant Professor Mirko Gamba
Associate Professor Venkat Raman
Professor Volker Sick

Aaron W. Skiba

skiba@umich.edu

ORCID iD: 0000-0001-8494-4372

For my parents,

their unwavering love and support is the ground upon which these efforts rest.

ACKNOWLEDGEMENTS

Properly acknowledging each individual who has in some way influenced, facilitated, and/or helped with the efforts presented in this dissertation would undoubtedly increase its length tenfold. For the sake of brevity and practicality, I will restrain from composing such a comprehensive acknowledgement section. Therefore, I apologize in advance if your name is not explicitly mentioned here. However, do know that if our paths have ever crossed it is likely that you have, in some fashion, positively influenced these efforts, and for that I am grateful.

I must begin by thanking my dissertation committee, for without their guidance, expertise, and willingness to carefully read and critique this dissertation, it would not have been brought to fruition. Professor Sick, though our interactions have been minimal, I certainly appreciate the sacrifice in time and energy you have made to be a part of my committee. Moreover, I am grateful for your comments and suggested edits to this work; incorporating them into this dissertation has undoubtedly rendered it superior. Professor Raman, I have truly enjoyed each of our many conversations on turbulence, combustion, and modeling. The insights and understanding I have acquired from you have shaped a significant portion of this dissertation, and they will, without question, assist me with my future endeavors. I firmly believe that close relationships between numerical and experimental combustion scientists are essential to the advancement of our field. Thus, I hope that we can continue our conversations long into the future and perhaps even establish a research collaboration one day. Professor Gamba, no one has challenged me more than you have, and that, without a

doubt, has made me a better scientist. You were always willing to hear my questions and difficulties and subsequently, you always provided me with guidance and direction on how to obtain the answers I sought. I am sincerely grateful for all your efforts and for all that you have taught me.

A substantial portion of the work presented in this dissertation would not have been possible without my 4th committee member, Dr. Campbell D. Carter (i.e. Cam). Cam, I will never be able to thank you enough for all the time and effort you have put in to help me with this work. Over the past two years you have 1) thoroughly read portions of this dissertation several times over; 2) provided innumerous and invaluable pieces of advice; 3) allowed me to invade and essentially take over your lab for weeks on end; 4) taught me an endless array of diagnostic tricks and details; and so on and so on. Moreover, you have been a mentor and a friend. Regardless of whether the topic was diagnostics, research, politics, or something as simple as the best shows on Netflix, I have always enjoyed conversing with you. You are an amazing researcher and scientist, and I aspire to be as dedicated and as passionate as you are towards your research. Yet, more importantly, I aim to be as humble and generous as you are towards others. Thank you, so very much, Cam. I hope that our collaborations continue for many years to come.

The final member of my committee most definitely deserves my sincerest gratitude. In my mind, Professor Driscoll, you are without a doubt the best advisor a Ph.D. student could ever ask for. You have allowed me to design, propose, and partake in multiple research campaigns, and all the while you provided suggestions and guidance in a manner that has allowed me to become a free thinking combustion scientist. Your tactic for motivating me to work (whether intentional or not) never came in the form of a stern or a harsh warning. Instead, I was always motivated by a desire to impress you and subsequently to impress the entire combustion science community. I certainly cannot list the vast amounts of information I have learned from you over the past 5

years. But I will say that the most important thing you have taught me is how to be an excellent mentor. Your door was always open and you were always willing to listen and weigh in on whatever challenges I was facing. Whether I was struggling with difficulties in the lab or with identifying the most appropriate way to define the turbulent Karlovitz number, you were always there to help and to teach. It might be cheesy, but I must admit that our conversations on turbulence, combustion, and the future of our field are some of the best that I have ever had, and I look forward to many more of them in the days ahead. So thank you again, Professor Driscoll, it has truly been an honor being your student.

Beyond my committee, there are many other scientists and researchers that require my gratitude. Dr. Timothy M. Wabel tops the list, for without his assistance in the lab much of this work would not have been accomplished as efficiently as it was. So for all your efforts, Tim, thank you. Dr. Jacob E. Temme, without your guidance and experience in the lab it would have taken many more years for me to complete the research presented in this dissertation. So thank you for being a patient mentor to a young graduate student, and for trusting me with delicate and expensive experimental equipment. My first mentor as a combustion researcher, Dr. Matthew Fotia, also deserves my gratitude. Thank you for acquainting me with the lab, Matt, and for designing the majority of the burner used to conduct the research presented in this dissertation. Though only a portion of the data I helped gather at Wright Patterson Air Force Base is presented in this dissertation, I must thank Dr. Stephen D. Hammack for all of his assistance with setting up and performing multiple, highly-complex experiments. I would also like to thank Professor Brian K. Arbic for taking me on as an undergraduate student research assistant. The opportunity to study tides incited my passion for research and my desire to elucidate the unknown. Thus, I often identify that opportunity as the primary motivator for my decision to pursue a Ph.D. and to continue to conduct research. So again, thank you Professor Arbic

for allowing me to be a part of your research group for a time.

To the numerous and ever helpful staff associated with the FXB, thank you. In particular, I am grateful for all the help and assistance that I have received from Denise Phelps, Tom Griffin, Chris Chartier, Eric Kirk, Dave McLean, Aaron Borgman, and last but certainly not least Terry Larrow. Your efforts have facilitated a great deal of the work presented here, and I know that many former (and future) graduate students would have been (would be) lost without you. So know that your work is highly appreciated. Furthermore, I must thank my fellow Ph.D. students: Chuky Mbagwa, Kyle Hanquist, Horatiu Dragnea, (former student) Yuntao Chen, Robert Zidek, Yasin Abul-Huda, Robin Hunt, Rohan Morajkar, Chris Marley, Logan White, Jacob France, Fabian Chacon, and our dearest friend, Abhinav Dasari, may you rest in peace. Each of you have helped me in some way or another, for which I am grateful. Additionally, know that without your comradery and fellowship, the last five years would have certainly been much more of a struggle.

Of course, outside of research and academia there are many individuals I am grateful for. To my high school chemistry teachers, Mrs. Ellsen Diamond and Mrs. Jennifer Poli, thank you for being such great instructors and instilling within me a passion for science and a desire to share my knowledge with others. One of my favorite quotes, which is by Henry Adams, is, "A teacher affects eternity; he [she] can never tell where his [her] influence stops." Your influence has brought me here, and it will undoubtedly lead me to other achievements in the future. So I thank and commend you for all the time you put in and all the effort you expend to be such amazing teachers.

In addition to the excellent teachers, mentors, and advisors I have, I am most fortunate to have many wonderful friendships. To Robert Carter, Curt Kaiser, Jared Patterson, Brenten Kelly, and to so many other loyal friends from high school, thank you for some of the most memorable times of my life. Though we may not see each

other on a regular basis, I think about you guys often and I am thankful to be able to call each of you, my friend. I have made many great friends during college as well. Thank you, Anuj Shah, Robert (Roe) Burrell, DJ Lee, Ben Williams, Ian Spiers, Liam Scott, Evan Collins, Trevor Nutt, Evan Rosen, Aaron Sochacki, Todd Holden, Will Wimbrow, and many others for all the fun times we have shared together. To one of my best friends, Nick Olson, thank you for being by my side during both good times and bad over the past 10 years. I certainly hope that we can stay close for many years to come and I am already looking forward to your visit(s) to Cambridge. To my other best friend, (soon to be Professor) Patton Allison, thank you for not only being a close friend but also for being a great mentor over these past five years. I struggle to comprehend the fact that we have only known each other for such a short time. To me, it feels as though we have been close companions for multiple decades. We have shared many wonderful experiences together, and I know that there are many more in store for us.

To my dearest friend, partner in crime, and love of my life – Ellen – I will never be able to express enough gratitude for the help and support you have given me and the love you have shown me throughout these efforts. I do not think I could have accomplished this without you by my side to comfort my anxieties and fears; that is, without you, it is quite likely that I would have gone mad long before reaching this point. I cannot stress enough how unbelievably helpful it has been to have someone to talk to who has been through all this already. As a simple example, your assistance with LaTeX alone likely saved me countless hours of agony and frustration. Yet most of all, I must thank you for having confidence in me, especially when I had little to none in myself. For all that you have done, and for all that you do, Ellen, I am grateful and I love you so very much.

Finally, I must thank my family, for without them none of this would have been possible. As many of you reading this may know, I have a massive extended family

(e.g. +60 first cousins). Thus, I will only explicitly acknowledge my closest family members. So to all of my relatives that I do not mention, thank you for your never failing support. I would like to start by thanking my grandparents, Anthony and Agnes Skiba. Though you are no longer with us on Earth, the love and faith you shared with me during our brief time together certainly impacted my life in positive ways. To my grandmother, Diana Hale-Dean, thank you so very much for all your love, support, and kindness and for all the wonderful celebrations you have hosted over the years. The endless array of joyous memories I have from all the times our families have gathered certainly helped to curb the stress I endured whilst composing this dissertation. To my grandfather, William Aaron Hale ("Gramps"), thank you for your love and support as well. You have always pushed me to be my best and your faith in me has never faltered, and for that, I am truly thankful. To Alex, my brother and my friend, thank you for being there for me as well. You always know how to bring a smile to my face and I cannot even begin to count all of the wonderful and exciting adventures we have had together. Though we have not always seen eye-to-eye, I now consider you as one of my best friends; I love you brother.

Last but not least, in fact, most of all, I must thank my parents, Richard and Christina Skiba. The countless sacrifices you have made to see me through to this point, are beyond my comprehension. Yet, I appreciate each and every one of them. Your unconditional love and support is the foundation I have depended upon throughout my entire life, and in its absence, I would not be the man I am today. You raised me to be kind, patient, polite, and respectful and you always encouraged me to pursue my dreams, even if that meant playing with fire. There is no doubt in my mind that the upbringing you gave me and the perpetual love you show me will lead me to many successes in the future. I cannot even begin to describe how blessed I am to have you as parents. The world would be a much better place if there were more parents like you in it. And you should know that one of my deepest aspirations in

life is to be as great of a parent as you are some day. Mom and Dad, thank you so incredibly much, I love you dearly.

TABLE OF CONTENTS

LIST OF FIGURES

Figure

LIST OF TABLES

Table

LIST OF APPENDICES

Appendix

LIST OF ABBREVIATIONS

Acronym

AFRL	Air Force Research Laboratory
BP-TR	Broadened Preheat – Thin Reaction Zones Regime
CMOS	Complementary Metal-Oxide Semiconductor
DNS	Direct Numerical Simulation
FLOPS	Floating Point Operations Per Second
FOV	Field of View
FSD	Flame Surface Density
FWHM	Full Width at Half Maximum
HIT	Homogeneous Isotropic Turbulence
HRR	Heat Release Rate
HS-IRO	High-Speed ICCD Relay Optics
ICCD	Intensified Charge-Coupled Device
LDV	Laser Doppler Velocimetry
LES	Large-Eddy Simulation
LIF	Laser-Induced Fluorescence
LSF	Line Spread Function
OL	Overlap
PACE	Propulsion and Combustion Engineering Laboratory
PDF	Probability Density Function
PH	Preheat Zone

PLIF	Planar Laser-Induced Fluorescence
PMT	Photomultiplier Tube
PSF	Point Spread Function
RANS	Reynolds-Averaged Navier-Stokes
RMS	Root Mean Square
SNR	Signal to Noise Ratio
SRF	Step Response Function
TKE	Turbulent Kinetic Energy
UHC	Un-burned Hydrocarbons
UV	Ultra-Violet

LIST OF SYMBOLS

Latin Symbols

a	Refractivity Constant taken from Gardiner et al. [38]
b	Refractivity Constant taken from Gardiner et al. [38]
c	Progress Variable
c_p	Specific Heat Capacity
C_{opt}	Constant Corresponding to the Optical Efficiency of an Imaging System
D^*	Characteristic Molecular Diffusivity defined by Peters [1, 36]
D_T	Turbulent Diffusivity
Da_T	Turbulent Damköhler Number
E_L	Laser Energy Ratio
I	Signal Intensity or an Intensity Image
k	Boltzmann Constant
Ka_T	Turbulent Karlovitz Number
L	Integral Length Scale
ℓ	Characteristic Length Scale
N_0	Number Density
N_x	Number of Computation Grid Points in One Direction
n_0	Index of Refraction
P	Pressure
Re_T	Turbulent Reynolds Number

T	Temperature
T_p	Product gas Temperature
U_0	Mean Centerline Velocity
u'	RMS of the Velocity Fluctuations in the Axial Direction

Greek Symbols

α	Flame Crossing Angle
δ	Represents the Thickness of a Particular Layer
Δ_L	Ensemble-Averaged Flame Front Length
Δx	Interogation Box Size for FSD Measurements
Δ_x	Computational Grid Size in One Direction
δt_i	Time Step Between a Discreet Numerical Integration Step
δx_{gp}	Distance Between Computational Grid Points
ϵ	Dissipation Rate of Turbulent Kinetic Energy
η	Kolmogorov Length Scale
η^*	Kolmogorov Length Scale Based on a Kinematic Viscosity Evaluated at a Reaction Layer Temperature (ν^*)
λ_{th}	Thermal Conductivity
λ	Wavelength of Laser Light
ν	Kinematic Viscosity
ν^*	Kinematic Viscosity Evaluated at a Reaction Layer Temperature
ρ	Density
ρ_ν	*Depolarization* Value
Σ	Flame Surface Density
σ	Differential Rayleigh Scattering Cross-Section
σ_{sd}	Standard Deviation
τ	Characteristic Time Scale

τ_{η^*}	Kolmogorov Time Scale Based on a Kinematic Viscosity Evaluated at a Reaction Layer Temperature (ν^*)
ϕ	Equivalence Ratio
χ	Species Mole Fraction
Ω	Flame Wrinkling Parameter

Subscripts

0	Indicates that the Parameter was Evaluated at a Reactant Temperature
$2D$	Indicates a 2-Dimensional Quantity
$3D$	Indicates a 3-Dimensional Quantity
A	Indicates a General Parameter Associated with Air
D	Indicates a Dark Background Image
e	Indicates an Expected Signal Intensity (Void of Background Signal
F	Indicates a General Parameter Associated with a Flame
FB	Indicates a Flame Background Image
inc	Indicates Incident Laser Light Intensity
L	Indicates a Parameter Associated with a Laminar Flame
ℓ	Indicates a Parameter Evaluated at a Characteristic Length Scale
LB	Indicates a Laser Background Image
LS	Indicates a Parameter Associated with a Laser Sheet
mix	Indicates a Parameter Based on a Mixture of Gasses
MP	Most Probable (Peak value of a PDF)
OL	Overlap
P	Indicates that the Parameter was based on Peters' Definition [1, 36]
PH	Indicates a Parameter Associated with the Preheat Zone
R	Indicates that the Parameter was Evaluated at a Reaction Layer Temperature
r	Indicates that the Parameter was Evaluated in the Radial Direction

raw	Indicates an Image with no Processing Applied
Ray	Indicates an Image or Intensity Level of Rayleigh Scattering Signal
ref	Indicates that the Image or Value was Obtained from a Reference Case
RL	Indicates a Parameter Associated with a General Reaction Layer
RZ	Indicates a Parameter Associated with the Reaction Zone
S	Indicates an Image or Intensity Level of Laser Light Scattering
SC	Indicates a Laser Sheet Correction Image
th	Indicates a Thickness based on Temperature (Thermal Thickness)
VH	Indicates a Rayleigh Scattering Cross Section Associated with Vertically Polarized Indecent Laser Light and Horizontally Polarized Scattered Signal
VV	Indicates a Rayleigh Scattering Cross Section Associated with Vertically Polarized Indecent Laser Light and Scattered Signal
x	Indicates that the Parameter was Evaluated in the Axial Direction

Mathematical Operators

$(\bar{\cdot})$	Temporal or Ensemble Average
$\sum_i$	Summation over i
∇	Differential Operator

ABSTRACT

On the Structure of Premixed Flames Subjected to Extreme Levels of Turbulence

by

Aaron W. Skiba

Chair: Professor James F. Driscoll

Developing next-generation propulsion and energy production devices that are efficient, cost-effective, and generate little to no harmful emissions will require highly-accurate, robust, yet computationally tractable turbulent combustion models. Models that accurately simulate turbulent premixed combustion problems are particularly important due to the fact that burning in a premixed mode can reduce exhaust emissions. A common tool employed to identify when a particular model might be more appropriate than others is the theoretical Borghi Diagram, which possesses boundaries that are meant to separate various regimes of combustion (i.e. where a particular model is superior to others). However, the derivations of these boundaries are merely based upon intuition and dimensional reasoning, rather than experimental evidence. This thesis aims to provide such evidence; furthermore, it proposes novel approaches to delineating regimes of combustion that are consistent with experimental results.

To this end, high-fidelity flame structure measurements were applied to premixed methane–air Bunsen flames subjected to extreme levels of turbulence. Specifically, 28 cases were studied with turbulence levels (u'/S_L) as high as 246, longitudinal integral length scales (L_x) as large as 43 mm, and turbulent Karlovitz (Ka_T) and Reynolds

(Re_T) numbers up to 533 and 99,000, respectively. Two techniques were employed to measure the preheat and reaction layer thicknesses of these flames. One consisted of planar laser-induced fluorescence (PLIF) imaging of CH radicals, while the other involved taking the product of simultaneously acquired PLIF images of formaldehyde (CH_2O) and hydroxyl (OH) to produce "overlap-layers." Average preheat layer thicknesses are found to increase with increasing u'/S_L and with axial distance from the burner (x/D). In contrast, average reaction layer thicknesses did not vary appreciably with either u'/S_L or x/D. The reaction layers are also observed to remain continuous; that is, local extinction events are rarely observed. The results of this study, as well as those from prior investigations, display inconsistencies with predictions made by the theoretical Borghi Diagram. Therefore, a new Measured Regime Diagram is proposed wherein the Klimov-Williams criterion is replaced by a metric that relates the turbulent diffusivity ($D_T = u'L$) to the molecular diffusivity within the preheat layer ($D^* = S_L\delta_{F,L}$). Specifically, the line defined by $D_T/D^* \approx 180$ does a substantially better job of separating thin flamelets from those with broadened preheat yet thin reaction layers (i.e. BP-TR flames). Additionally, the results suggest that the BP-TR regime extends well beyond what was previously theorized since neither broken nor broadened reaction layers were observed under conditions with Karlovitz numbers as high as 533. Overall, these efforts provide tremendous insights into the fundamental properties of extremely turbulent premixed flames. Ultimately, these insights will assist with the development and proper selection of accurate and robust numerical models.

CHAPTER I

Introduction

1.1 Motivations

Fire, or more accurately combustion, has played a pivotal role in the development of the human race. For primitive human beings, the ability to control and utilize flames for warmth, cooking, and protection from predators was essential for survival. Of course, as humans evolved, so did their ability to harness the heat, and subsequently the energy, generated by combustion processes. Steam engines powered by the burning of wood, and eventually coal, were central to the latter part of the industrial revolution in the late 18th and early 19th centuries. Since that time, beginning with ships and trains, mass transportation vehicles have depended upon combustion. From the internal combustion (IC) engines that power our automobiles, to the gas turbine engines that propel aircraft across the sky, and even to the massive rocket engines that have sent astronauts into orbit and to the moon, the majority of engines that enable modern day transportation rely upon the combustion of either liquid, gaseous, or solid fuel.

Beyond transportation, however, modern life as we know it would not be possible without our current ability to control and utilize combustion processes. In fact, approximately 80% of the world's energy needs are currently met through some form of combustion [39]. And the relationship between energy and modern civilization, I

believe, was best put by Dave Mosher [40],

> The lifeblood of modern civilization is affordable, free-flowing energy. It gives us the power to heat our homes. Grow and refrigerate food. Purify water. Manufacture products. [And] perform organ transplants.

It also facilitates all forms of modern research and is likely enabling you to read this right now, especially if you are using a computer to do so. Moreover, as a civilization, our energy needs are only going to increase in the future. Even if the energy usage per person remains constant for the next thirty years, the total energy consumption in the world is still going to rise dramatically in that time. This is because the world's population is expected to increase by over 20% between now and 2050 (see Ref. [40] and the references therein). Furthermore, our reliance upon the combustion of fossil fuels is not likely to decline in that time [39].

There are, of course, issues with continuously burning fossil fuels to satisfy the energy needs of our world. For one, fossil fuels are a limited resource. Though coal, gas, and oil reserves are predicted to last at least another fifty years [39], the cost of a resource that will inevitably be entirely consumed will most certainly increase beyond the realm of what is considered "affordable." Additionally, instabilities in the geopolitical environment of our world can, without much warning, jeopardize access to our primary fuel reserves and cause the cost of these fuels to rise sharply. But even if the world's access to fossil fuels is unhindered for the next several centuries, it is without question that burning these fuels on such a grand scale has a negative impact on our environment. This is because fossil fuels are carbon-based, and thus burning them with air generates large amounts of CO_2 and other gaseous species that change the composition of our atmosphere. In fact, since the industrial revolution the concentration of CO_2 within our atmosphere has increased by over 50% [41]. This, as substantial scientific evidence indicates [41], is the primary cause of increasing global temperature, extreme weather patters, and rising sea levels. Yet, beyond

the environment, burning fossil fuels can have detrimental impacts on the health of humans and all forms of life. For example, un-burned hydrocarbons (UHC) and soot (or smoke), which are the result of incomplete combustion of carbon-based fuels and are exhausted by many modern day combustion engines, are known carcinogens [42]. Therefore, in order for our civilization to progress and thrive within a world that is dependent upon timely mass transportation and a continuous supply of energy, we must develop transportation and energy production systems that are affordable, efficient, and harm the environment – and life in general – as little as possible.

For this reason, energy from alternative sources, such as solar, wind, hydroelectric, and nuclear, have become increasingly popular. There are, however, several disadvantages to obtaining energy from solar and wind. For one, they cannot provide a continuous source of energy and it is difficult to efficiently throttle the energy from them to satisfy ever fluctuating demands. Furthermore, because those systems require large areas of land and, at present, are not particularly efficient, at this time they do not offer an affordable alternative to the burning of fossil fuels. Though hydroelectric dams also take up large portions of land, they are in fact the leading source of alternative electricity [39]. Yet, obviously such systems can only exist in specific parts of the world and they often negatively impact the ecosystems that surround them. Obtaining energy from nuclear power plants is ideal in theory, however, current geopolitical policies coupled with the general public's negative view of them has hindered, and will continue to hinder, the development of nuclear power sources [40]. Moreover, in comparison to modern gas turbine engines operating with liquid hydrocarbon fuels, the weight-to-energy production (or weight-to-thrust) ratio of these alternative sources is extremely high. Thus, even if a significant portion of our electricity and ground-based transportation needs are met via alternative sources, aircraft are unlikely to be powered by anything other than engines that burn hydrocarbon fuels. Needless to say, the combustion of fossil fuels is going to remain a primary source of energy

for the foreseeable future. Hence, it is paramount that our civilization develop means to utilize the combustion of hydrocarbons in ways that are economical, efficient, and clean.

Designing, developing, and testing combustion-based engines is both highly challenging and extremely expensive. In terms of time, labor, and expenses, it is not feasible to preform countless full-scale experiments in which one small parameter of a combustion system is varied until that system produces a minimal amount of pollutants while still operating as efficiently as possible. Therefore, it is tempting to turn to technology. That is, it would be ideal if one could simply run computer simulations to identify the cleanest and most efficient engine design. In principle, one can develop computer simulations that directly solve the fundamental equations that govern the dynamics of a reacting fluid and that also incorporate the expected chemical reactions and species associated with the combustion of hydrocarbon fuels. Such direct numerical simulation (DNS) algorithms have in fact been developed and have been successfully implemented (see, for example, Refs. [24–26, 31, 32, 43–45]). Nevertheless, performing DNS studies in an effort to optimize a combustion engine is no more practical than conducting innumerous experimental studies.

The reason DNS studies are not a practical means by which to optimize practical combustion engines is a consequence of the inherently turbulent nature of their reacting flow fields. In fact, without the enhanced mixing brought about by turbulence, modern combustion engines would not be as efficient nor as compact as they are. However, because turbulent flows possess a large range of spatiotemporal scales, to simulate them in their entirety (i.e. to resolve their largest and smallest possible scales) requires many grid points and time steps. The number of spatial grid points required is of course related to the ratio between the largest and smallest scales expected to exist within the flow. Since the integral length scale (L, which represents the scale that contains the majority of the turbulent kinetic energy (TKE) within a

flow), is one of the largest possible scales in a flow, and the Kolmogorov length scale (η, which signifies the scale at which viscus dissipation begins to convert TKE into heat), is one of the smallest possible scales in a flow, the ratio of these two values is related to the number of grid points needed in one direction. Based on the scaling principles of Kolmogorov's 1941 theory [46], one can show that L/η is directly related to the turbulent Reynolds number (Re_T); namely:

$$\frac{L}{\eta} = Re_T^{\frac{3}{4}}. \tag{1.1}$$

Where Re_T is defined as:

$$Re_T = \frac{u'L}{\nu}, \tag{1.2}$$

and where u' and ν represent the root mean square (RMS) of the velocity fluctuations and the kinematic viscosity, respectively. Because turbulence is an inherently three-dimensional (3-D) phenomenon, the total number of grid points required to fully resolve a turbulent flow is proportional to $Re_T^{9/4}$. Then, solving the governing differential equations (i.e. the Navier-Stokes equations [1, 47, 48]) at each grid point requires numerical integration. In order for such integration to resolve the highest expected frequencies, the time between each integration step must be proportional to η/u'. Then, if the size of the combustor is on the order of L, the total simulation time is $\sim L/u'$. Therefore, the total number of integration steps at each grid point is proportional to $L/\eta = Re_T^{\frac{3}{4}}$, and hence, the number of floating point operations required to solve a turbulent flow via a DNS scales with Re_T^3.

Gicquel et al. [33] suggest that within jet engines $Re_T \sim \mathcal{O}(10^8)$. Thus, a rough estimate of the number of floating point operations it would take to solve the turbulent

flow through a jet engine is $\mathcal{O}(10^{24})$ (i.e. a quadrillion computations)[1]. Now if NASA's largest supercomputer, which performs $\sim 6\times10^{15}$ floating point operations per second (FLOPS) [49], was used to solve this problem it would take $\sim$5.5 years and would cost $\sim$500 million dollars to do so (based on information provided in Ref. [50]; see Appendix A for details). One could argue that five and a half years is not a terribly long time and that half of a billion dollars is worth improving the efficiency of and reducing the harmful emissions from an engine. However, notice that the above analysis only considered the turbulent flow; incorporating the reactive processes that occur within a modern jet engine will only exacerbate the problem. Furthermore, the amount of data generated by such a simulation would likely be on the order of several hundred (if not several thousand) terabytes (TB), and hence, extracting meaningful information from such a large data-set would itself take years and cost large sums of money. Even more concerning is the fact that the aforementioned estimates were for performing just one simulation. Attempting to optimize an engine that has minimal harmful exhaust but runs as efficiently as possible would require hundreds if not thousands of such simulations (i.e. hundreds of years and trillions of dollars). Obviously, designing optimal combustion engines requires a more practical solution.

While DNS studies are clearly impractical tools for designing full-scale combustion engines, the current state-of-the-art in combustion engine design actually involves numerical simulations. However, in order to render the problem computational tractable, either the governing equations or the spatiotemporal domain of the problem are simplified. An example of the former are simulations in which the Reynolds-Averaged Navier-Stokes (RANS) equations [48, 51] are solved, while the latter is a characteristic of a large-eddy simulation (LES) [33, 52]. RANS equations govern the

[1]Note that this is merely just an estimate. The number of floating point operations required to solve a turbulent flow problem is *proportional*, not equal, to Re_T^3. For instance, the number of FLOPS necessary to solve a flow problem with $Re_T = 1$ is not one. Therefore, the values determined in this exercise should be considered as order of magnitude ($\mathcal{O}(\cdot)$) estimates, rather than exact values.

transport and production of average quantities (e.g. mean velocity, temperature, pressure, gas composition, etc.) within a fluid. Motivation for solving RANS equations, instead of the full Navier-Stokes equations, stems from the fact that in practice average quantities are the primary parameters that influence the design of combustion engines. In an LES, only the largest scales within a turbulent flow are resolved. That is, the grid spacing and time steps in an LES are generally much lager than η and η/u', respectively. The impetus for performing an LES is that the majority of the TKE within a turbulent fluid, and thus its mixing ability, is contained within its largest scales.

Though solving RANS equations or performing an LES can certainly reduce the time and cost of numerically simulating a turbulent flow problem, both of these approaches have drawbacks. For instance, RANS equations suffer from the closure problem, which is the fact that attempting to use additional transport equations to explicitly solve for the higher-order (i.e. un-closed) terms within them always leads to even more un-closed terms. Thus, solving RANS equations require that the higher-order/un-closed terms be modeled. When an LES is conducted, models are also necessary to simulate the physics occurring at the unresolved scales (e.g. the sub-grid stresses). The ability of such simulations to accurately solve turbulent flow problems, thus rests upon the validity of the models and the assumptions those models are based upon. However, because our fundamental understanding of turbulence is severely lacking, such models are typically derived from intuition and empiricism rather than physical principles [1].

The addition of combustion to a turbulent flow complicates the modeling process even further. Simulations that solve RANS equations require modeling not just for the higher-order terms associated with the turbulence, but also for the highly non-linear chemical source terms. These terms must also be modeled in an LES because, under practical conditions, chemical species mix, and hence thermochemical reactions

occur, at scales much smaller than those resolved by an LES [33, 52]. Again, these models and the regimes (i.e. turbulent conditions) over which their assumptions are valid, are generally based on intuition and dimensional reasoning [1, 53] rather than physics. This, in part, is a product of our minimal understanding of turbulence, but it is predominately a result of our insufficient knowledge of the fundamental interactions between turbulence and combustion processes and the mutual effects they have on each other. In other words, the development of accurate, robust, and reliable turbulent combustion models is a very challenging problem, which is indicative of the fact that it has been at the forefront of the field of combustion science for the past +50 years.

Turbulent premixed combustion, wherein the fuel and oxidizer are homogeneously mixed well upstream of the flame front, is a particularly challenging problem to model. This results from the fact that the most popular modeling schemes for turbulent combustion require knowledge of the location of the flame front and/or is topological configuration (i.e. curvature and surface wrinkling) [1, 33]. Yet, unlike their non-premixed counterparts (i.e. where the fuel and oxidizer are separate until the point of combustion), turbulent premixed flames can potentially propagate to and exist within any region of the incoming flow field. Indeed, while the location, topology, internal structure (e.g. thickness, connectivity, etc.), and dynamics of turbulent non-premixed flames are primarily governed by the mixing field, those of premixed flames are dictated by a highly non-linear coupling between the turbulent flow field and the finite rate chemical kinetics controlling the thermochemical reactions. Thus, accurately predicting such features of premixed flames is, in general, more challenging than doing so for non-premixed flames.

Nevertheless, burning in a premixed or partially-premixed mode (which is very similar to premixed combustion under even modestly turbulent conditions [54]), especially when the overall equivalence ratio is lean, is advantageous. The reason for

this stems from the fact that the product gasses from lean premixed flames are generally cooler than those from non-premixed flames with the same reactants (i.e. because non-premixed flames burn near the stoichiometric contour, their product gasses are always near the highest achievable temperatures for a particular set of reactants). Since the production of oxides of nitrogen (e.g. NO, NO_2, or in general NO_x) substantially increases with temperature, keeping the temperature of product gasses cool (e.g. below 1800 K) by burning in a lean premixed mode can reduce NO_x emissions from combustion engines [55]. This is crucial because NO_x are responsible for ozone depletion and contribute to smog and acid rain. Thus, they pose a serious threat to civilization, and accordingly, their emissions are highly regulated by federal agencies [56]. Therefore, combustion engines operating in a lean premixed mode are currently (e.g. the GENx gas turbine engine by General Electric [57]), and will continue to be pivotal to the production of clean energy from hydrocarbon fuels.

As the previous discussions have indicated, designing and developing such engines will undoubtedly rely upon accurate and reliable predictive models of turbulent premixed flames. Ensuring that these models are indeed accurate and reliable requires a deep fundamental understanding of the effects turbulence has on the structure and dynamics of turbulent premixed flames, particularly at the high turbulent Reynolds number conditions found in practical combustion devices. Since DNS studies do not offer a practical means by which to attain such understanding, high-fidelity experimental investigations of turbulent premixed flames with high Re_T values are necessary. This thesis presents the results of such experimentation. Furthermore, the results presented here, as well as those from previous studies of turbulent premixed flames, are used to assess the phenomenological hypotheses that, heretofore, were thought to bound regimes in which particular classes of premixed combustion models were believed to be superior to others. Based on this assessment, new hypotheses are proposed that are both more physically sound and more consistent with experimental

results than previous theories.

1.2 Outline

The aim of this dissertation is to elucidate the effects turbulence levels found in practical combustion devices have on the structure of premixed flames. Such understanding is subsequently used to assess the validity of theoretical regimes of combustion, which are used to help identify the most appropriate model for a particular problem.

The contents of this dissertation are organized as follows:

- **Chapter I: Motivations, Theory, and Objectives** The remainder of this Chapter is focused on providing background for and describing the objectives of the work presented in this dissertation. Prior to presenting details regarding theoretical regimes of turbulent premixed combustion, a brief review of laminar premixed flames is provided. This is because most theoretical definitions for the boundaries of such regimes rest on comparisons between the turbulent characteristics of a reacting flow and those associated with a laminar flame. After that discussion the theoretical regimes of turbulent premixed combustion and the theories used to develop them are introduced. Then a review of prior studies relevant to the work presented in this dissertation are discussed. Finally, this Chapter concludes by presenting the primary objectives of this dissertation.

- **Chapter II: Experimental Details** The purpose of this Chapter is to introduce details regarding the experimental studies that were performed in order to characterize the structure of the extremely turbulent premixed flames considered in this dissertation. First, the burner used to stabilized such flames is described and the properties of the 28 separate flames investigated here are listed. Then the diagnostic tools and optical configurations that were imple-

mented to characterize the flows and visualize the structures of the flames that were immersed within them are described. Because multiple diagnostics and optical setups were employed in this dissertation, a summary of each of them is provided in the last section of this Chapter.

- **Chapter III: Image Processing and Assessment of Techniques** Extracting meaningful information from the flame structure images that were obtained in this dissertation required the implementation of both standard and novel image processing techniques. The first portion of this Chapter is dedicated to describing those techniques. An assessment of their robustness is also provided. The second part of this Chapter provides details regarding uncertainties in the measurements that were made. Finally, the last two sections of this Chapter present assessments of the preheat and reaction layer visualization techniques that were implemented in this dissertation.

- **Chapter IV: Preheat and Reaction Layer Structure** Both qualitative and quantitative information regarding the preheat and reaction zone structures of the flames investigated here are presented in this Chapter. First, sample images of preheat and reaction layers are provided and the features they exhibit are described. Average preheat and reaction layer thicknesses derived from all 28 cases considered in this dissertation are then plotted as a function of u'/S_L. The trends observed in that plot are then discussed and contrasted against results from prior experimental studies. The last portion of this Chapter discusses the degree of localized extinction events in the flames considered and presents results that help elucidate the reasons for them.

- **Chapter V: Measured Regime Diagram** Two of the the key boundaries of the theoretical Borghi Diagram are found to be in contradiction with the qualitative and quantitative results presented in Chapter IV. Additionally, results

from 23 prior experimental and numerical studies indicate that these boundaries fail to accurately distinguish various regimes of turbulent premixed combustion. Thus, within this Chapter new hypotheses for defining the limits to regimes of premixed combustion are presented. The boundaries that result from those hypotheses are then compared to and subsequently found to agree far better with results from the current and prior investigations of turbulent premixed flames. Finally, this Chapter concludes with cautions regarding the interpretation of regime boundaries. Namely, that they should be considered as marking transition regions rather than strict demarcations.

- **Chapter V: Conclusions and Future Efforts** A summary of the results presented throughout this dissertation and the conclusions derived from them are provided in this final Chapter. While these results provide substantial insight into the structure of extremely turbulent premixed flames, there are still many unanswered questions surrounding the fundamental aspects of turbulent premixed combustion. Therefore, this dissertation concludes with a discussion of future efforts that are necessary to deepen our understanding of the dynamics and structural features of turbulent premixed flames.

1.3 Properties of laminar premixed flames

Some of the most popular turbulent premixed combustion models are based on the assumption that, at a local level, turbulent premixed flames retain the attributes of a laminar flame (e.g. flamelet models [58, 59]). Furthermore, the theories employed to determine the regime (or regimes) in which that assumption is valid are typically derived from comparisons between characteristics of the turbulence and those associated with a laminar flame. Therefore, prior to discussing theories that aim to distinguish various regimes of turbulent premixed combustion, it is helpful to first

introduce features of laminar premixed flames.

For turbulent premixed combustion theories, the key parameters of a laminar premixed flame are its characteristic length and velocity scales. The characteristic velocity scale of a laminar flame is the laminar burning velocity (S_L). S_L represents the speed a laminar flame front propagates normal to itself and is dictated by a reactive-diffusive balance [36] between: 1) the ability of the flame to heat the incoming reactants through diffusion; and 2) the rate at which its thermochemical reactions can convert the preheated reactants into products. The characteristic length scales of a laminar premixed flame are related to its thickness. There are three different thicknesses that can be defined for laminar flames, they include the laminar preheat zone ($\delta_{PH,L}$), reaction zone ($\delta_{RZ,L}$), and total flame thickness ($\delta_{F,L}$), where $\delta_{F,L}$ is classically defined as the sum of $\delta_{PH,L}$ and $\delta_{RZ,L}$ [47]. To help illustrate the definitions of and the relationships between these length scales, a sketch of a laminar flame is provided in Fig. 1.1a. Additionally, Fig. 1.1b displays profiles of temperature and various chemical species (obtained from a CHEMKIN simulation, the details of which are provided in Section 2.1) plotted as a function of the distance along the trajectory highlighted by the red line in Fig. 1.1a.

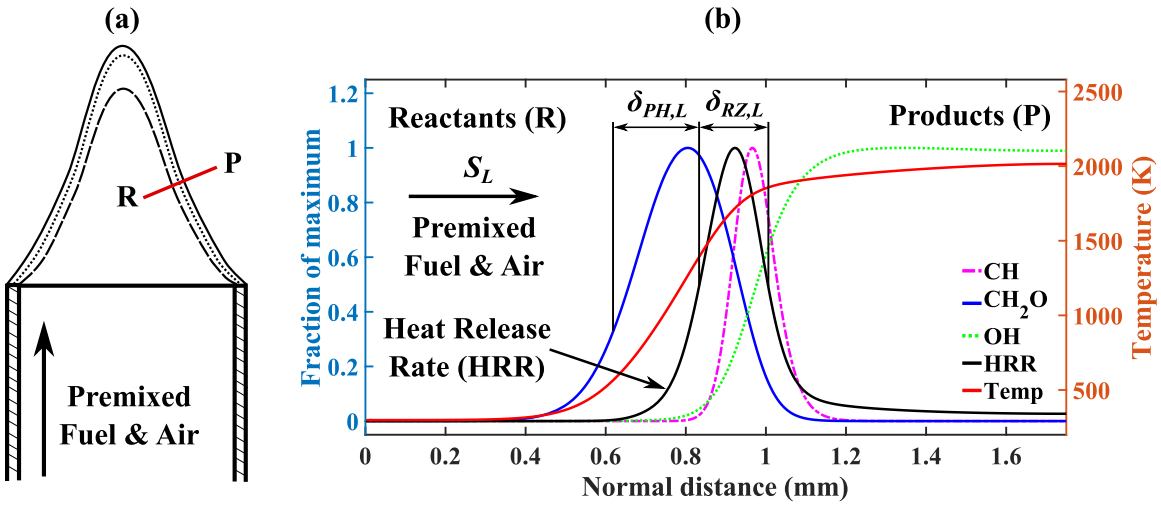

Figure 1.1: (a) Sketch of a laminar premixed flame. The dashed and dotted black lines indicate the upstream boundaries of the preheat and reaction layers, respectively. (b) Sample profiles of temperature and multiple chemical species derived from a freely propagating CHEMKIN simulation of methane and air at an equivalence ratio of 1.05. Note that these profiles represent those that would be obtained from the red line in (a).

As Fig. 1.1b indicates, the reaction zone (or layer) is marked by the region where the rate of heat release is highest. The reason for this is that reaction layers are classically defined as the region where the primary thermochemical reactions occur [47]. In order to initiate and sustain these chemical reactions, the local temperature of the premixed reactants must be elevated beyond a particular threshold (e.g. ∼1500 K for methane-air flames). In a laminar flame, this is achieved through the diffusion of warm species (e.g. CH_2O, HO_2, etc.) generated in or near the reaction layer to regions just upstream of that layer. As can be seen from Fig. 1.1b, this convective-diffusive balance between the cool incoming reactants and the warm species diffused from the reaction layer causes the temperature to monotonically increase as the reaction layer is approached from the reactants side. The region just upstream of the reaction layer, where the temperatures are elevated above those of the incoming reactants, is, as Fig. 1.1b shows, defined as the preheat zone (layer) [47].

There are, of course, many ways to define $\delta_{PH,L}$, $\delta_{RZ,L}$, and $\delta_{F,L}$. Our defini-

tions for determining $\delta_{PH,L}$ and $\delta_{RZ,L}$ from measurements are provided in Chapter III. However, as can be gathered from Fig. 1.1b, for laminar premixed methane-air flames at atmospheric conditions they are on the order of several hundred microns. Furthermore, the value of S_L for such flames varies between ~10 cm/s to ~40 cm/s depending on the equivalence ratio of the reactants (see Table 2.2). Again, and as will be shown in the next section, comparisons between these length and velocity scales to those associated with turbulence (e.g. L, η, and u') are central to theories of turbulent premixed combustion.

1.4 Theoretical Regimes of Turbulent Premixed Combustion

Identification of the most appropriate model to simulate a turbulent premixed combustion problem is often linked to the structural features expected to be exhibited by the flames within that problem [1]. For this reason, the ability to accurately predict the structure of turbulent premixed flames, based on a condensed set of governing parameters (e.g. turbulence level and integral scale), has been a primary goal of combustion science for the past four decades. The allure of attaining this ability is that it would allow one to easily determine the the most appropriate formulation for modeling the reaction processes within a given combustion system. For example, if the spatiotemporal scales of the primary combustion reactions in a particular system mimic those of a laminar flame, then it is likely that a flamelet model [58, 59] would most accurately simulate the combustion physics associated with that system. However, if a problem possesses locally extinguished and/or significantly broadened reactions, accurately simulating that problem necessitates the use of models equipped to handle such phenomena.

Alas, the structural features of premixed flames within practical combustion devices are not known a priori. Nonetheless, theoretical attempts (guided by some empirical evidence) have been made to classify turbulent premixed flames into var-

ious regimes of combustion [1, 53, 58–72]. The central theory used to delimit one regime from another rests on dimensional reasoning and scaling principles first introduced by Damköhler [60]. Namely, he theorized that if eddies smaller than a laminar flame exist within a reacting flow, they will penetrate the flame, and through enhanced diffusion, will distort its structure and disrupt its propagation rate [60]. Yet, if all of the eddies within a turbulent flow are larger than $\delta_{F,L}$, their effect is simply to wrinkle and stretch the flame front without distorting its thickness or time scales [60]. This latter hypothesis forms the basis for the *flamelet* concept [58, 59], which is one of the most common approaches to modeling the reactive processes of turbulent premixed flames.

The principal assumption of the flamelet concept is that, locally, the turbulent flame retains a laminar like structure. There are at least two ways in which the flamelet assumption is exploited to model turbulent premixed flames. One involves the development of state relations (or mapping functions) between a conserved scalar (e.g. progress variable) and reactive scalars (i.e. chemical species). The other further assumes that the flame front can be treated as an infinitely thin passive interface that separates products from reactants and, on a local level, propagates at the laminar flame speed [1, 73, 74] . In the former, the chemical source term within a transport equation for the conserved scalar can be closed by using the state relation to provide details of the local concentrations of the chemical species. In the latter, the average chemical source term within a similar transport equation is often closed by assuming that it can be related to a flamelet crossing frequency [1, 75], which can also be related to the flame surface density (Σ) [1, 74, 76–79]. Though these modeling methodologies differ substantially in their approach, the appropriateness of both of them is grounded in the validity of the flamelet concept. Thus, knowing the range over which the flamelet concept is valid is a practical concern.

Klimov [61] and Williams [66, 67] were the first to address this concern, and

they did so by refining Damköhler's ideas. Specifically, they proposed that when the Kolmogorov length scale (η) becomes smaller than $\delta_{F,L}$, the flame broadens and no longer resembles nor behaves like a laminar flame. Thus, the theoretical boundary between flamelet and non-flamelet regimes is often referred to as the Klimov–Williams criterion and was initially defined by $\eta = \delta_{F,L}$. In addition to this theoretical limit, several others were consolidated into phase diagrams by multiple authors in the early to mid 1980s [59, 63–65, 68, 69, 71]. Each of these diagrams, as well as those presented in Refs. [1, 36, 53, 70, 72, 80], were constructed slightly differently; however, the version most commonly referred to today was first introduced by Borghi [64, 65] and has since been refined by Peters [1, 36, 59]. A modified version of the *Borghi Diagram* presented by Peters in Ref. [1], is displayed in Fig. 1.2a.

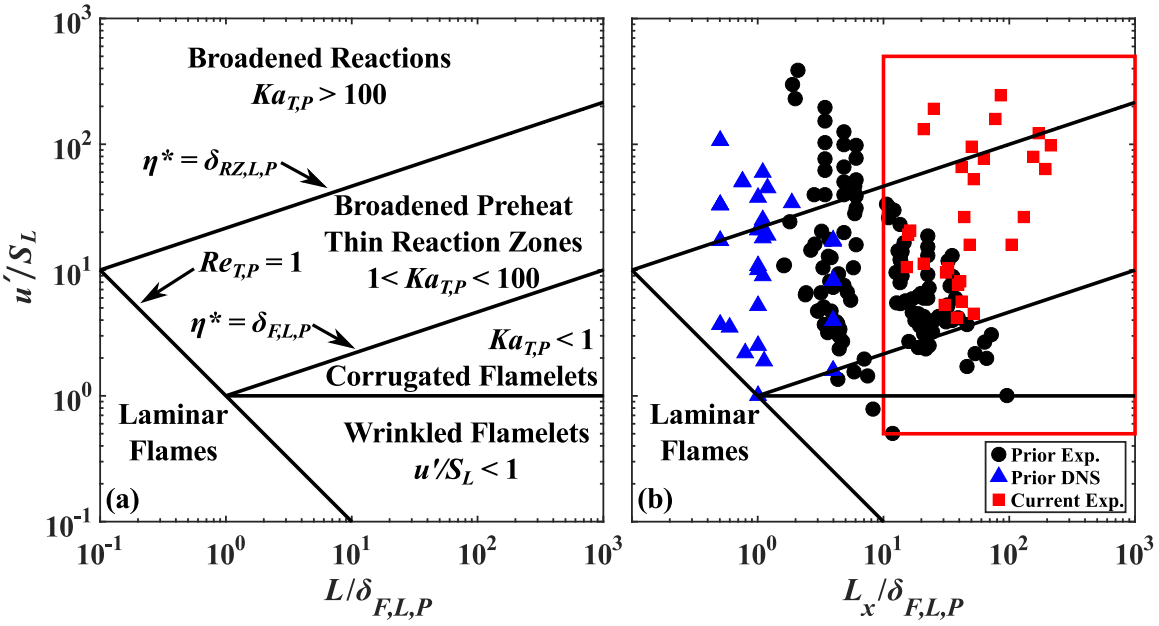

Figure 1.2: (a) Theoretical Borghi Diagram adopted from Ref. [1]. (b) The same diagram with prior and current cases included. Where black circles represent prior experimental cases (See Refs. [2–23]), blue triangles mark prior DNS studies (see Refs. [24–32]), and the red squares indicate the experimental cases presented in this investigation. Definitions for $\delta_{F,L,P}$, $Re_{T,P}$, and $Ka_{T,P}$, are provided in Eqs. 1.3, 1.4, and 1.6, respectively. The red rectangle in (b) is an estimate of where practical devices generally operate (see Ref. [33]).

As Fig. 1.2a shows, Peters, and thus Borghi, constructed this diagram with the ordinate and abscissa being represented by the the nondimensional turbulence intensity (u'/S_L) and the ratio $L/\delta_{F,L}$, respectively. Note that in this study, and in many prior studies, the longitudinal integral length scale (L_x) is used to place cases on the Borghi Diagram. This is why L_x is used in Fig. 1.2b, which marks the locations of prior cases as well as those considered here. Furthermore, in order to be consistent with Peters' version of the Borghi Diagram, we have chosen to adopt his definition for $\delta_{F,L}$, namely:

$$\delta_{F,L,P} = \frac{(\lambda_{th}/c_p)_R}{(\rho S_L)_0} = \frac{D^*}{S_L}, \tag{1.3}$$

where ρ is the density, λ_{th} and c_p are the thermal conductivity and specific heat capacity, respectively, D^* is a characteristic molecular diffusivity, and the subscripts "0" and "R" indicate whether the parameters were evaluated at a reactant or a reaction layer temperature, respectively. By assuming a reaction layer temperature of 1500 K and employing an empirically based formulation to compute λ_{th}/c_p [81], Peters determined that $D^* \approx 7.2 \times 10^{-5}$ m^2/s. Then by considering a stoichiometric methane–air flame with $S_L \approx 40$ cm/s, he estimated that $\delta_{F,L,P} \approx 0.18$ mm [36]. Peters considered this to be an approximate measure of $\delta_{PH,L}$, which explains the specific definition he provides in Eq. 1.3 since the structure of a laminar preheat layer is based on a convective-diffusive balance [36]. Peters' definition for the laminar reaction layer thickness is also based on D^*. Specifically, by taking the square root of D^* divided by a fuel depletion rate, he estimated that the laminar reaction layer thickness is roughly an order of magnitude smaller than $\delta_{F,L,P}$. Thus, Peters defined the laminar reaction layer thickness to be $\delta_{RZ,L,P} = 0.1\delta_{F,L,P}$.

While the exact formulation of the Borghi Diagram in Fig. 1.2a differs from those constructed in Refs. [36, 53, 59, 63, 68–72, 80], all of them are fundamentally the

same. That is, the limits of their various regimes are typically marked by three specific nondimensional parameters: the turbulent Reynolds (Re_T), Damköhler (Da_T), and Karlovitz numbers (Ka_T). Peters [1, 36] provided the following definitions for these parameters:

$$Re_{T,P} = \frac{u'L}{S_L \delta_{F,L,P}}, \tag{1.4}$$

$$Da_{T,P} = \frac{S_L L}{u' \delta_{F,L,P}}, \tag{1.5}$$

$$Ka_{T,P} = \frac{\tau_{F,L,P}}{\tau_{\eta^*}} = \left(\frac{\delta_{F,L,P}}{\eta^*}\right)^2 = \left(\frac{u'^3 \delta_{F,L,P}}{S_L^3 L}\right)^{\frac{1}{2}}, \tag{1.6}$$

where the subscript "P" signifies a variable based on Peters' definitions, $\tau_{F,L,P} = \delta_{F,L,P}/S_L$ is a characteristic flame time scale, and τ_{η^*} and η^* represent the Kolmogorov time and length scales based on a reaction layer temperature (e.g. 1500 K), respectively. Note, however, that in this study, and in most prior studies, the turbulent Reynolds number that is reported is based on the following definition:

$$Re_{T,0} = \frac{u' L_x}{\nu_0}. \tag{1.7}$$

where ν_0 represents the kinematic viscosity of the reactants. To arrive at the specific definitions in Eqs. 1.4 – 1.6, Peters invoked two specific assumptions. The first was that $\delta_{F,L}$ should be defined as in Eq. 1.3 and the second was that the relevant Kolmogorov scale should be based on a kinematic viscosity evaluated at a temperature associated with the reaction layer ν^*. Specifically, Peters assumed that $\nu^* = D^*$, and hence the Kolmogorov length scale he considered was defined as follows:

$$\eta^* = \left(\frac{\nu^{*3}}{\epsilon}\right)^{\frac{1}{4}} = LRe_{T,P}^{\frac{-3}{4}}, \tag{1.8}$$

where ϵ is the dissipation rate of TKE.

It is apparent from Fig. 1.2a that the primary boundaries of Peters' version of the Borghi Diagram are represented by constant values of $Re_{T,P}$ and $Ka_{T,P}$. However, since most practical combustion systems are expected to operate in regimes highlighted by the red rectangle in Fig.1.2b [33] (i.e. highly turbulent conditions), Peters restricted his discussions to regimes in which $Re_{T,P} > 1$ and $u'/S_L > 1$, and we choose to do the same. As can be seen from Fig. 1.2a, the theoretical boundaries separating these remaining regimes are marked by constant values of $Ka_{T,P}$. For example, because $Ka_{T,P} = 1$ implies that $\eta^* = \delta_{F,L,P}$, it represents the Klimov–Williams criterion. This criterion defines the upper limit of the Corrugated Flamelet regime in Fig. 1.2a, wherein flames are believed to resemble wrinkled laminar flamelets intermixed with pockets of products and reactants [1, 59, 61, 66, 67, 70]. This is because $Ka_{T,P}$ is less than unity here (i.e. $\eta^* > \delta_{F,L,P}$), which suggests that turbulent eddies are unable to enter and disrupt the underlying flame structure but can severely stretch and wrinkle the flame – even to the point were multiple sheets and pockets can form. A cartoon illustrating the *predicted* structural appearance of flames categorized within this regime and the others in Fig. 1.2a is provided in Fig. 1.3.

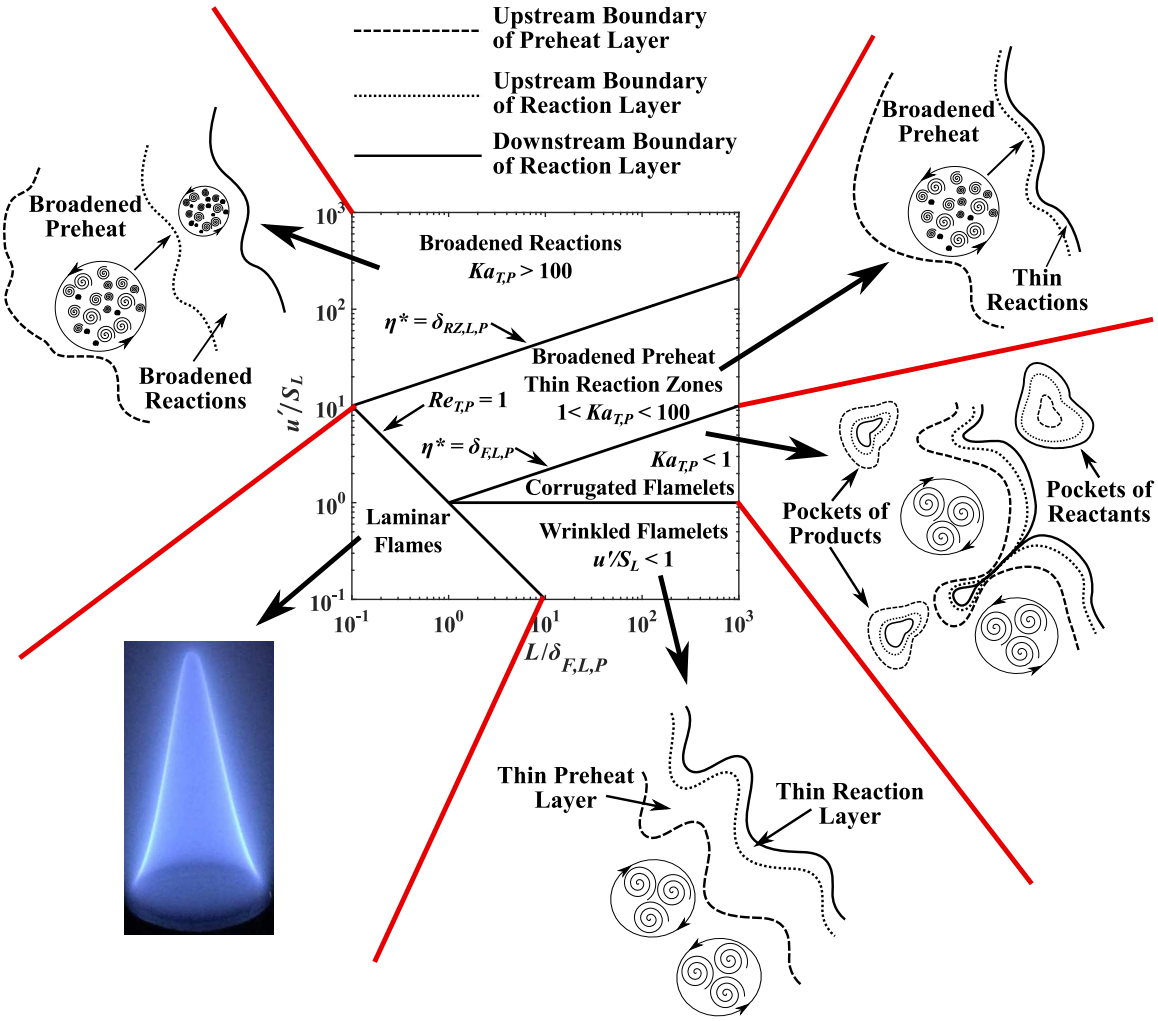

Figure 1.3: Cartoon illustrating the *predicted* structural appearance of flames categorized within each regime of the Borghi Diagram.

Above the Klimov-Williams limit, where $Ka_{T,P} > 1$ and $\eta^* < \delta_{F,L,P}$, Peters postulated that the smallest turbulent eddies will penetrate the flame and cause its preheat zone to broaden [1]. Yet, so long as η^* is larger than $\delta_{RZ,L,P}$, Peters argued that the reaction layers will remain thin [1]. If Peters' suggestion that $\delta_{RZ,L,P} = 0.1\delta_{F,L,P}$ is assumed to be true, then the inequalities $\delta_{RZ,L,P} < \eta^* < \delta_{F,L,P}$ and $1 < Ka_{T,P} < 100$ are analogous and define a regime in which flames are predicted to possess broadened preheat and thin reaction zones [1, 36]. The predicted flame structure for this regime is depicted by the sketch in the top right corner of Fig. 1.3. Peters termed this the *Thin Reaction Zones* regime; however, as is evident from Figs.

1.2a and 1.3, we choose to call it the *Broadened Preheat – Thin Reaction* (BP-TR) zones regime, since this more accurately descries the predicted flame structure here.

Peters further theorized that if $Ka_{T,P} > 100$ (i.e. $\eta^* < \delta_{RZ,L,P}$), then Kolmogorov eddies will enter the reaction zones and will cause them to become distributed [36, 59] or "broken" [1] (i.e. locally extinguished). The notion of a *distributed reaction zone* was first introduce by Summerfield et al. [82, 83] and can be described as a type of combustion wherein reactions and heat release are homogeneously spread throughout the flame brush and hence are not associated with steep temperature and concentration gradients [68, 84]. Initially, it was theorized that distributed reactions, or a "well-stirred reactor" combustion mode [36, 59, 70], would occur when $u' > S_L$ and $L < \delta_{F,L,P}$, or equivalently when $Da_{T,P} < 1$ [36, 59, 64, 70]. However, after a series of studies that linked flame extinction to high stretch rates [14, 15, 85–87], Peters argued that reaction layers will extinguish before they become distributed. Specifically, he posited that significant quenching will occur beyond $Ka_{T,P}$ =100 [1]. This, he postulated, is a result of the fact that for $Ka_{T,P} > 100$ eddies penetrate the reaction layer, enhance heat transfer to the preheat layer, and subsequently cause reactions to cease [1]. Therefore, Peters relabeled the Distributed Reactions regime as the Broken Reaction Zones regime and marked its boundary by $Ka_{T,P} = 100$ rather than $Da_{T,P} = 1$.

Notice however, that neither of these labels have been ascribed to this theoretical regime in Fig. 1.2a; instead, we will refer to it as the *Broadened Reactions* regime. An illustration of the flame structure associated with this theoretical regime is provided in top left corner of Fig. 1.3. The reason for not retaining Peters' Broken Reactions regime is because recent evidence from numerical and experimental studies suggests that local extinction is not solely the result of turbulence-flame interactions. For example, in a direct numerical simulation (DNS) study by Aspden et al. [26], it was argued that the reaction layers of flames with $Ka_{T,P} \gg 100$ remained continuous

because they were confined by hot products. Similarly, a detailed experimental and numerical study by Li et al. [21] linked flame quenching to the entrainment of cool, room air, which is corroborated by the results presented in Section 4.4. Since the Borghi Diagram is not designed to handle such phenomenon, the Broken Reactions regime cannot be accurately represented on it in its current state. The reason the Broken Reaction Zones regime was not replaced by a Distributed Reactions regime is that the term "distributed reactions" has most recently been claimed to characterize the structure of reaction zones in "mild" combustion experiments [88, 89]. Since these experiments primarily rely on highly preheated reactants, rather than turbulence, to generate distributed reactions, their structure is also unlikely to be captured by the classic Borghi Diagram. Thus, to distinguish distributed reactions produced under "mild" conditions from those generated primarily by turbulence-flame interactions, we have chosen to label the latter as *broadened reactions*. Yet, since the region of $Ka_{T,P} > 100$ is relatively unexplored [90, 91], it is not clear what type of flame structure should be ascribed to this portion of the Borghi Diagram, though suggestions are provided in this work.

While the Borghi Diagram is a useful tool for attempting to predict the structural features of premixed flames, its key boundaries (i.e. those defined by $Ka_{T,P} = 1$ and $Ka_{T,P} = 100$) are solely based on intuition and the phenomenological *hypothesis* that once Kolmogorov eddies penetrate preheat or reaction layers, they severely disrupt them. Thus, if the Borghi Diagram is to serve as a robust tool for accurately predicting flame structures, and hence when a particular model is superior to others, its boundaries must be assessed experimentally and perhaps be re-defined altogether. Additionally, to the best of the author's knowledge, evidence directly supporting the hypothesis that Kolmogorov eddies cause preheat and reaction zone broadening does not exist, and so an assessment can only be conducted with macroscopic results (e.g. measured preheat and reaction layer thicknesses). However, heretofore, a comprehen-

sive assessment of this sort has not been performed.

1.5 Prior Relevant Studies of Turbulent Premixed Flames

Numerous experimental [2–14, 17–23, 92, 93] and DNS [24–32, 45, 94] studies have shed light on the validity of various regime boundaries. For reference, cases from most of these investigations are included on the Borghi Diagram shown in Fig. 1.2b. While a handful of these studies present results that are consistent with the theoretical regimes in Fig. 1.2a [14–20, 92], the vast majority of them do not [2, 4–12, 14, 22, 25–30, 94]. Experimental investigations of methane–air jet flames by Zhou et al. [17–19] provide an example of the former, where broadened CH- and HCO-layers (which generally track the primary heat release zone) were observed only for cases in which $Ka_{T,P} > 100$ and remained relatively thin otherwise. In contrast, Tamadonfar and Gülder [2] applied Rayleigh scattering imaging to methane–air flames classified within the predicted BP-TR regime and found that their preheat zone thicknesses were thinner than their laminar counterparts. Additionally, using similar diagnostics, others [3–10] also observed relatively thin preheat layers for flames classified into the predicted BP-TR regime.

Another set of experimental studies with results that contradicted the predictions made by the Borghi Diagram are those by Dunn et al. [11–13]. Namely, even though their least turbulent condition was classified into the theoretical Broadened Reactions regime, its average reaction layer thickness (interpreted from the average of its temperature gradients (∇T) conditioned on a temperature of 1200 K; see Fig. 4 in Ref. [12]) was thinner than that in a laminar flame with the same equivalence ratio [12]. Furthermore, though they reported the occurrence of broadened reactions, this was only for cases in which $Ka_{T,P} > 2500$ [11, 12]; their other case, which had a $Ka_{T,P}$ of ∼2300, possessed un-broadened reaction layers. More recently, in a study of extremely turbulent (i.e. $u'/S_L > 25$) methane–air Bunsen flames, which comprised of

a subset of the data exhibited here, relatively thin and continuous reaction layers (inferred from the product of simultaneous images of formaldehyde and hydroxyl) were also observed in cases classified into the Broadened Reactions regime [22]. On the other hand, a series of 3-D DNS studies conducted by Aspden et al. [26, 27] were interpreted as indicating the existence of broadened reactions in hydrogen–, methane–, and propane–air flames positioned well above the $Ka_{T,P} = 100$ line. However, only four of their nine cases categorized into the Broadened Reactions regime displayed this flame structure; the other five – including one of their most turbulent case (i.e. $u'/S_L = 107$ and $Ka_{T,P} = 1562$) – possessed relatively thin and continuous reaction layers. A different set of 3-D DNS studies performed by Lapointe et al. [32] also observed broadened reaction layers. However, this was only in cases with $Ka_{T,P} \geq 270$, the reaction layers of their other two cases with $Ka_{T,P} > 100$ were relatively thin [32].

Though this is a rather brief account of prior experimental and numerical studies of turbulent premixed flames, it already suggests that the boundaries of the Borghi Diagram require alterations if they are to accurately distinguish various regimes of combustion. However, one deficiency of all of these previous studies (with the exception of [22]) is that they were conducted with $Re_{T,0} < 6,000$. Practical combustion devices, on the other hand, operate with much larger turbulent Reynolds numbers [33]. Furthermore, Fig 1.2b clearly indicates that the majority of prior investigations of turbulent flame structure fall outside of the regime where most practical devices are believed to operate [33]. Hence, in order to provide a more comprehensive assessment of the Borghi Diagram, and to elucidate the effects practical levels of turbulence have on the structure of premixed flames, there is a need to extend flame structure measurements to regimes of intense and extreme turbulence. This work addresses that need.

1.6 Objectives

This Chapter is designed to provided motivations and background for the objectives of this dissertation. The compelling arguments in Section 1.1 imply that the energy and transportation needs of our world will be satisfied through the combustion of fossil fuels for many years to come. Yet, because fossil fuels are a limited resource and burning them has detrimental impacts on life and our environment, there is a critical need to develop systems that can harness the energy from the combustion of fossil fuels in ways that are as efficient, economical, and clean as possible. From a practical standpoint, this requires accurate and reliable predictive models of turbulent premixed combustion. Section 1.4 presents and describes the current theories which attempt to identify the conditions over which such models remain valid. Of course, verification of these theories requires experimentation. As Section 1.5 points out, many experiments have provided insights into the validity of such theories. However, the vast majority of them were not conducted with levels of turbulence typically found in practical devices, and therein lies the impetus for the objectives of this dissertation.

The primary objective of this dissertation was to understand how increasing levels of turbulence affect the structure of premixed flames. To that end, high-fidelity flame structure measurements were made in premixed methane–air Bunsen flames subjected to intense and extreme levels of turbulence (i.e. $4.2 < u'/S_L < 25$ and $25 < u'/S_L < 246$, respectively). Those measurements were facilitated by three separate laser-based diagnostic techniques that permitted flame structure imaging. Namely, two of the diagnostics provided images of the preheat and reaction layers of the flames considered here while the other supplied images that helped elucidate the phenomena responsible for local extinction events (note that such events were rare in this study). By developing and implementing a novel local thresholding algorithm, statistics, such as average preheat and reaction layer thicknesses, were obtained from those images. Therefore, conclusions regarding the affects of increasing levels of

turbulence on the structure of premixed flames are drawn from both qualitative and quantitative results.

The secondary objective of this dissertation was to assess the validity of the primary boundaries on the theoretical Borghi Diagram (i.e those defined by $Ka_{T,P} = 1$ and $Ka_{T,P} = 100$). This was achieved by considering the results from the flame structure measurements made here as well as those from 23 prior experimental and numerical investigations of turbulent premixed flames. Nonetheless, attempts to reconcile those boundaries with measured results proved to be futile. Physical explanations for these inconsistencies are presented, and new *measured* and plausible regime boundaries are defined in light of these explanations. Beyond stemming from physical arguments, these new boundaries are far more consistent with experimental results than those in Fig. 1.2a. However, it is important to recognize that whether or not such boundaries are measured, plausible, or merely theoretical, they should not be interpreted as strict demarcations. Instead, we believe that the boundaries on any regime diagram should be viewed from a probabilistic standpoint (see Section 5.4 for further elaborations), and hence, should be considered as transition regions and not firm borders.

CHAPTER II

Experimental Details

There are (at least) three requirements for experimentally investigating the effects turbulent flow fields have on the structure of premixed flames. The first is the ability to generate and properly stabilize highly turbulent premixed flames. The second is the capacity to measure, and subsequently characterize, the properties of the flow fields in which the premixed flames exist. The third is the capability to non-intrusively probe the flame so that its structural qualities can be ascertained. This Chapter presents the details of how these three requirements were met in this investigation.

2.1 Burner and Experimental Conditions

All of the flames studied in this work were produced by the Hi-Pilot burner. A schematic of this burner as well as an image of it in operation are shown in Figs. 2.1a and 2.1b, respectively.

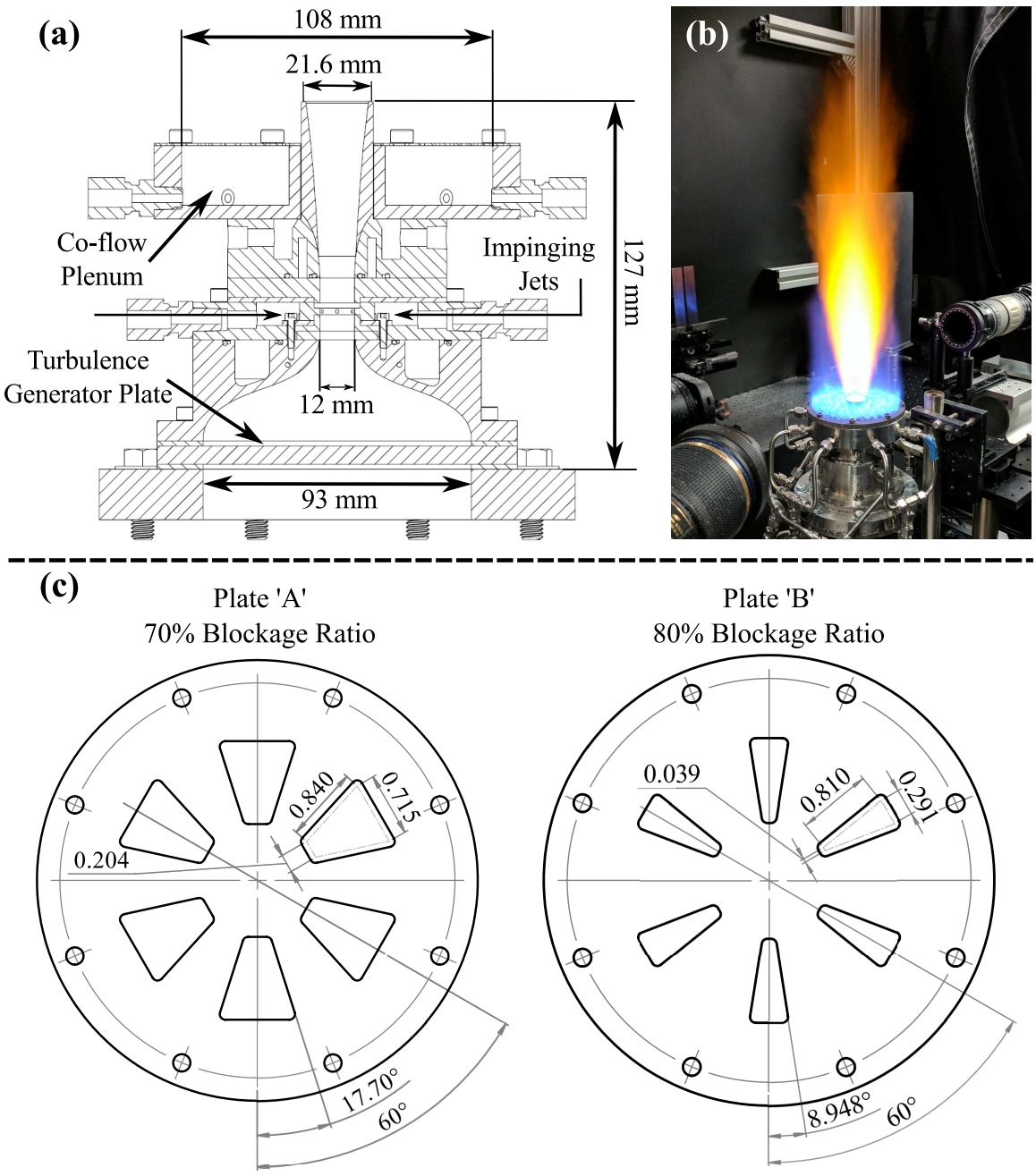

Figure 2.1: (a) Schematic of the Michigan Hi-Pilot Burner. (b) An image of the Hi-Pilot Burner while it is being operated. (c) Drawings of the two separate turbulence generator plates used in this study. Note that the dimensions incorporated on the turbulence plates are in inches.

The Hi-Pilot burner is a piloted, Bunsen-type burner that employs a slotted contraction device [95] and a jet-in-crossflow configuration to generate extremely turbulent flow fields. Specifically, the reactants in this study, which comprised of three different

equivalence ratios (ϕ= 0.65, 0.85, and 1.05) of methane and air, were premixed ahead of one of the two separate slotted plates in Fig. 2.1c. These plates produce flow fields with different turbulence properties, and in general, the slotted plate labeled 'A' in Fig. 2.1 generated larger values of u' and L_x at the exit of the burner than the 'B' plate. Downstream of the slotted plate is a converging-diverging nozzle, at the throat of which is a series of impinging jets that injected premixed reactants (at the same equivalence ratio as the primary flow) perpendicularly into the main flow. The total flow rate though these jets was set to 6% of the bulk flow rate in each case; however, the two lowest flow rate cases (cases 1 and 2) did not utilize these jets (to reduce turbulence levels). Downstream of the jets is the diverging portion of the nozzle, which has an exit inner diameter of 21.6 mm. The reactants issuing from this nozzle are ignited by a large-diameter (108 mm), methane–air ($\phi = 0.98$) pilot-flame. The purpose of such a large-diameter pilot was to shroud the main flame in a field of hot products, which helped to mitigate the entrainment of room-air to the reaction layers. A total of 28 separate cases stabilized by this burner were investigated here, and their details are provided in Table 2.1. Note that each case is referred to as Case$\alpha\beta$-ϕ, where α corresponds to the case number (i.e. 1 to 6, 6 having the highest flow rate), β will indicated which turbulence plate was used (e.g. β = A implies plate 'A' was used), and ϕ represents the equivalence ratio of that case.

Case	$\frac{u'}{S_L}$ [a]	$\frac{L_x}{\delta_{F,L,P}}$ [b]	U_0 [c] (m/s)	u' [d] (m/s)	L_x [e] (mm)	$Ka_{T,P}$ [f]	$Ka_{T,0}$ [g]	$Re_{T,0}$ [h]	$Da_{T,P}$ [i]
1A-0.65	11	21				8.3	30		1.9
1A-0.85	5.6	42	7.7	1.7	10	2.1	19	1,100	7.4
1A-1.05	4.5	52				1.3	6.5		12
2A-0.65	19	16				21	76		0.8
2A-0.85	9.6	31	14	2.9	7.5	5.3	48	1,400	3.3
2A-1.05	7.7	39				3.4	17		5.1
3A-1.05	16	105	32	6.0	20	6.2	30	7,900	6.6
4A-1.05	27	131	44	10	25	12	58	17,000	4.9
5A-0.65	159	77				228	817		0.5
5A-0.85	66	155	64	24	37	57	513	58,000	1.9
5A-1.05	64	194				37	178		3.0
6A-0.65	246	86				415	1487		0.3
6A-0.85	123	172	78	37	41	104	933	99,000	1.4
6A-1.05	98	215				66	324		2.2
1B-0.65	11	15				8.8	32		1.4
1B-0.85	5.3	31	6.0	1.6	7.3	2.2	20	760	5.8
1B-1.05	4.2	38				1.4	6.9		9.0
2B-0.65	21	16				23	83		0.8
2B-0.85	10	32.7	9.2	3.1	7.8	5.8	52	1,600	3.2
2B-1.05	9.6	31.4				3.7	18		5.0
3B-1.05	16	48	21	7.1	9.2	12	57	4,200	2.6
4B-1.05	27	44	28	9.3	8.4	18	90	5,100	1.8
5B-0.65	133	21				334	1196		0.2
5B-0.85	66	42	45	20	10	83	751	13,000	0.6
5B-1.05	53	52				53	260		1.0
6B-0.65	192	25				533	1907		0.1
6B-0.85	96	50	72	29	12	132	1197	22,000	0.5
6B-1.05	77	63				85	415		0.8

Table 2.1: Details of the 28 cases investigated here. [a] u'/S_L is the nondimensional turbulence intensity. [b] $L_x/\delta_{F,L,P}$ is the ratio of the longitudinal integral length scale to the laminar flame thickness, which is defined in Eq. 1.3. [c] U_0 is the centerline velocity. [d] u' is the r.m.s. of the velocity fluctuations. [e] L_x is the longitudinal integral length scale. [f] $Ka_{T,P}$ is the Karlovitz number defined by Peters (see Eq. 1.6). [g] $Ka_{T,0}$ is the Karlovitz number based on parameters determined in the reactants (see Eq. 5.7). [h] $Re_{T,0}$ is the turbulent Reynolds number based on L_x and ν_0, which is the kinematic viscosity of the reactants. [i] $Da_{T,P}$ is the turbulent Damköhler number defined by Peters [1] (see Eq. 1.5).

The mean centerline velocities (U_0) and other flow characteristics listed in Table

2.1 (i.e. u' and L_x) were obtained from single component Laser Doppler Velocimetry (LDV) measurements made on centerline, 5 mm downstream of the nozzle exit, and in non-reacting flows only (see Section 2.2, for details). In order to compute nondimensional parameters from these measured values the laminar flame speeds and thicknesses (S_L and $\delta_{F,L,P}$, respectively) needed to be determined for each of the three equivalence ratios. The separate S_L values, which are listed in Table 2.2, were computed from 1-D freely propagating CHEMKIN simulations that employed the GRImech 3.0 chemical kinetic mechanism [34]. All three values of $\delta_{F,L,P}$ were computed via Eq. 1.3, and are listed in Table 2.2 as well. Table 2.2 also lists laminar preheat ($\delta_{PH,L}$) and reaction zone thicknesses (which were interpreted from the laminar overlap and CH layer thicknesses: $\delta_{OL,L}$ and $\delta_{CH,L}$, respectively) measured in actual laminar flames (see Sections 2.2.2 and 3.1 for measurement details). Note that these measured laminar values are used in Section 4.3 to normalize those obtained from the turbulent flames.

	Computed			Measured (mm)		
ϕ	S_L [a] (cm/s)	$\delta_{F,L,P}$ [b] (mm)	$\delta_{th,L}$ [c] (mm)	$\delta_{PH,L}$ [d]	$\delta_{OL,L}$ [e]	$\delta_{CH,L}$ [f]
0.65	15.1	0.48	0.79	0.66	0.54	-
0.85	30.2	0.24	0.50	0.38	0.50	0.38
1.05	37.7	0.19	0.43	0.32	0.45	0.36

Table 2.2: Laminar flame speeds and thicknesses used for normalizations. [a] S_L was computed from CHEMKIN simulations that used GRImech 3.0 [34]. [b] $\delta_{F,L,P}$ is the laminar flame thickness defined by Peters [1, 36] (see Eq. 1.3). [c] $\delta_{th,L} = (T_p - T_0)/\frac{dT}{dx}|_{max}$ is the computed laminar thermal thickness, where T_0 and T_p are the temperatures of the reactants and products, respectively. [d] $\delta_{PH,L}$ is the measured laminar preheat zone thickness. [e] $\delta_{OL,L}$ is the measured laminar reaction (overlap) layer thickness. [f] $\delta_{CH,L}$ is the measured laminar reaction (CH) layer thickness. Note: the measured values were acquired from laminar Bunsen flames and their specific definitions as well as the algorithm used to determine them is described in Sections 2.2.2 and 3.1.

2.2 Diagnostics

This Section presents details of the diagnostic tools that were utilized to characterize the flow fields and to visualize the structure of the flames studied here.

2.2.1 Flow Field Characterization

As mentioned in Section 2.1, the flow field properties for each case in Table 2.1 were obtained from single component LDV measurements. In order make these measurements, the flows were seeded with 0.5 μm alumina-oxide particles, which were illuminated by an Argon-Ion laser (Coherent Innova 90c) operated at 514 nm and 1.5 Watts. All of the cases possessed Stokes numbers that were less than one, where the characteristic flow time was set to 5 times the smallest inertial range time scale (i.e. $\sim 10\tau_{\eta_0}$ [96]); hence, the particles tracked all of the flows reasonably well. Light scattered from the particles was collected through a standard optic and photomultiplier tube (TSI), and the resulting signal was processed via a Doppler burst correlator (TSI FSA 4000). Flow statistics for each case were based on two independent sets, with each set being comprised of 500,000 samples. Mean and RMS values varied by no more than 1% and 2%, respectively, between these separate sets, which demonstrates the repeatability of this diagnostic.

In addition to U_0 and u', longitudinal integral length scales were also derived from the LDV measurements. To facilitate this, the normalized slotting method of Mayo et al. [97] (see Refs. [95, 98] for additional details) was used to calculate temporal autocorrelation functions from the randomly sampled LDV data. Integrating these functions yielded longitudinal integral time scales ($\tau_{I,x}$), which were converted to length scales via a corrected version of Taylor's frozen flow hypothesis [99–104]. Specifically, the following relation was used to convert $\tau_{I,x}$ to L_x:

$$L_x = \tau_{I,x} U_0 \sqrt{1 + 5\left(\frac{u'}{U_0}\right)^2}, \tag{2.1}$$

and the reason for using this corrected version is because Taylor's hypothesis is not necessarily valid under the highly turbulent conditions studied here (e.g. u'/U_0 is greater than 30% for most of the cases in Table 2.1). Note that applying this correction yielded values of L_x that were at most 37% larger than what they would have been without it. Additionally, it should be mentioned that while we believe this correction to be proper, its application had little to no impact on the final conclusions presented in this paper. The variation between L_x values computed from the two independent LDV measurements made for each case was ∼20%, which is a reasonable error estimate for this measurement. To further assess this technique for determining L_x, LDV measurements were made in a non-reacting turbulent flow issuing from a simple pipe. The value of L_x computed from these measurements was ∼27% of the diameter of the pipe, which agrees well with values reported in literature (see, for example, Ref. [51]).

2.2.2 Flame structure visualization

In order to visualize and measure the structural features of the preheat and reaction layers within the cases listed in Table 2.1, three separate laser based diagnostics were implemented. The first of these techniques is "overlap-layer" (OL) imaging, which involves taking the pixel-by-pixel product of simultaneously acquired planar laser-induced fluorescence (planar LIF or PLIF) images of hydroxyl (OH) and formaldehyde (CH_2O) to generate "overlap-layers." Two variations of this technique were employed in this study. The first, which was preformed at the Propulsion and Combustion Engineering (PACE) Laboratory at the University of Michigan, was conducted with a small field of view (FOV) to provide high-resolution overlap-layer

images. The second was performed at the Air Force Research Laboratory (AFRL) at Wright Patterson Air Force Base, which was implemented with a medium-sized FOV to visualize the preheat layers of the flames considered here. Hereinafter, this latter overlap-layer imaging technique will only be referred to in terms of preheat layer imaging (e.g. the preheat layer imaging technique, etc.), since only preheat layer information was derived from it. Rayleigh scattering images were acquired simultaneously with these preheat layer images and preliminary results from that simultaneous imaging are used in Section 3.5 to justify our methods for visualizing preheat layers.

The other two flame visualization techniques employed in this study were also performed at AFRL. Unlike the overlap-layer and preheat layer images, which where obtained at a rate of 1.6 Hz and 10 Hz, respectively, these other two diagnostics permitted flame structure imaging at a rate of 10 kHz (i.e. at high-speed). The first of these high-speed imaging techniques was CH-PLIF imaging; the second involved the acquisition of images containing both CH- and OH-LIF signals. The ability to conduct this high-speed PLIF imaging was facilitated by a novel excitation/detection scheme for acquiring CH-PLIF images [105, 106], which is described in detail below. All three of these flame structure imaging techniques were applied to at least two separate regions downstream of the exit of the burner. The relative positioning of these regions of interest (i.e. FOVs) with respect to the burner are depicted in Fig. 2.2.

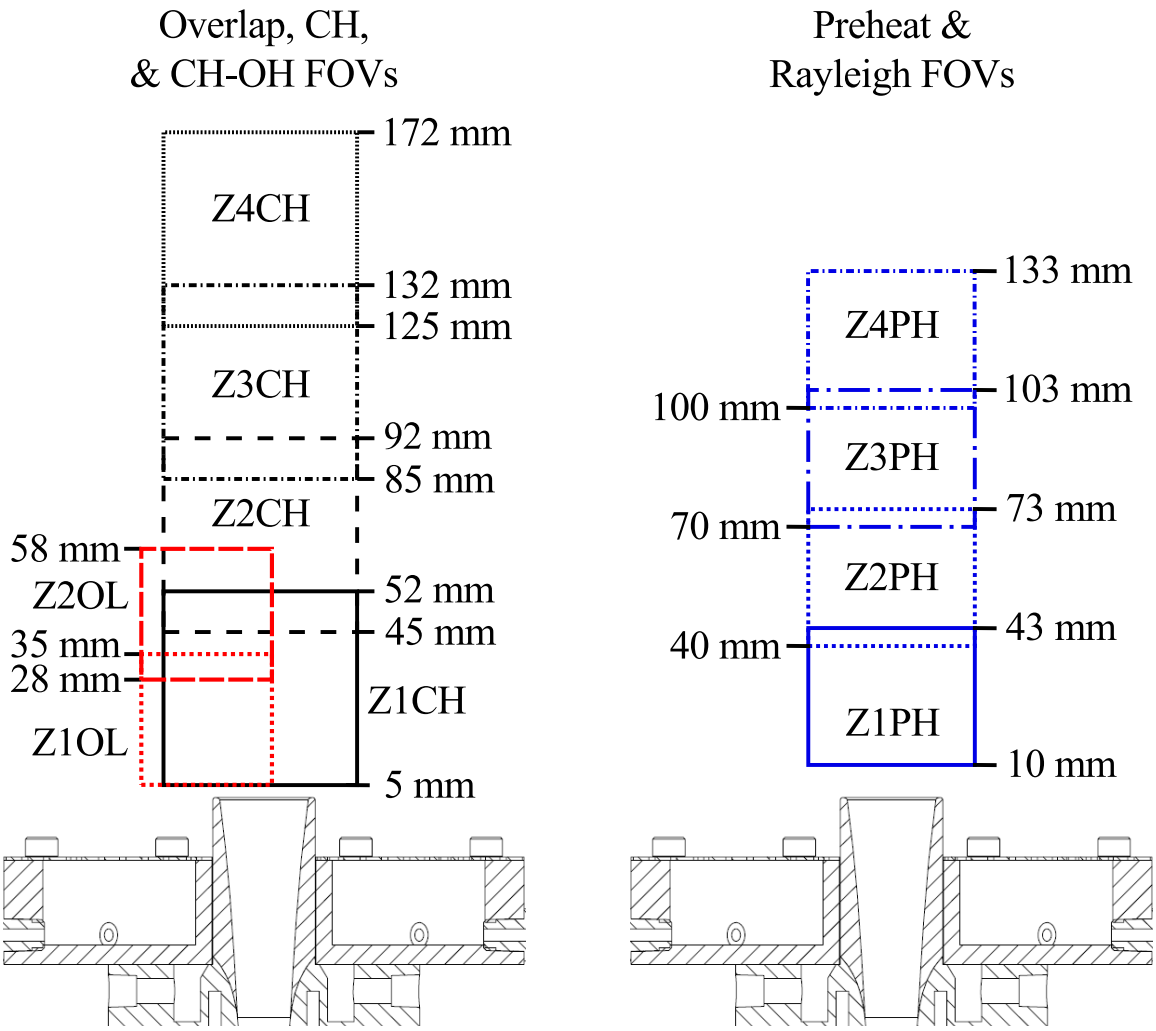

Figure 2.2: Diagram depicting the relative locations of the separate FOVs.

Finally, details regarding which information was acquired for each case considered and where (i.e. which FOV) that information was obtained from is provided in Table 2.3.

Case	Measurement details		
	Preheat	Overlap	CH
1A-0.65	Z1PH	Z2OL	none
1A-0.85		Z1OL	Z1CH
1A-1.05			
2A-0.65	Z1PH	Z2OL	None
2A-0.85		Z1OL	Z1CH – Z2CH
2A-1.05		Z2OL	
3A-1.05	None	Z2OL	Z1CH – Z3CH
4A-1.05	None	Z2OL	Z1CH – Z3CH
5A-0.65	Z1PH - Z3PH	Z2OL	None
5A-0.85			Z1CH – Z4CH
5A-1.05			
6A-0.65	None	Z2OL	None
6A-0.85	Z1PH – Z4PH		Z1CH – Z4CH
6A-1.05	None		None
1B-0.65	Z1PH	Z2OL	None
1B-0.85		Z1OL	Z1CH
1B-1.05			
2B-0.65	Z1PH	Z2OL	None
2B-0.85		Z1OL	Z1CH – Z2CH
2B-1.05			
3B-1.05	None	None	Z1CH – Z3CH
4B-1.05	None	None	Z1CH – Z3CH
5B-0.65	Z1PH	Z2OL	None
5B-0.85	Z1PH – Z3PH		Z1CH – Z4CH
5B-1.05			
6B-0.65	Z1PH – Z4PH	Z2OL	None
6B-0.85			Z1CH – Z4CH
6B-1.05	None		None

Table 2.3: Details regarding what information was acquired for the 28 cases considered here and where it was collected from, if it was at all. PH, OL, and CH indicate preheat, overlap and CH data respectively. ZnPH, ZnOL, and ZnCH indicate that the data was collected from Zone n (n = 1, 2, 3, or 4) of the preheat, overlap, and CH interrogation regions (see Fig. 2.2), respectively.

2.2.2.1 Overlap layer imaging

The overlap-method is a common technique for visualizing the reaction layers of flames (see, for example, Refs. [13, 19, 22, 23, 107–117]). As is demonstrated in

Fig. 2.3, the reason for this is because the spatial region over which CH_2O and OH overlap (i.e. the product of the concentrations of CH_2O and OH) correlates well with the region of peak heat release rate (HRR) in premixed methane–air flames.

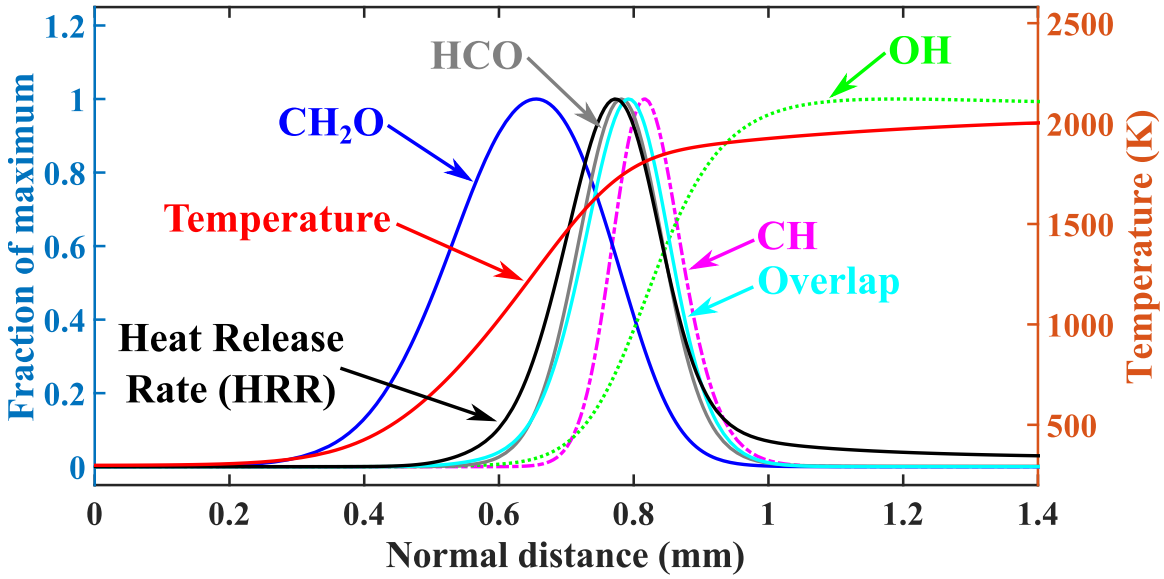

Figure 2.3: Profiles of key intermediate species to methane–air combustion. Profiles were derived from a 1-D freely propagating CHEMKIN simulation of a premixed methane–air flame with $\phi = 1.05$. The chemical kinetic mechanism utilized in this simulation was GRImech 3.0 [34].

This good correlation is explained by the fact that the reaction $CH_2O + OH \rightarrow HCO + H_2O$ is one of the primary ways in which fomyl (HCO) – which is a key species in the oxidation of hydrocarbons [118, 119] – is produced in hydrocarbon flames [107, 114, 119–121]. Furthermore, as Fig. 2.3 shows, the concentration of HCO correlates well with HRR. This, in part, is attributed to the fact that HCO is depleted far quicker than it is produced, and hence, its concentration and production rate are proportional to each other [107, 114, 119, 120]. For this reason, and because the aforementioned elementary reaction is one of the primary reactions responsible for the formation of HCO in methane–air flames [114, 119–121], the product of the

concentrations of CH_2O and OH correlates well with both HCO and HRR.

The previous discussion would suggest that a rather simple way to visualize the reaction layers of flames would be to perform PLIF imaging of HCO. While such imaging has been preformed (see Refs. [17–19, 119, 122]), conventional PLIF techniques (i.e. employing pulsed Nd:YAG lasers) do not provide adequate signal levels because: 1) HCO is found in relatively low concentrations in hydrocarbon flames; 2) the fluorescence signals from HCO are strongly quenched [114]; and 3) the accessible electronic transitions of HCO are predissociative [123]. However, high-quality PLIF images of CH_2O and OH can be acquired with relatively standard laser-based imaging systems (for combustion research facilities, at least). Additionally, through proper excitation schemes (which are similar to those implemented here; see below) the product of LIF signals of CH_2O and OH are proportional to the forward reaction rate of the aforementioned elementary reaction [114]. Thus, in principle by taking the product of simultaneously acquired PLIF images of CH_2O and OH one can generate an image in which the signal correlates well with the HRR (i.e. that provides a visualization of the reaction layer).

By applying the overlap-method to quasi-laminar, premixed flames, Paul and Najm [107] were the first to experimentally demonstrate that overlap-layers correlate well with the primary heat release regions in such flames. Since their study, others [108–110] also showed good agreement between overlap-layers and the region of heat release in flames. Based on these findings, numerous investigations [13, 19, 111–117, 124] have utilized the overlap-method to visualize reaction layers in turbulent flames. While concerns regarding the fidelity of the overlap-method have been raised [17, 19, 21, 121], recent DNS studies by Aspden et al. [30] and Wang et al. [45] showed a strong correlation between heat release rate and overlap-layers in turbulent premixed dodecane– and methane–air flames, respectively. Furthermore, the comparisons between overlap- and CH-layers provided in Section 3.6 demonstrate that

this technique is a robust tool for visualizing reaction layers within highly turbulent premixed methane-air flames.

High-resolution overlap-layer images were acquired in this study by implementing the diagnostic configuration depicted in Fig. 2.4.

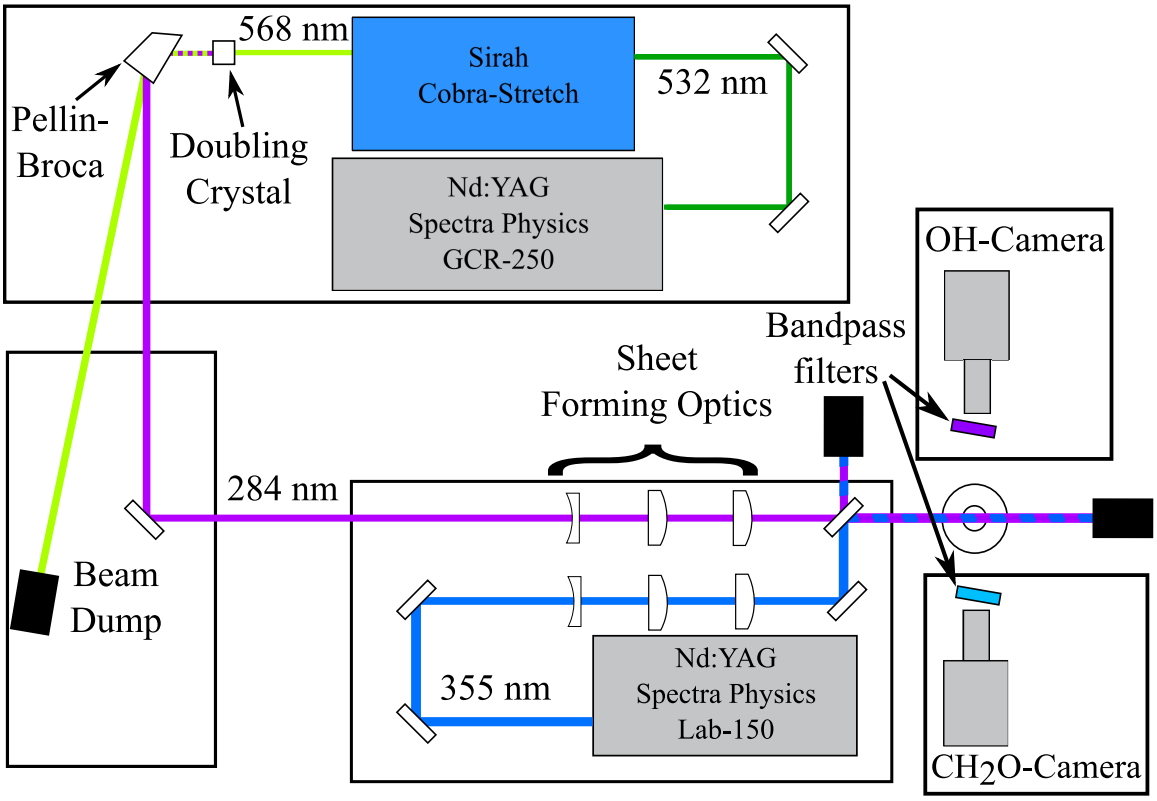

Figure 2.4: Schematic of the diagnostic configuration to acquire overlap layers at the University of Michigan.

Excitation of CH_2O was accomplished by pumping a series of pP and pQ transitions within its 4_0^1 vibration band [125]. This was achieved via a laser sheet near 355 nm that contained pulse energies of ∼125 mJ. This laser sheet was produced by frequency-tripling the output from an Nd:YAG laser (Spectra-Physics Lab 150) and sending the resulting beam through a series of sheet forming optics (see Fig. 2.4). Broadband fluorescence from the CH_2O molecules (∼370 nm to ∼530 nm) was collected by an intensified charge-coupled device (ICCD) camera (Andor iStar) that was mounted perpendicular to the laser sheet and was equipped with a Nikon 105-mm f/2.8 lens

and two Semrock filters (BLP01-364R and FF01-533/SP), which blocked elastically scatter laser-light. As is indicated in Fig. 2.4, fluorescence from OH radicals was collected by a second ICCD camera (Andor iStar) mounded opposite the CH_2O-camera. The OH-camera was fitted with a Cerco 100-mm f/2.8 lens and a Asahi Spectra 310 ±5-nm bandpass filter. Note that in an effort to minimize the collection of chemiluminescence signal, the gate time for both cameras was set to 100 ns. The OH radicals were excited by pumping the $P_2(4)$ transition of the (1,0) band in the $A^2\Sigma^+$–$X^2\Pi$ system of OH via a laser sheet near 284 nm. To generate this sheet, an Nd:YAG (Spectra-Physics GCR 250) pumped dye laser (Sirah Cobra-Stretch) system generated a beam near 568 nm, which was frequency doubled to produce a beam near 284 nm with pulse energies of ∼4 mJ. The overlapping 568-nm and 284-nm beams were then passed through a Pellin-Broca prism that separated them and directed the 284-nm beam through a series of sheet forming optics. Additionally, a portion of the residual 568-nm beam was monitored by a HighFinesse WS-6 wavelength meter in order to ensure the wavelength of the excitation sheet remained consistent.

After passing through their respective sheet forming optics, the 284-nm and 355-nm sheets were combined via a short-wave pass dichroic mirror and were carefully overlapped at three separate points: on centerline and 150 mm ahead of and behind the burner. Furthermore, the spatial overlap of these sheets was verified after every sample was collected to ensure that it was maintained throughout the entire duration of data collection. Note that to prevent cross talk between the two laser-based imaging systems, a temporal delay of 250 ns was set between the pulses of the 284-nm and 355-nm sheets. Both of these sheets were 36 mm tall and were measured (via a scanning knife-edge) to be ∼0.2 mm thick. A sheet height of 36 mm was chosen so that they would cover the entire FOV imaged by the cameras, which was approximately 30 mm (tall) × 30 mm (wide). Two separate FOVs were used for imaging overlap-layers; their locations relative to the burner are depicted in Fig. 2.2 and they are referred to

as Z1OL and Z2OL (short for Zone 1 and Zone 2 overlap, respectively).

2.2.2.2 Planar Laser Induced Fluorescence of CH and combined CH-OH

The second technique employed here for visualizing reaction layers involved CH-PLIF imaging. Like the overlap technique, CH-PLIF imaging has been used by many researchers [15, 17–19, 21, 108, 126–131] to visualize reaction layers within turbulent flames. This is because CH is a short-lived radical and, as Fig. 2.3 indicates, its spatial distribution does a reasonable job of tracking the heat release rate in methane–air flames [45, 108, 119]. While in all of those prior studies CH-PLIF was conducted via transitions in either the $A^2\Sigma^+$–$X^2\Pi$ (0,0) or $B^2\Sigma^-$–$X^2\Pi$ (0,0) bands, here it was facilitated via excitation of and detection from transitions in the (0,0) band of the CH $C^2\Sigma^+$–$X^2\Pi$ system (near 314 nm) [105, 106, 132]. Owing to the relatively large absorption and emission coefficients of transitions in the CH C–X (0,0) band [133], the primary benefit of this unique approach to CH-PLIF imaging is that high-quality images (e.g. signal-to-noise ratios > 10) can be acquired with relatively low laser pulse energies (e.g. $\sim$0.2 mJ/pulse) (or laser fluence 1.6×10^{-3} J/cm^2) [105, 106]. This suggests that a continuously pulsed Nd:YAG pumped dye laser system, which currently provide less than 1 mJ/pulse after frequency-doubling [105], could be used to acquire high-quality CH-PLIF images at kHz rates. Indeed, by utilizing a continuously pulsed Nd:YAG pumped dye laser system to excite transitions in the C–X (0,0) band of CH, Carter et al. [105, 106] demonstrated that one can obtain high-quality CH-PLIF images at a rate of 10 kHz. The technique developed and employed by Carter et al. [105, 106] was also implemented here. Thus, unlike the overlap-layer images, which were acquired at a low rate (i.e. 1.6 Hz), here CH-PLIF images were obtained at a rate of 10 kHz (i.e. at high-speed).

Beyond permitting high-speed CH-PLIF imaging, the aforementioned diagnostic technique possesses an additional benefit. Specifically, as was first alluded to by Jef-

feries et al. [133], through a judicious choice of excitation transitions and filtering schemes one can use that technique to obtain CH- and OH-PLIF images either simultaneously or separately with a single laser and camera configuration. To illustrate this, consider the computed excitation spectrums (generated via LIFBASE [35]) for CH and OH in Fig. 2.5, which also displays sample PLIF images corresponding to three separate target transitions.

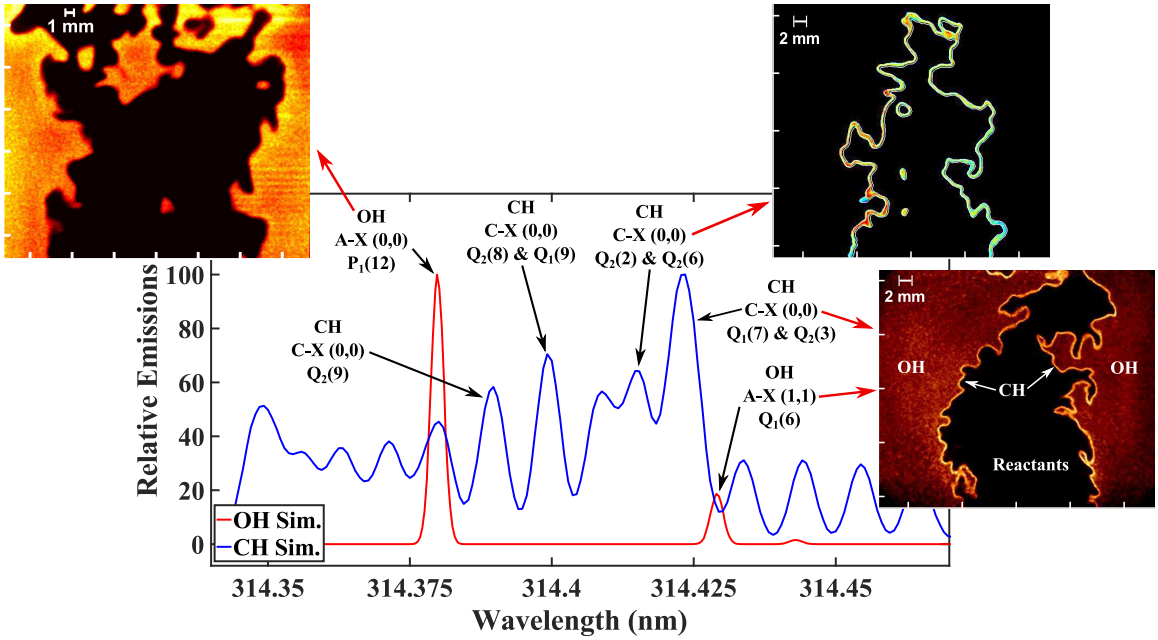

Figure 2.5: Computed spectrum of the CH CX and OH AX systems [35] as well as sample PLIF images.

Figure 2.5 clearly indicates that two OH lines are located near the primary Q-branch transitions of the CH C–X (0,0) band. However, as Fig. 2.5 shows, and as was demonstrated by Carter et al. [105, 106], by tuning to the overlapping $Q_2(2)$ and $Q_2(6)$ transitions in the (0,0) band of the CH C–X system (at 314.415 nm in air), one can obtain high-quality CH-PLIF images void of OH-LIF signal. On the other hand, OH-PLIF images, void of CH-LIF signal, can be acquired by tuning to the $P_1(12)$ transition in the (0,0) band of the OH A-X system (at 314.380 nm in air). Finally, as Carter et al. [105, 106] showed, by tuning the output of the dye laser near 314.426

nm (in air) one can excite the CH C–X (0,0) Q-branch band-head (composed of the $Q_1(7)$ and $Q_2(3)$ transitions) and the $Q_1(6)$ transition in the in the OH A-X (1,1) band. As the sample image in the lower right hand corner of Fig. 2.5 shows, this allows one to acquire images containing both CH- and OH-LIF signal.

This latter fact is what facilitated the third reaction layer imaging technique employed here, which was the acquisition of images containing both CH- and OH-LIF signals at a rate of 10 kHz. Specifically, by simply tuning the output of the dye laser used to conduct high-speed CH-PLIF imaging (see below) from 314.415 nm (in air) to 314.426 nm (in air), we were able to go from acquiring images that exclusively contained CH-LIF signal to those that contained both CH- and OH-LIF signals. Figure 2.6 presents a sample image acquired from our Case2A-1.05 that exhibits the result of exciting the CH C-X (0,0) Q-branch band-head and the $Q_1(6)$ transition in the OH A–X (1,1) band with a 314.426-nm laser sheet.

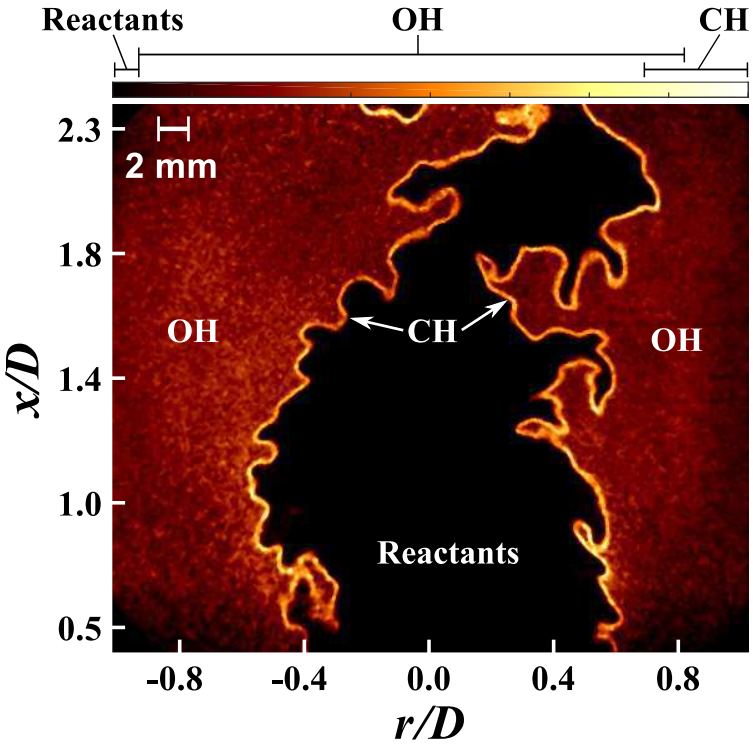

Figure 2.6: Sample combined CH-OH PLIF image from Case2A-1.05. Note that D = 21.6 mm, is the inner diameter of the nozzle at the Burner's exit.

The advantage of capturing both OH- and CH-LIF signals within the same image is that it allows one to visualize the reaction layer structure while also being able to clearly distinguish reactants from products. This feature is particularly advantageous when imaging cases with extreme turbulence levels because they become so convoluted that it is impossible to separate products from reactants with CH-PLIF images alone (e.g. see Fig. 2 of Ref. [132]). Furthermore, since this combined CH-OH technique was also conducted at a rate of 10 kHz, it allowed us to observe the temporal evolution of interactions between CH-layers and cool product gasses (inferred from low OH-LIF signals), which, as will be shown in Section 4.4, is the primary cause of local extinction in this experiment.

The diagnostic configuration employed in this dissertation to conduct PLIF imaging of CH and CH-OH at a rate of 10 kHz is presented in Fig. 2.7.

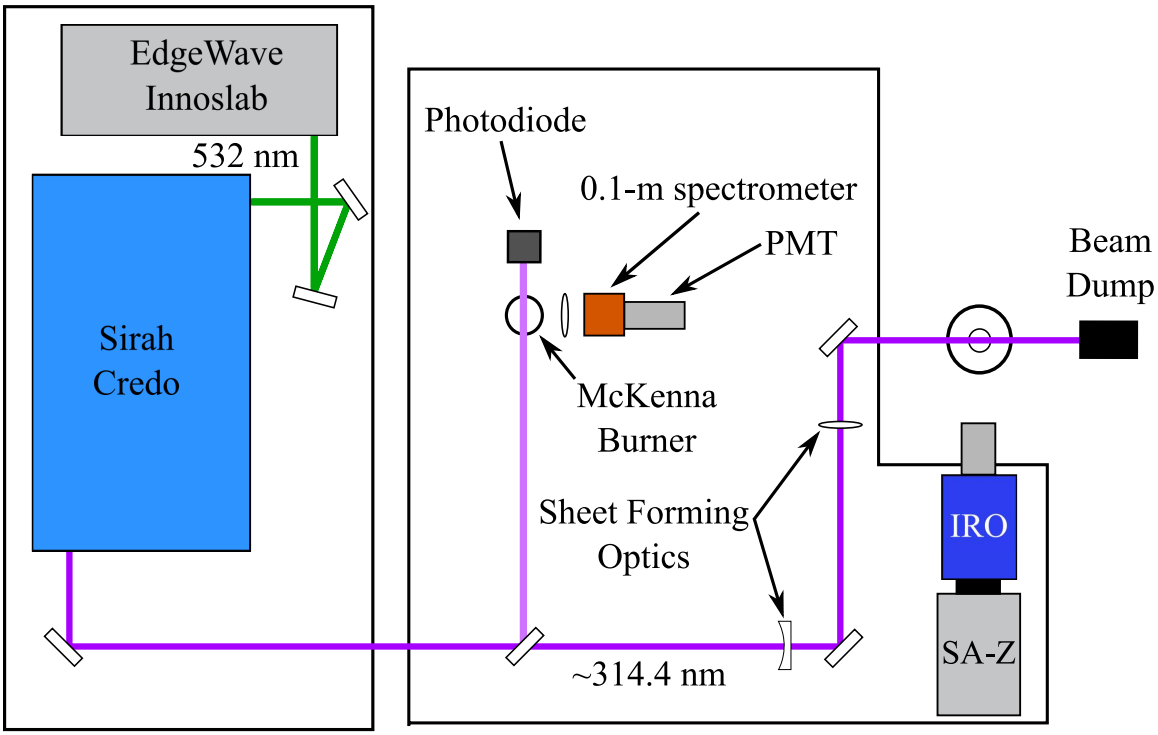

Figure 2.7: Schematic of the diagnostic configuration to acquire CH-PLIF images at a rate of 10 kHz. Note that PMT stands for photomultiplier tube.

Specifically, CH-PLIF imaging at a rate of 10 kHz was facilitated by pumping the overlapping $Q_2(2)$ and $Q_2(6)$ transitions in the (0,0) band of the CH $C^2\Sigma^+$–$X^2\Pi$ system with a 314.415-nm laser sheet. By tuning that laser sheet to 314.426 nm (in air), the setup depicted in Fig. 2.7 also permitted the acquisition of PLIF images containing both CH- and OH-LIF signals at a rate of 10 kHz. The sheet was approximately 50 mm tall and 0.23 mm thick, and, as Fig. 2.7 suggest, was formed by passing the frequency-doubled output of an Nd:YAG (EdgeWave Innoslab) pumped dye laser (Sirah Credo) system through a series of sheet forming optics. Resonant fluorescence from the target species was collected with a high-speed CMOS camera (Photron SA-Z) equipped with a HS-IRO (LaVision), a Cerco 100-mm f/2.8 lens, a UG-5 glass filter, and a 1-m focal length UV close-up lens. The locations of the four separate FOVs imaged by this camera are presented in Fig. 2.2. As can be seen, these FOVs were approximately 47 $\times$ 47 mm^2 in size and they are referred to as ZnCH, with n = 1, 2, 3, and 4.

A noteworthy feature of the diagnostic setup utilized here is that a portion of the frequency-doubled output from the dye laser was directed over a Mckenna Burner. This was done in order to correct for any offsets in the frequencies determined by the control system for the dye laser, which subsequently ensured that the laser sheet was tuned to the correct transition. Specifically, fluorescence resulting from passing the pick-off beam through the product region of a methane-air flame stabilized on the Mckenna Burner was monitored by a 0.1-m spectrometer equipped with a photomultiplier tube (PMT) and set to detect fluorescence from transitions in the OH A–X (1,0) band (near 283 nm). Thus, by locating the $P_1(12)$ transition in the (0,0) band of the OH A–X system, we were able to determine and account for the offset of the control system for the dye laser.

2.2.2.3 Preheat Layer Imaging

As discussed in Section 1.3, the preheat layer is the region just upstream of the reaction layer where the temperatures are elevated above those corresponding to the reactants [47]. Therefore, acquiring images of preheat layers can be achieved by either imaging the temperature field directly or, as is the case for reaction layers, imaging a suitable surrogate. Rayleigh scattering imaging is a common means by which temperature images can be acquired from flames (e.g. Refs. [2–7, 11, 13, 17–19, 111, 124, 134, 135], to list a few). However, because Rayleigh scattering signal is collected at the same wavelength as the incident radiation from the laser, this technique is susceptible to interference from elastically scatter later light (e.g. Mie scattering) [136][1].

An alternative approach to imaging preheat layers is through PLIF imaging of CH_2O [21]. Specifically, the experimental observations and numerical results presented by Li et al. [21] suggest that CH_2O-LIF signals can serve as a marker of the preheat zone in methane–air flames. This is further corroborated by the simulated results in Fig. 2.8, which demonstrate that the spatial region over which CH_2O concentrations are high correlate well with the region of elevated temperature that lies just upstream of the reaction layer.

[1] Note, however, that this is not the general case and that filtered Rayleigh scattering techniques have been developed and implemented (see, for example [137])

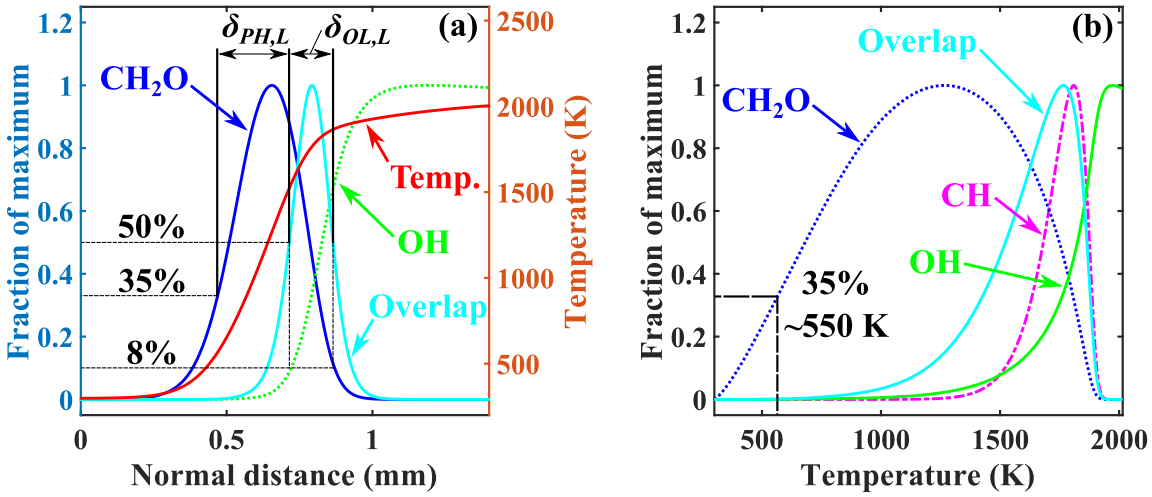

Figure 2.8: Profiles of key intermediate species to methane–air combustion that highlight our definitions for preheat and reaction layer thicknesses. Profiles were derived from a 1-D freely propagating CHEMKIN simulation of a premixed methane–air flame with $\phi = 1.05$. The chemical kinetic mechanism utilized in this simulation was GRImech 3.0 [34].

For this reason, and because CH_2O-PLIF is required to obtain overlap-layers, in this dissertation preheat layer information is derived from CH_2O-LIF signals. An additional reason for this is that deriving preheat zone information from CH_2O-LIF signals utilized to generate overlap-layers allows one to explicitly distinguish preheat and reaction layers as is consistent with classical laminar flame theory [47]. Moreover, since CH_2O-LIF signals can be imaged in a non-resonant fashion, with proper filtering, this technique is not as susceptible as Rayleigh scattering imaging is to interference from elastically scattered laser light.

As is depicted in Fig. 2.8a, in this dissertation the upstream boundary of the preheat layer is marked by the location where the CH_2O-LIF signals first exceed 35% of a local maximum value on the reactant side (i.e. away from OH-LIF signal). The downstream boundary of the preheat layer is define by the cool-edges of the overlap-layers. The edges of overlap-layers are defined as the location where the overlap-signal falls below 50% of a local maximum value (see Section 3.1.1 for details), and the cool edge is identified as the one furthest from relatively high OH-LIF signals. The reason

the 35% value was chosen to mark the upstream boundary is because, as Fig. 2.8b shows, the point where CH_2O concentrations first exceed 35% of their maximum value in a simulated laminar flame corresponds to a temperature of ∼550 K. The aforementioned definition for the trailing edge of the preheat zone was chosen so that the preheat and reaction layers could remain as separate entities as they are in classical laminar flame theory [47]. Admittedly, justification for this definition is not the most compelling since it is merely based on rather anecdotal evidence from Li et al. [21] and results derived from a simulated laminar flame. Thus, Rayleigh scattering images were acquired simultaneously with PLIF images of CH_2O to solidify the use of CH_2O-LIF signals as a preheat zone marker. Results from such simultaneous imaging are provided in Section 3.5 and they clearly indicate that the approach adopted here for preheat layer imaging is robust.

Though preheat heat layer information was derived from the overlap-method in this dissertation, a larger FOV than that employed to acquire high-resolution overlap-layer images was necessary to image the preheat layers of the flames considered here in their entirety. This is a consequence of the fact that the preheat layers of the flames considered here often filled the entire central core of the flame brush, which could be anywhere from 20 mm to 30 mm wide. Yet, beyond a different FOV size, a completely different diagnostic configuration than that described and portrayed in Section 2.2.2.1 was used to obtain preheat layer images. A schematic of the optical setup utilized for preheat layer and Rayleigh scattering imaging is displayed in Fig. 2.9.

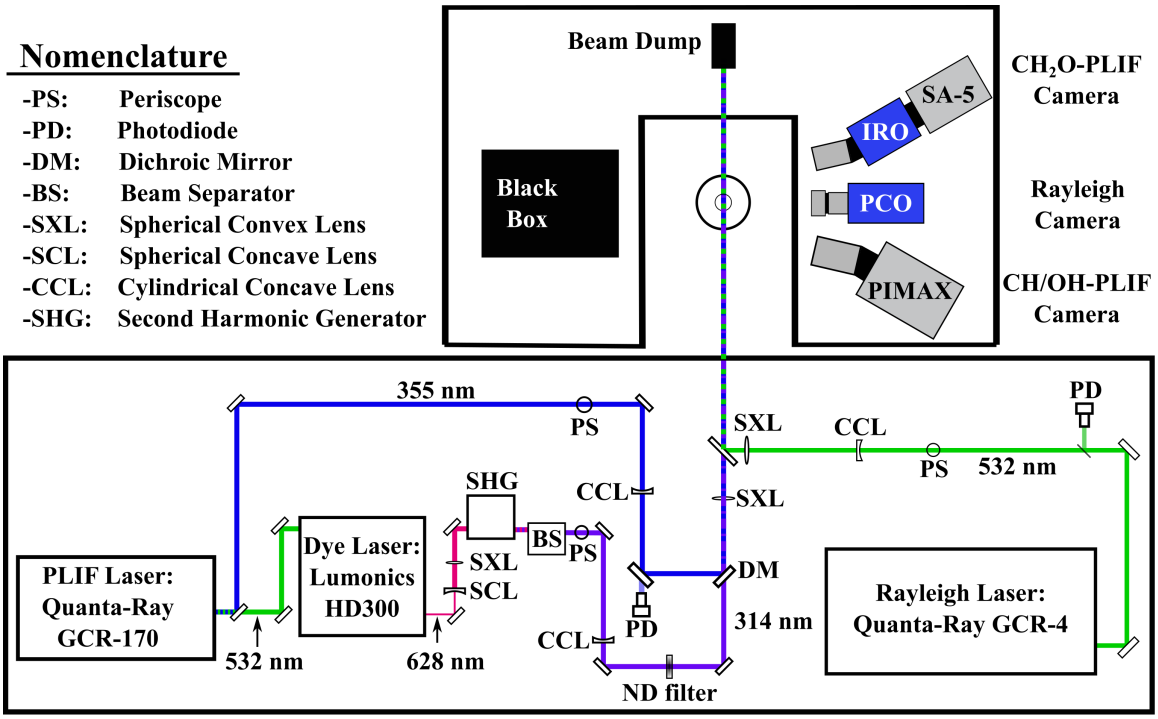

Figure 2.9: Schematic of the diagnostic configuration employed to acquire Rayleigh scattering images simultaneously with preheat layers at AFRL.

The sketch in Fig. 2.9 indicates that the primary diagnostic tools used to conduct simultaneous Rayleigh scattering and preheat layer imaging (i.e. simultaneous Rayleigh/CH_2O-/OH-PLIF imaging) included two Nd:YAG lasers, a dye laser, two intensified cameras, and one un-intensified camera. One of the Nd:YAG lasers (Quanta-Ray GCR-4) was used as the light source for the planar Rayleigh scattering measurements. Specifically, the s-polarized, 532-nm output from that laser, having pulse energies of 630 mJ, was formed into a 40 mm (tall) $\times$ 0.16 mm (thick) sheet. The resulting Rayleigh signal was imaged by an un-intensified camera (PCO 1600) mounted perpendicular to the plane of the laser sheet; gating for this camera was set to 500 ns. This camera was equipped with two separate lenses: a Nikon Noct-Nikkor (58-mm f/1.2) and a Rodenstock (210-mm f/4.5). The Nikon lens was mounted directly to the PCO camera in a standard fashion, while the Rodenstock lens was mounted such that its front was attached to the front of the Nikon lens. Further-

more, sandwiched between these two lenses was a 532-nm bandpass filter (Semrock FF01-532/3-50).

In addition to permitting simultaneous Rayleigh scattering and preheat layer imaging (i.e. simultaneous Rayleigh/CH_2O-/OH-PLIF imaging), the diagnostic configuration in Fig. 2.9 also facilitated the simultaneous acquisition of Rayleigh scattering, CH_2O-, and CH-PLIF images via a slight shift in the wavelength of the output from the dye laser. The ability to make such multi-scalar measurements with relatively standard diagnostic equipment was made possible by the novel approach to acquiring CH-PLIF images described in Section 2.2.2.2. In fact, as Fig. 2.9 indicates, three separate PLIF measurements were facilitated by a single Nd:YAG (Quanta-Ray GCR-170) pumped dye laser (Lumonics HD300) system. Specifically, the frequency-tripled output from this Nd:YAG laser (near 355 nm), having pulse energies of ∼180 mJ, was used to excite CH_2O molecules, while its frequency-doubled output (near 532 nm) was used to pump the dye laser. The 628 nm output from the dye laser was frequency doubled to generate a laser beam near 314 nm with ∼3 mJ/pulse. Note, however, that the energy in this beam was reduced by directing it through an ND filter (OD 0.5); thus, after losses due to reflections and significant expansion, the pulse energy within the probe region was ∼0.5 mJ. Both the 355-nm and ∼314-nm beams were formed into ∼40 mm tall sheets that were 0.12 mm and 0.29 mm thick, respectively, and were overlapped by passing the ∼314-nm beam through a shortwave-pass dichroic mirror. These overlapped sheets were then combined with the 532-nm sheet used for Rayleigh scattering by passing them through a standard 532-nm mirror with a fused-silica substrate.

To permit preheat layer imaging, CH_2O- and OH-PLIF images were acquired simultaneously by tuning the output from the dye laser to the $P_1(12)$ transition in the (0,0) band of the OH $A^2\Sigma^+$-$X^2\Pi$ system (at 314.380 nm in air). The PLIF images were captured by two separate ICCD cameras that were mounted on the same side

of the laser sheet as the Rayleigh scattering camera (one on either side of it). As Fig. 2.9 shows, all three of these cameras "looked into" a "black box" (ThorLabs), which helped minimize background scattering. To facilitate this configuration, the two PLIF cameras were mounted at an angle of ∼20° with respect to the normal of the laser sheet. Furthermore, both cameras were equipped with a Schiempflug mount so that their focal planes could be made coincident with the laser sheets. The ICCD camera (PIMAX III) used for OH-PLIF (and CH-PLIF) imaging was gated to 100 ns to minimize chemiluminescence signal. This camera was fitted with a Cerco f/2.8 100-mm lens, a 500-mm focal length UV close-up lens, and a 325 +/- 20 nm bandpass filter. The reason for including the bandpass filter was to isolate the CH and OH fluorescence from Rayleigh/elastic scattering from the 355-nm sheet, which was temporally overlapped with the 314-nm sheet. CH_2O fluorescence was imaged by a Photron SA-5 camera, which was equipped with a HS-IRO (LaVision), a Nikon f/2.8 105-mm macro lens, and two Semrock filters (BLP01-364R and FF01-533/SP); gating for this system was also set to 100 ns. Though a high-speed camera was used for CH_2O-PLIF imaging, all of the preheat and Rayleigh scattering images were acquired at a rate of 10 Hz. Finally, preheat layer information was acquired from four separate FOVs; their locations relative to the burner are depicted in Fig. 2.2, and they are referred to as ZnPH, with n = 1, 2, 3, and 4.

2.3 Summary of diagnostic details

For convenience, a summary of the details regarding the four separate diagnostic tools implemented in this dissertation is provided in Table 2.4. Specifically, Table 2.4 presents estimations for the in- and out-of-plane resolutions and signal-to-noise ratios (SNRs) of all of the image types gathered in this study. Note that for the PLIF images the SNRs were determined after median filtering was applied and that they were computed by dividing the average signal within a region by the standard

deviation of the signal within that region.

Diagnostic			Resolution (μm) Individual (Ind.)		Result	SNR	
Primary	Und.	Rate	In-plane	Out-of-plane	In-plane	Ind.	Result
Overlap	CH_2O	1.6 Hz	130	200	150	~14	~6
	OH		150	200		~20	
Preheat	CH_2O	10 Hz	210	120	210	~17	~17
	OH		210	190		~25	
CH	NA	10 kHz	190	250	NA	~14	NA
CH-OH	NA	10 kHz	190	250	NA	~16	NA
Rayleigh	NA	10 Hz	64	160	NA	R: ~40	P: ~25

Table 2.4: Diagnostic details. Nomenclature: Und. stands for Underlying, which signifies the underlying diagnostic for derived quantities; Ind. stands for Individual; the "R" and "P" indicate the SNRs in the reactants and products, respectively, for the Rayleigh scattering images. The in-plane resolutions represent the FWHM of the line spread functions (LSFs) associated with each imaging system (prior to the application of filters). Details regarding the methods used to determine those values are provided in 3.3.1. The out-of-plane resolutions represent the thickness (FWHM) of the laser sheets, which were determined via a scanning knife-edge method.

The out-of-plane resolutions listed in Table 2.4 represent the full width at half maximum (FWHM) of the laser sheets, which were measured via a scanning knife-edge technique. The in-plane resolutions provided in Table 2.4 represent the FWHM of the line spread functions (LSFs) associated with each imaging system. Three separate approaches for determining these values were taken. For the overlap images, the in-plane resolution is taken to be the larger of the two in-plane resolutions associated with the high-resolution OH- and CH_2O-PLIF imaging systems (see Section 2.2.2.1), where the resolutions of those images were determined via the methods outlined in Refs. [138–140] (see 3.3.1 for details). The in-plane resolution of the preheat layer images represents the resolution of the CH_2O-PLIF images they were derived from (see Section 2.2.2.3), which was determined by comparing target images acquired with this system to those that were fully resolved (see 3.3.1 for details). Finally, the

in-plane resolution of the CH-PLIF images was determined by integrating the signal from small dust particles (see 3.3.1 for details) to identify the LSF associated with this imaging system. It is important to note that, due to aliasing, the latter two approaches are likely to produce over estimations [139, 140].

CHAPTER III

Image Processing and Assessment of Flame Visualization Techniques

From medical examination scans to satellite imagery, the ability to acquire meaningful information from images plays a pivotal role in modern day science. Nevertheless, obtaining such information, particularly in an automated fashion, is a challenging task. It requires the ability to filter, manipulate, and accurately segment portions of digital images. Fortunately, over the past 50 years the field of digital image analysis has developed a plethora of tools that enable such image handling. The challenges, however, are identifying the correct tools for a particular situation and combining multiple sets of those tools in ways that 1) provide accurate information; 2) enhance, rather than diminish the quality of the images being analyzed; and 3) can be automated. Since the primary data obtained in this dissertation is in image form, such challenges were overcome to extract statistical information from them.

The first portion of this Chapter (i.e. Sections 3.1 to 3.3) is dedicated to presenting the details of the image processing schemes that were implemented in order to extract meaningful information from the PLIF images acquired in this dissertation. Following the presentation of those details, the reliability of the processing schemes applied to the PLIF images is assessed. Of course, the accuracy of the results presented in this dissertation not only rests on the reliability of the specific post processing methods

that were implemented but also on the uncertainties in the measurements themselves. Thus, uncertainties in the PLIF measurements are discussed and presented in Section 3.3.

The second part of this Chapter (i.e. Section 3.4) provides details regarding the steps that were taken to convert Rayleigh scattering images into temperature field images. A discussion of the resolution and uncertainty in those measurements are also provided in this portion of the Chapter. Finally, the last segment of this Chapter (i.e. Sections 3.5 and 3.6) presents an assessment of the validity of the techniques that were implemented to visualize the preheat and reaction layers of the flames considered in this study.

3.1 Processing schemes for PLIF images

In general, standard image processing schemes as well as a novel local thresholding algorithm were implemented to extract preheat and reaction layer thickness from the images obtained in this dissertation. However, the fact that two separate diagnostic tools and three separate optical configurations were implemented to acquire those images rendered it impossible to obtain average preheat and reaction layer thicknesses with a single processing algorithm. In the sections that follow, details of the various processing schemes that were utilized to extract preheat and reaction layers are described. First, Section 3.1.1 presents the standard and novel processing schemes used to obtain average reaction layer thicknesses. Then, details regarding the acquisition of average preheat layer thicknesses are discussed in Section 3.1.2. Finally, the reliability of the processing schemes implemented in this dissertation are assessed based on laminar flame measurements in Section 3.2.

3.1.1 Processing to obtain reaction layer thicknesses

In order to extract statistical information from the images collected in this dissertation, both standard and novel image processing schemes were implemented. The standard techniques applied to the high-resolution CH_2O- and OH-PLIF images (i.e. for generating overlap-layers; see Section 2.2.2.1) included the following. First, they were binned 2×2 (before readout) to an array size of 512×512 pixels, which, based on Fig. 2.2, indicates that the pixels within these images covered an area of 59×59 μm^2. Then, in order to remove contributions from chemiluminescence, elastically scattered laser light, and dark current within the ICCD cameras, average background fields were subtracted from each raw image (I_{raw}) via an equation similar to the one prescribed by Clemens [139][1]. Namely, background signals were removed from the raw high-resolution CH_2O- and OH-PLIF images through the following equation:

$$I_e = \frac{I_{raw} - ((\overline{I_{FB}} + \overline{I_L}) - \overline{I_D})}{\overline{I_{SC}}}, \tag{3.1}$$

where the symbol $\overline{(\cdot)}$ indicates an average quantity, (I_e) is the expected LIF signal intensity, $\overline{I_{FB}}$ represents the average of images acquired with the flame present yet without incident laser radiation (i.e. it accounts for the average chemiluminescence signal), $\overline{I_{LB}}$ signifies the average of images acquired while the laser sheet was present but the flame was extinguished (i.e. it accounts for signal stemming from scattered laser light), $\overline{I_D}$ represents the average of images obtained with a cap on the camera lenses (i.e. it represents an average measure of the signal associated with dark current within the ICCD cameras), and $\overline{I_{SC}}$ is an average image that corrects for inhomogeneities in vertical profile of the laser sheets. To obtain $\overline{I_{SC}}$, the laser sheets were sent through an optically thick solution (i.e. a highly concentrated mixture of

[1]The difference between Eq. 3.1 and that suggested by Clemens [139] is that Eq. 3.1 does not incorporate a white field (or flat-field) correction

Rhodamine 6G and Ethanol) contained within a dye cell and subsequently imaged by the PLIF cameras. Two hundred of these images were acquired for each laser sheet and were subsequently averaged to generate images such as those in Fig. 3.1. Vertical profiles were then generated from those average images by integrating them in the radial direction and subsequently dividing the resulting profiles by their respective maximum intensity values. Sample profiles, as well as those obtained in the same manner from the PLIF images of the target species, are provided in Fig. 3.1. The good agreement between the separate profiles indicates that the corrections were accurate.

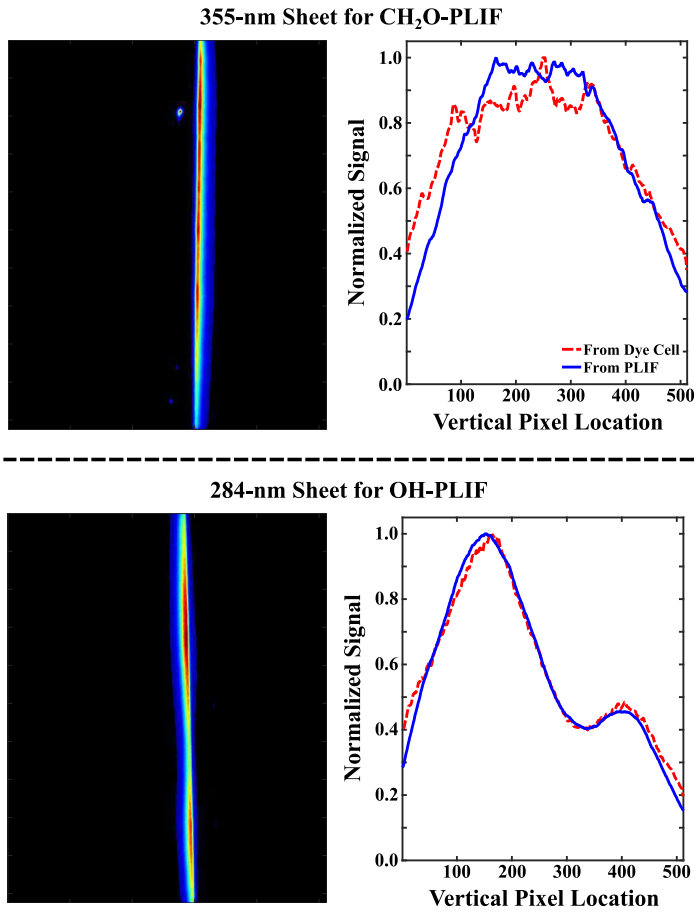

Figure 3.1: Average images of the 355-nm and 284-nm laser sheets used for the high-resolution CH_2O- and OH-PLIF images, respectively. The profiles to the right of each image was obtained by integrating those images in the horizontal direction. Note, vertical profiles derived from the respective LIF signals are also included in the plots.

Following the aforementioned corrections, the high-resolution CH_2O- and OH-PLIF images were subjected to 5-pixel-radius median and level-set filtering [141]. After this filtering, the OH-PLIF images were registered to the CH_2O-PLIF images via a transform generated by identifying the same points on a thin transparent target that was aligned with the laser sheets and imaged by both cameras. The accuracy of this registration process was assessed by comparing the transformed target image acquired by the OH-camera to the one captured by the CH_2O-camera. In doing so, this registration process was deemed accurate to within one pixel (i.e. 59 μm). After the OH-PLIF images were registered to the CH_2O-PLIF images, they were multiplied together to produce "raw" overlap-layer images.

A similar series of standard processing techniques were applied to the CH-PLIF images. For instance, they were binned 2×2 to an array size of 512×512 pixels, thus each super pixel within them spanned an area of 91×91 μm^2. Additionally, once background signal was removed from them, they were subjected to 5-pixel-radius median filtering. However, level-set filtering was not applied and the background signal was not removed via Eq. 3.1. Instead, a single value, determined from the median signal in regions generally void of CH-layers, was subtracted from each image. Note that this value was generally only $\sim$10% of the average CH-LIF signal, which is consistent with a signal-to-background ratio of 10%, as was typical of the CH-PLIF images acquired here. Another difference was that correcting for the non-uniformities in the laser sheet that facilitated CH-PLIF imaging was accomplished by dividing the PLIF images by a profile generated from the average CH-LIF signal. This type of sheet correction is justified by Fig. 3.1, which indicates that the corrective profiles used on the CH_2O- and OH-PLIF images closely matched the profiles derived from the average signal in those images. Furthermore, unlike the high-resolution CH_2O- and OH-PLIF images used to generate overlap data, these CH-PLIF images were flat-field corrected by dividing them by an average image derived from a set of images

of a uniformly illuminated white background.

In addition to these standard image processing steps, an additional novel local thresholding scheme was implemented to identify the boundaries of the reaction layers. These boundaries are defined by the location where the CH-LIF and overlap signals first exceed 50% of a local maximum value. The thresholding scheme to identify these boundaries consisted of 3 primary steps, which are depicted in Fig. 3.2.

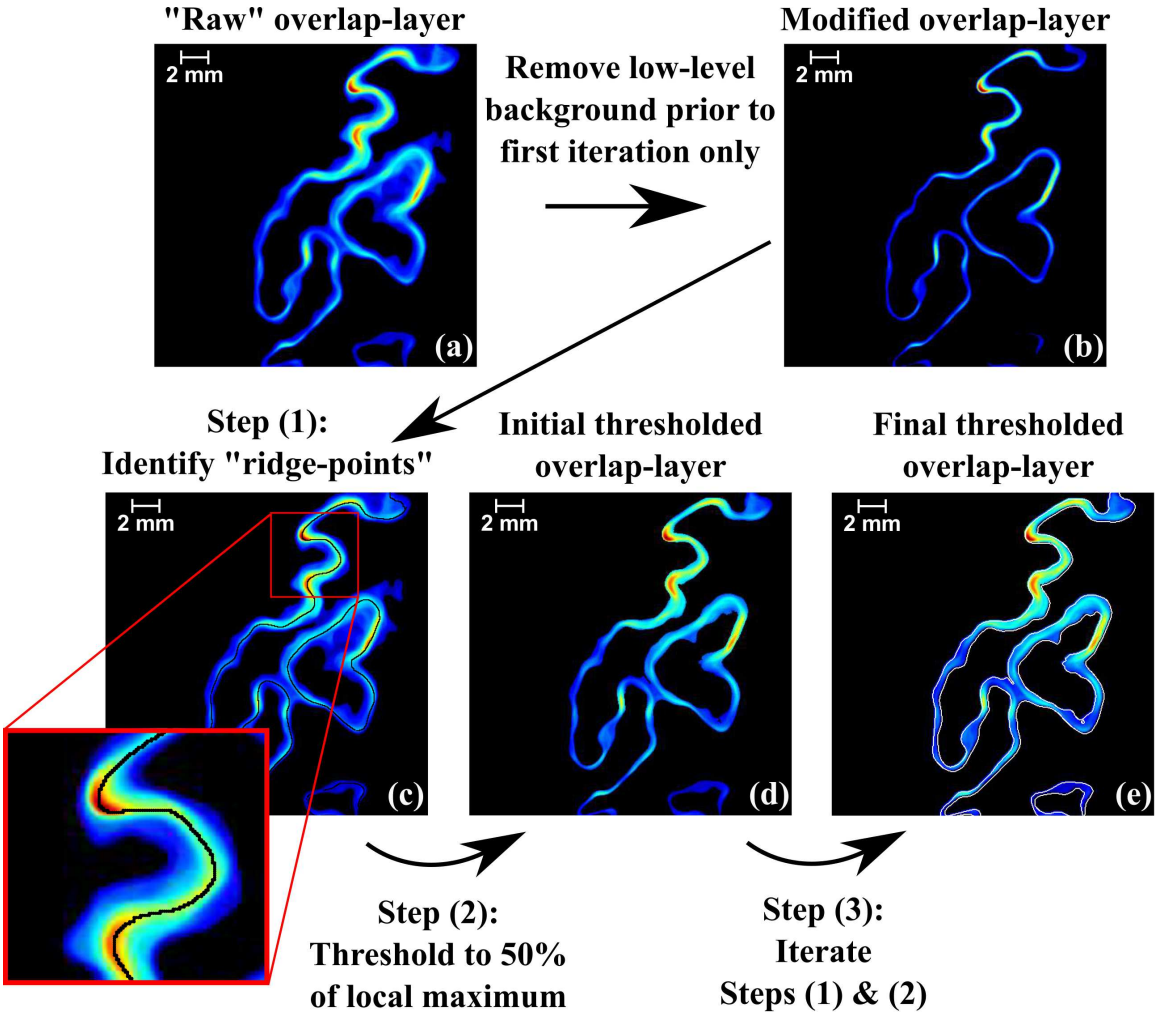

Figure 3.2: Diagram demonstrating the novel thresholding process applied to a sample overlap-layer.

In step (1), the loci of points that follow the maximum contours of the CH and overlap-layers are identified via a watershed algorithm [142, 143]. These points will be referred to as "ridge-points" and examples of them are highlighted by the black line

in Fig. 3.2c. Step (2) involves locally thresholding the reaction layers with respect to the signal values at these ridge-points. Specifically, if the signal at a particular pixel is less than half of the signal at the ridge-point nearest it, its signal is set to zero, otherwise it is left alone. Finally, step (3) is to iterate through steps (1) and (2) two additional times, using the output from the previous iteration for the current one. A final sample of a thresholed overlap-layer is shown in Fig. 3.2e.

Note, however, that the watershed algorithm will identify ridge-points for all non-zero regions within an image, even if those regions merely represent spurious background signal. Therefore, in an effort to improve the accuracy of identifying the initial ridge-points, in the first iteration they were obtained from overlap and CH-PLIF images that had low-level signal removed. Although it should be noted that the images with this low-level signal removed were not used for anything other than simply identify the initial ridge-points. Removal of this low-level background signal was accomplished by subtracting a percentage of the maximum value in each row from that row in each CH-PLIF and overlap image. This subtraction was performed on a row-by-row basis because it was a relatively simply way to remove low-level background signal while still accounting for vertical variations in signal intensity. An example of an overlap image that has had this signal removed is exhibited in Fig. 3.2b.

Beyond facilitating localized thresholding, this local thresholding scheme also permitted the automated computation of average preheat and reaction layer thicknesses. This was achieved by binarizing the thresholded images and applying a morphological function (from the Image Processing toolbox of Matlab [143]) to them to identify their skeletons. An example of a binarized overlap-layer and its corresponding skeleton are shown in Fig. 3.3a.

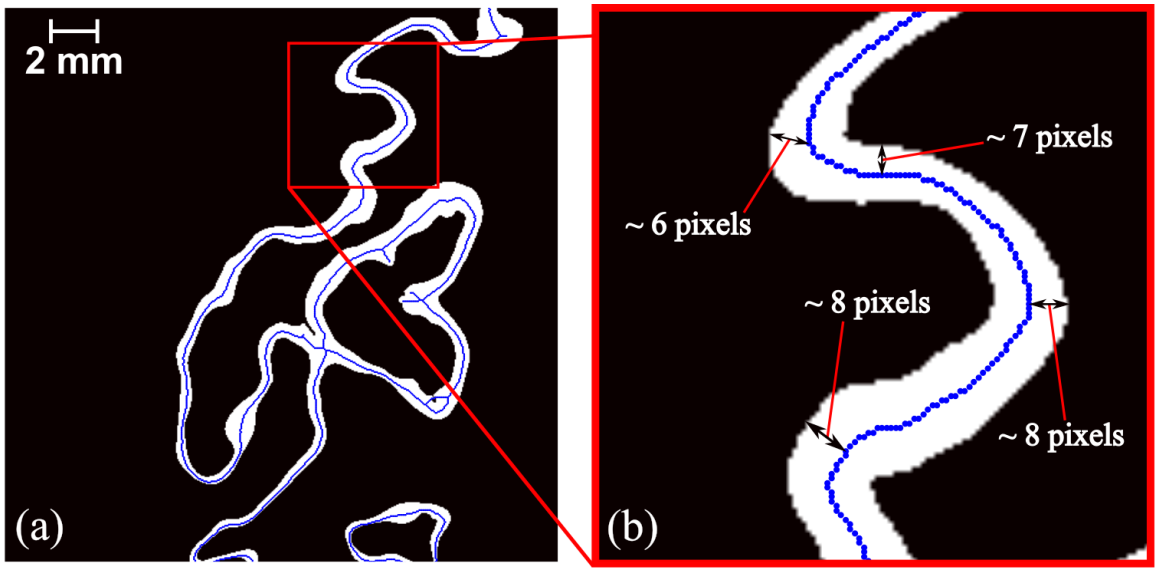

Figure 3.3: Sample binarized overlap-layer with its skeleton in (a), and a close-up highlighting the skeleton and the distance between it and the nearest thresholded edge in (b).

Once the skeleton of a layer was identified, the distance from each point on it to the nearest point on the boundary of the thresholded layer was determined (see Fig. 3.3b). Since the reaction layers were thresholded to 50% of a local maximum value and since the skeletal-points lie in the center of each layer, multiplying these distances by 2 and the pixel length for that image gives the FWHM of the layer at that point. Subsequently, these FWHM values were accumulated to generate probability density functions (PDFs) for each case studied here. Given that there were over 1500 skeletal-points in each CH-PLIF and overlap image and that 400 overlap and 4084 CH-PLIF images were collected in each case, these PDFs comprised of over 600,000 data points. Once these PDFs were generated, their most probable value was identified and was used to represent the "average" reaction layer thickness associated with a particular case. The reason for determining average reaction layer thicknesses in this way is that, as was pointed out by Dinkelacker et al. [7] and as is demonstrated Section 3.3.3, the most probable value of a 2-D thickness PDF is a good approximation of the average 3-D layer thickness.

3.1.2 Processing to obtain preheat layer thicknesses

Average preheat layer thicknesses were obtained through a similar, yet, slightly different image processing scheme. Like the CH-PLIF images and those used to generate the high-resolution overlap-layer images, the CH_2O- and OH-PLIF images used to produce preheat layer images were binned 2×2 to an array size of 512×512 pixels. Since the FOVs imaged by these CH_2O- and OH-cameras were approximately 33 mm (tall) $\times$ 40 mm (wide) implies that the area of each of their super pixels was approximately 64×78 μm^2. One difference between the processing of the CH_2O- and OH-PLIF images used to produce preheat layer images (see Section 2.2.2.3) and those used to generate high-resolution overlap-layers was that, in the former, flat-field corrections were applied and laser sheet corrections were based on average LIF signals (i.e. as was the case for the CH-PLIF images). Another difference was that after invoking Eq. 3.1 to remove background signals, but prior to registration and multiplication, an additional percentage (5% for CH_2O and 1% for OH) of the *global* maximum value in each image was subtracted from that image. Local thresholding was also applied to these images (i.e. steps (1)–(3) above), which removed any remaining OH- and CH_2O-LIF signal that was below 8% of a local maximum value. The reason a value of 8% was chosen for this was because, as Fig. 2.8 indicates, concentrations of OH and CH_2O below 8% of their respective local maximum values do not contribute to the FWHM of the overlap-layer. Furthermore, the reason this additional subtraction/thresholding was required is because simply subtracting average background fields in the manner described in Eq. 3.1 did not remove all of the background signal from these images. This latter point is illustrated and discussed in Appendix B.

After the aforementioned processing was applied to the CH_2O- and OH-PLIF images they were filtered (same as for the high-resolution overlap-layers) and registered to one another. This registration process was carried out in the same manner as

that described in Section 3.1.1 and was again deemed accurate to within one pixel (i.e. ∼71 μm). Following those steps, the CH_2O- and OH-PLIF images were multiplied together to produce overlap-layers, which were subsequently thresholded to 50% of their local maximum values. Once these overlap-layers were produced and thresholded, the CH_2O-PLIF images used to generate them were locally thresholded (via steps (1)–(3) above) such that signal below 35% of a local maximum value was removed. Then the regions of the thresholded overlap-layers that laid on top of the CH_2O layers were removed from them so that only the preheat layers remained (see Section 2.2.2.3 for the preheat layer definition invoked in this dissertation). These preheat layers were then binarized, their skeletons were identified, and the thickness at each skeletal-point was determined as it was was for the reaction layers. Additionally, like the reaction layers, the average preheat layer thickness of a case was represented by the most probable value of the PDF of preheat layer thicknesses accumulated over each skeletal-point and image in that case. Since each preheat layer image contained ∼2,500 skeletal-points and 300 images were collected for each case, those PDFs were derived from over 600,000 data points.

3.2 Reliability of PLIF processing schemes

To assess the reliability of the previously described algorithm, it was first applied to laminar flame measurements. Specifically, the thicknesses obtained from applying the algorithm to those measurements, which are listed in Table 2.2, were compared to thicknesses derived from manual profiles taken normal to the preheat and reaction layers of those flames. Sample PLIF images from laminar flames with $\phi = 1.05$ and profiles taken normal to their layers are depicted in Fig. 3.4.

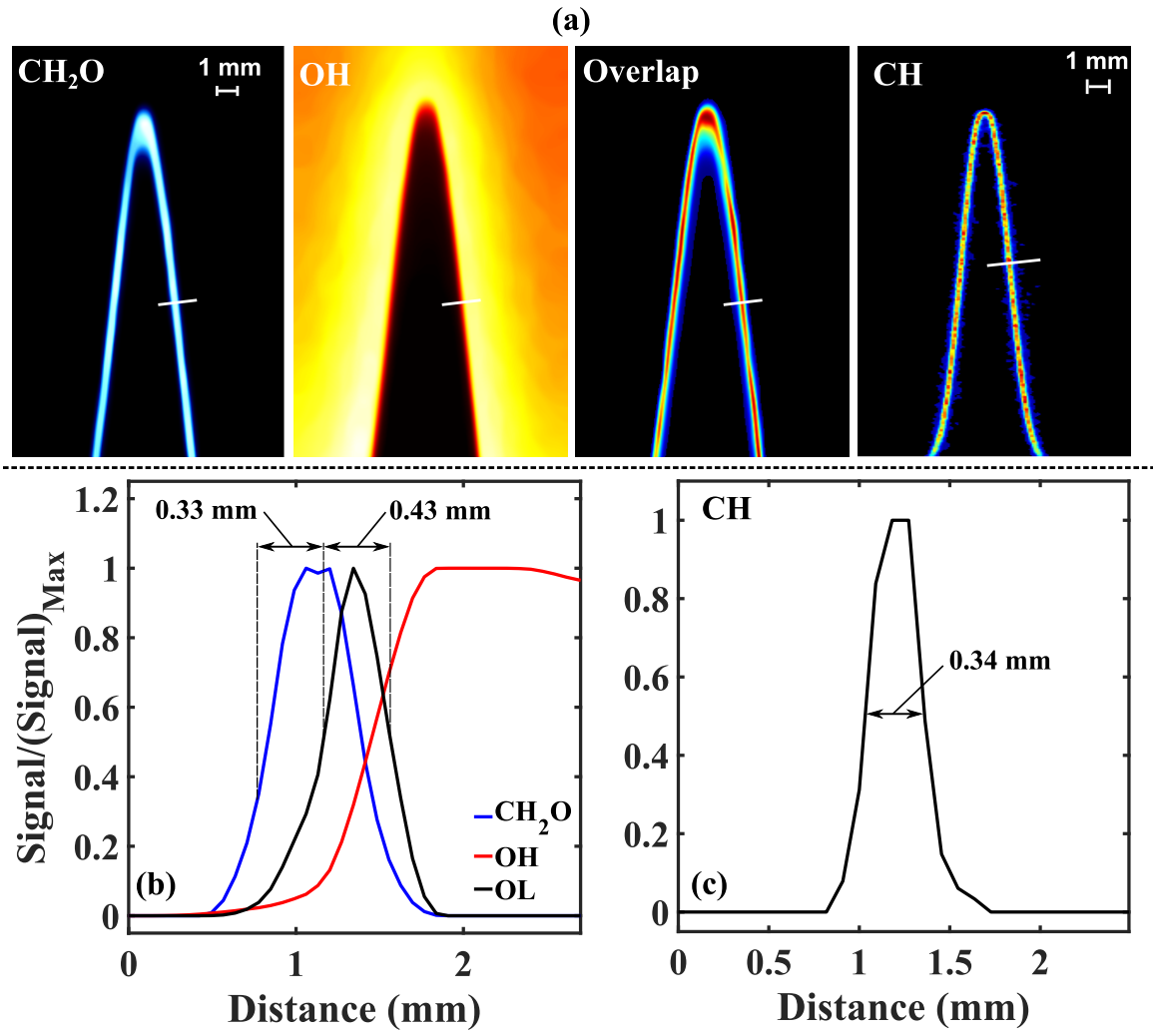

Figure 3.4: (a) Sample laminar images acquired with $\phi = 1.05$. (b) Profiles taken along the white line in the CH_2O/OH/overlap series of PLIF images. (c) Profile of CH-LIF signal taken from the white line in the sample CH-PLIF image.

As Fig. 3.4 suggest, the thicknesses derived from the manually acquired profiles were fairly consistent with the values obtained via the algorithm outlined above. In fact, the percent difference between the average of thicknesses acquired from 10 to 20 of such profiles and those listed in Table 2.2 was ~5%. This indicates that the aforementioned processing steps are a reliable means by which average preheat and reaction layer thicknesses can be extracted from PLIF images in an automated fashion.

3.3 Uncertainties for the PLIF measurements

Beyond the reliability of the processing schemes outlined above, there are several factors that limit the accuracy of measuring the preheat and reaction layer thicknesses of the flames considered in this dissertation. The main three factors (i.e. sources of uncertainty) include: finite resolution limits (briefly discussed in Section 2.2), non-ideal background subtractions, and the fact that a 2-D technique is used to measured a 3-D value (i.e 3-D effects). The relative errors associated with these limitations are presented in Table 3.1, and the complex details of how they were determined are described below. Based on the error estimates provided in Table 3.1, it is likely that the true thicknesses of the preheat, CH-, and overlap-layers were not fully resolved. However, to the best of the authors' knowledge, no experimental studies have been performed in which the imaging systems were capable of fully resolving laminar preheat (based on CH_2O-PLIF), CH-, and overlap-layers without any specific post-processing schemes. Moreover, significant insight can be gained by comparing the thicknesses measured from the turbulent cases to those acquired from laminar flames, which is done in Section 4.3.

Error type	Overlap	CH	preheat
Finite resolution (%)	17	38	24
Background Subtractions (%)	14	3	6
3-D effects (%)	3	6	5

Table 3.1: Relative errors in determining the Overlap-, CH-, and preheat layer thickness as a result of finite resolution limits, non-ideal background subtractions, and 3-D effects.

3.3.1 Finite resolution limits

As mentioned in Section 2.2, the in-plane resolutions of the imaging systems used to acquire the overlap, preheat, and CH-PLIF images were characterized by

the FWHM of the line spread functions (LSFs) associated with those imaging systems. Since overlap images are obtained by taking the product of CH_2O- and OH-PLIF images, directly determining the FWHM of the LSF associated with them is not trivial. Thus, we chose to represent the FWHM of the LSF associated with the overlap images as the larger of the two associated with the high-resolution OH- and CH_2O-PLIF imaging systems. To determine those values, we first used a scanning knife-edge technique [138–140] to obtain the discrete step response functions (SRFs) associated with the OH- and CH_2O-PLIF imaging systems. As was pointed out in Refs. [139, 140], one can obtain the LSF for an imaging system by differentiating the SRF for that system. However, because differentiation of discrete values can be rather noisy, here, as in Refs. [139, 140], an error function was fit to the SRFs and the LSFs were obtained by differentiating those fit functions. The SRFs, the functions fit to them, and the resulting LSFs for the high-resolution CH_2O- and OH-PLIF imaging systems are provided in Fig. 3.5a and 3.5b, respectively.

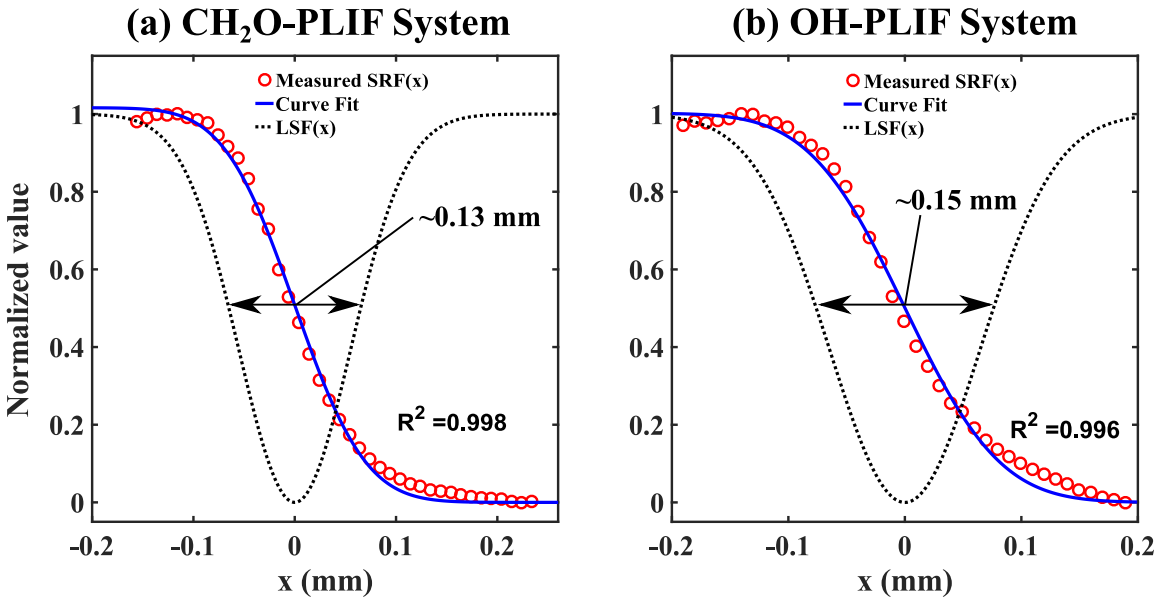

Figure 3.5: (a) SRF, an error funcntion fit to it, and the resulting LSF for the high-resolution CH_2O-PLIF imaging system used to generate overlap-layers. (b) SRF, an error funcntion fit to it, and the resulting LSF for the high-resolution OH-PLIF imaging system used to generate overlap-layer.

Based on Fig. 3.5, it is apparent that the OH-camera system possessed a slightly wider LSF than the CH_2O-camera system. Thus, the resolution of the overlap-layer images was taken to be the FWHM of the LSF associated with the OH-camera system, which was 150 μm.

Since CH_2O-LIF signals were used to mark the preheat layers of the flames considered here, the in-plane resolution of the preheat layer images is taken to be that of the CH_2O-PLIF images used to generate them (see Section 2.2.2.3). The FWHM of the LSF associated with this CH_2O-PLIF imaging system was determined by comparing a profile derived from a target image acquired with it to one derived from a target image taken with a high-resolution camera (Redlake EC16000) that was operated close to one-to-one (i.e. its resolution was $\sim$7.4 μm). The target images from the high-resolution and CH_2O-PLIF imaging systems, as well as the profiles obtained from them are provided in Figs. 3.6a, 3.6b, and 3.6c, respectively.

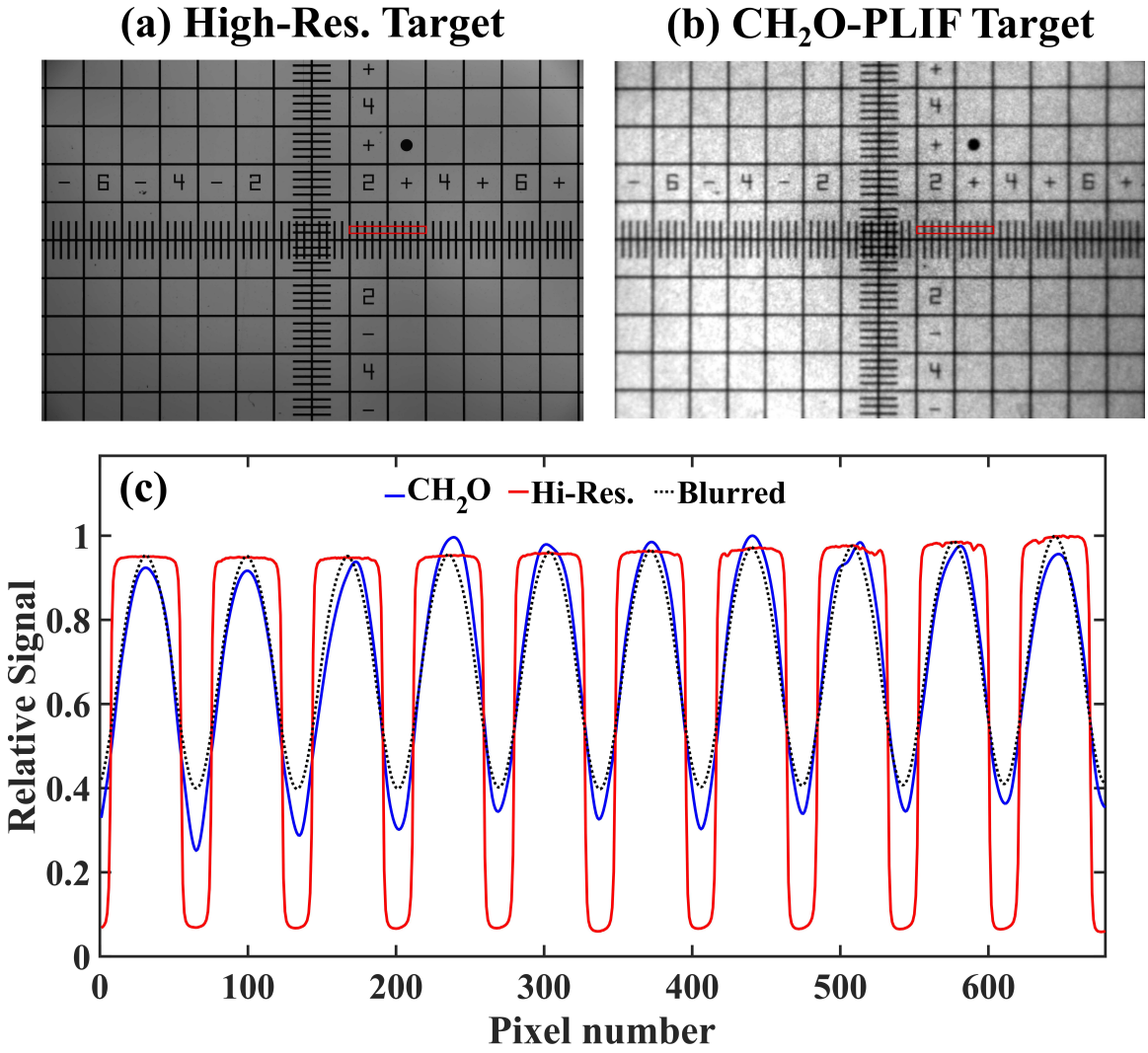

Figure 3.6: (a) Target image obtained with a high-resolution camera (Redlake EC16000) operated close to one-to-one (i.e. its resolution was ∼7.4 μm). (b) Target image acquired with the CH_2O-PLIF imaging system used to obtain preheat layer images (see Section 2.2.2.3). (c) A plot of profiles obtained by averaging over the vertical direction in the red rectangles in (a) and (b).

It is clear from Fig. 3.6c that the profile from the high-resolution target image is far sharper than the one from the target image acquired with the CH_2O-PLIF imaging system. However, as Fig. 3.6c shows, after applying a Gaussian blurring filter with a standard deviation (σ_{sd}) of 12 pixels (i.e. ∼89 μm) to the high-resolution target image, the profile obtained from it becomes very similar to the one from the CH_2O-PLIF imaging system. Because that Gaussian blurring filter represents a convolution

between the image and a Gaussian function with the user defined σ_{sd}, that Gaussian function behaved like a LSF (see Refs. [139, 140]). Thus, the input σ_{sd} that yields the best match between these profiles can provide an estimate for the FWHM of the LSF associated with the CH_2O-PLIF imaging system. Since, as Fig. 3.6c indicates, applying a Gaussian blurring filter with $\sigma_{sd} = 89$ μm to the high-resolution image generated profiles that closely matched those from the CH_2O-PLIF imaging system, the FWHM of the LSF associated with the latter is estimated to be 210 μm (i.e. FWHM $= 2.35\sigma_{sd}$).

The FWHM of the LSF associated with the CH-PLIF imaging system was obtained by considering the signal from small dust particles in the images. Recall that the CH-PLIF imaging technique implemented here is a resonant one, thus Mie scattering signal from small dust particles occasionally appeared in the PLIF images. Since those dust particles were much smaller than the resolution of the CH-PLIF imaging system (e.g. they were $\sim$0.5 μm in diameter), their resulting signals provided an approximation of the point spread function (PSF) associated with that system [139]. As was pointed out in Refs. [139, 140], the LSF is simply the integral of the PSF (see Eq. 11 of Ref. [140]). Therefore, as Fig. 3.7 illustrates, the FWHM of the LSF associated with the CH-PLIF imaging system was determined by: 1) integrating the signal from small dust particles over one direction; 2) subsequently fitting a Gaussian function to the results of that integration; and 3) identifying the FWHM of those Gaussian functions. This process was conducted for a total of 30 separate dust particles, and the FWHMs of their LSFs were averaged to yield a single value for the CH-PLIF imaging system, which was 190 μm.

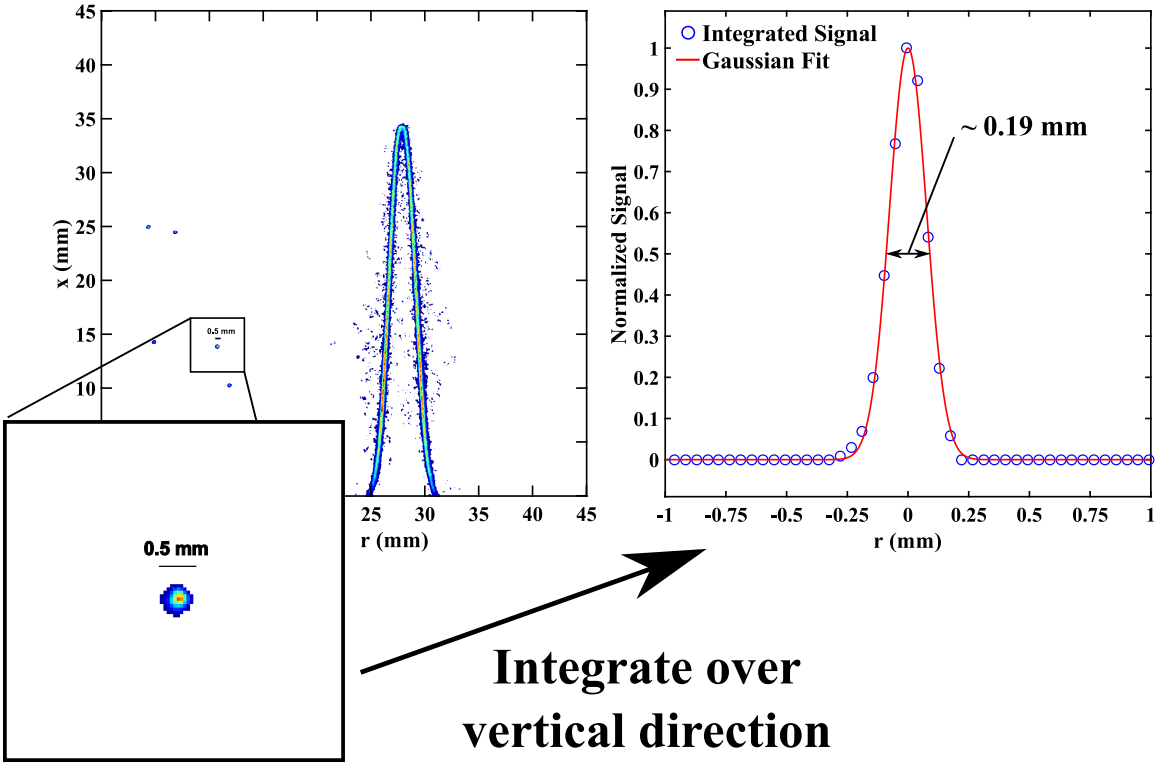

Figure 3.7: Image demonstrating how the LSF was determined from the CH-PLIF measurements.

According to Wang and Clemens [140], if one knows the FWHM (or standard deviation) of the LSF associated with their imaging system they can estimate the relative error in determining the thickness of a particular layer imaged with that system. Specifically, by using laminar CH- and overlap-layer thicknesses acquired from profiles taken normal to those layers[2] (e.g. as in Fig. 3.4), the FWHM of the LSF values in Table 2.4, and a modified version of Eq. 43 in Ref. [140], the relative error in determining the laminar CH- and overlap-layer thicknesses, as a result of finite resolution limits only, were found to be ∼38% and ∼17%, respectively. Because this method assumes that the layer in question is approximately Gaussian, it cannot be

[2]Note that because determining the FWHM of the LSFs from the aforementioned methods does not account for effects of filtering (i.e. median and level-set filtering), the thicknesses used to determine the relative errors were based on the FWHM of profiles taken normal to the layers with as little filtering as possible. The reason for using hand-drawn profiles rather than the algorithm here is because the algorithm struggles to properly identify local maximum points and subsequently threshold images when no filtering is applied.

used to provide a direct estimate of the relative error in measuring the laminar preheat layer thicknesses as they are defined here. However, because CH_2O-LIF signals were used to indicate the preheat layers of the flames considered in this study and because the profile taken normal to a laminar CH_2O-layer is approximately Gaussian (see Figs. 2.3 and 3.4), the average FWHM of such profiles was used to approximate the error associated with measuring the laminar preheat zone thicknesses. That relative error was determined to be $\sim$24%.

3.3.2 Sensitivity to background subtractions

In addition to the relative errors stemming from finite resolution limits, those resulting from the non-ideal background subtractions utilized in this study were also estimated. That is, because average and not instantaneous background images were subtracted from the raw CH_2O- and OH-PLIF images (see Eq. 3.1), it is likely that in many of the frames either too little or too much signal was removed. Moreover, in the case of the CH-PLIF images, a single value based on average background signal levels, rather than actual background images, was subtracted, and thus that value was like either too high or too low at various locations within each CH-PLIF frame. Of course, since in this dissertation the thickness of preheat and reaction layers are based on thresholding with respect to a local maximum value, imperfections in the background subtractions can impact the results.

To assess the sensitivity of thicknesses to varying levels of background subtraction, the percent increase (decrease) between thicknesses acquired from normal layers (again using hand drawn profiles as in Fig. 3.4) and those taken from layers wherein an additional amount of signal was subtracted (added) were determined. This additional amount was set to the total average standard deviation of the signal in the background images used to generate the background fields. For example, for the high-resolution CH_2O-PLIF images used to generate overlap-layers, the sum of the standard devia-

tions associated with $\overline{I_{FB}}$, $\overline{I_L}$, and $\overline{I_D}$, was ∼40 counts. For those CH_2O-PLIF images, 40 counts was ∼2% of the average CH_2O-LIF signal within them. Note, that in general, the percent of the average signal added or subtracted was between 1% and 3% of the average signal in their respective images. Also, because background images were not subtracted from the CH-PLIF images, the additional amount added/subtracted was set to twice the standard deviation of the background signal in regions void of CH-LIF signal. Again, these values were ∼3% of the average CH-LIF signal in those images. The percent increase/decrease values (which were typically within 1% or 2% of each other) determined from the aforementioned process are listed in Table 3.1. As can be seen, these values are between 3% and 14%, where the latter is for the overlap-layer thickness. It is somewhat expected that the overlap-layers would be the most sensitive to variations in background subtractions since the CH_2O- and OH-LIF signals that contribute to them are generally relatively low (see, for example, Fig. 3.4).

3.3.3 Error from 3-D effects

The final source of error considered in this study is that which stems from using a 2-D technique to measure an inherently 3-D quantity (i.e. preheat and reaction layer thicknesses). The thicknesses that are measured are merely the projection of the 3-D flame front onto a 2-D image, and thus are a function of the laser sheet thickness (δ_{LS}) and the flame crossing angle (α). A sketch depicting this issue is provided in Fig. 3.8.

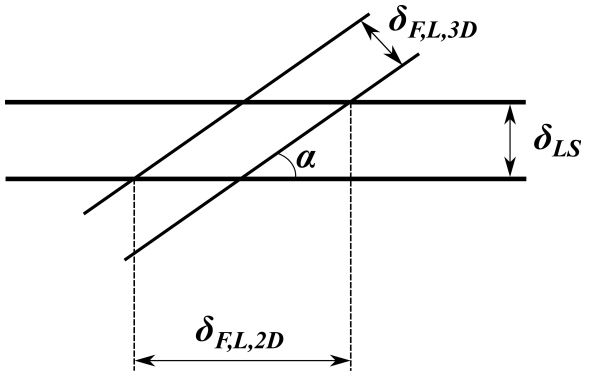

Figure 3.8: Sketch depicting the relationship between the actual 3-D thickness of a flame and that which is actually measured from a 2-D image.

The relationship between the 2-D flame thicknesses ($\delta_{F,L,2D}$) acquired from the images and the actual 3-D flame thicknesses ($\delta_{F,L,3D}$) is described by:

$$\delta_{F,L,2D} = \frac{\delta_{F,L,3D}}{sin(\alpha)} + \frac{\delta_{LS}}{|tan(\alpha)|}. \tag{3.2}$$

Notice that when setting $\alpha = 90°$ in Eq. 3.2, one finds that $\delta_{F,L,2D} = \delta_{F,L,3D}$ as expected. While α generally equals 90° in steady laminar flames, this is not the case once turbulence is intruded. In fact, since $\delta_{F,L,2D} \geq \delta_{F,L,3D}$, the average 2-D thicknesses determined in turbulent flames are often larger than the actual average 3-D thicknesses.

As mentioned in Section 3.1.1, the results of Dinkelacker et al. [7] suggest that one can minimize the discrepancy between the average 2-D thickness and the average 3-D thickness by using the most probable value of a 2-D thickness PDF to represent its average. This can be demonstrated analytically by considering normal distributions of $\delta_{F,L,3D}$ and α, where the average of those distributions are set to an average laminar layer thickness and 90°, respectively. Specifically, by plugging the values of those distributions into Eq. 3.2, one can generate a PDF of values for $\delta_{F,L,2D}$. An example of such a PDF is presented in Fig. 3.9a, while the normal distributions of $\delta_{F,L,3D}$ and

α used to generate it are exhibited in Figs. 3.9b, and 3.9c, respectively.

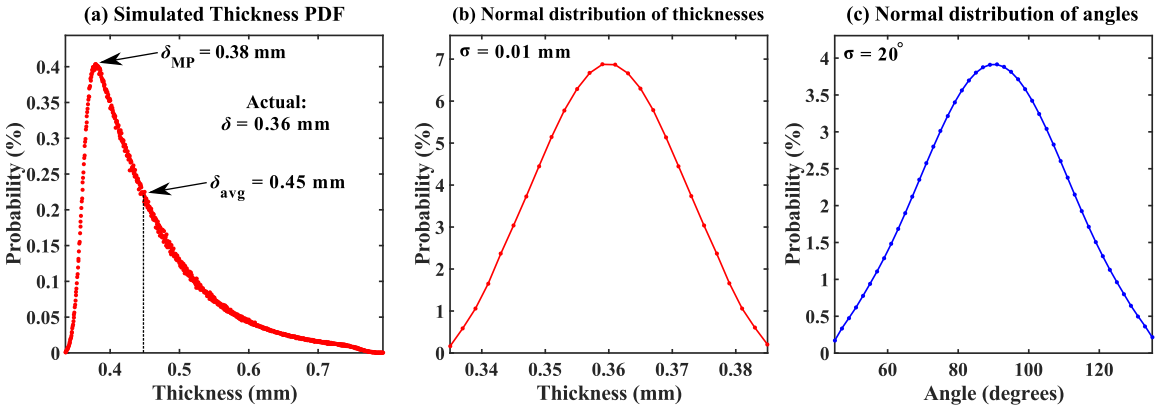

Figure 3.9: (a) Simulated PDF of thicknesses based on Eq. 3.2 and considering normal distrobutions of thicknesses (b) and angles (c) with standard deviations of 0.01 mm and 20°, respectively.

As can be seen, the PDF of $\delta_{F,L,2D}$ takes on a log-normal distribution, and hence the average value of this distribution is larger (up to ∼17%) than its most probable value (δ_{MP}). Yet, since the actual average 3-D thickness of the layer considered in constructing the PDF in Fig. 3.9a is known, we can compare that value to the δ_{MP} of that PDF. Clearly, δ_{MP} is a much better approximation of the average 3-D thickness than the average value of the PDF in Fig. 3.9a. To demonstrate that this approximation extends to the actual measurements, sample PDFs of measured preheat, overlap- and CH-layer thicknesses from Cases 1A-1.05 and 6A-0.85 are provided in Figs. 3.10a – 3.10f. Upon comparing Figs. 3.10a – 3.10f to Fig. 3.9a, it is apparent that the actual measured thickness distributions closely mimic the simulated one. For this reason, the most probable values of the 2-D thickness PDFs derived from the measurements were used to represent the average thickness values for each case.

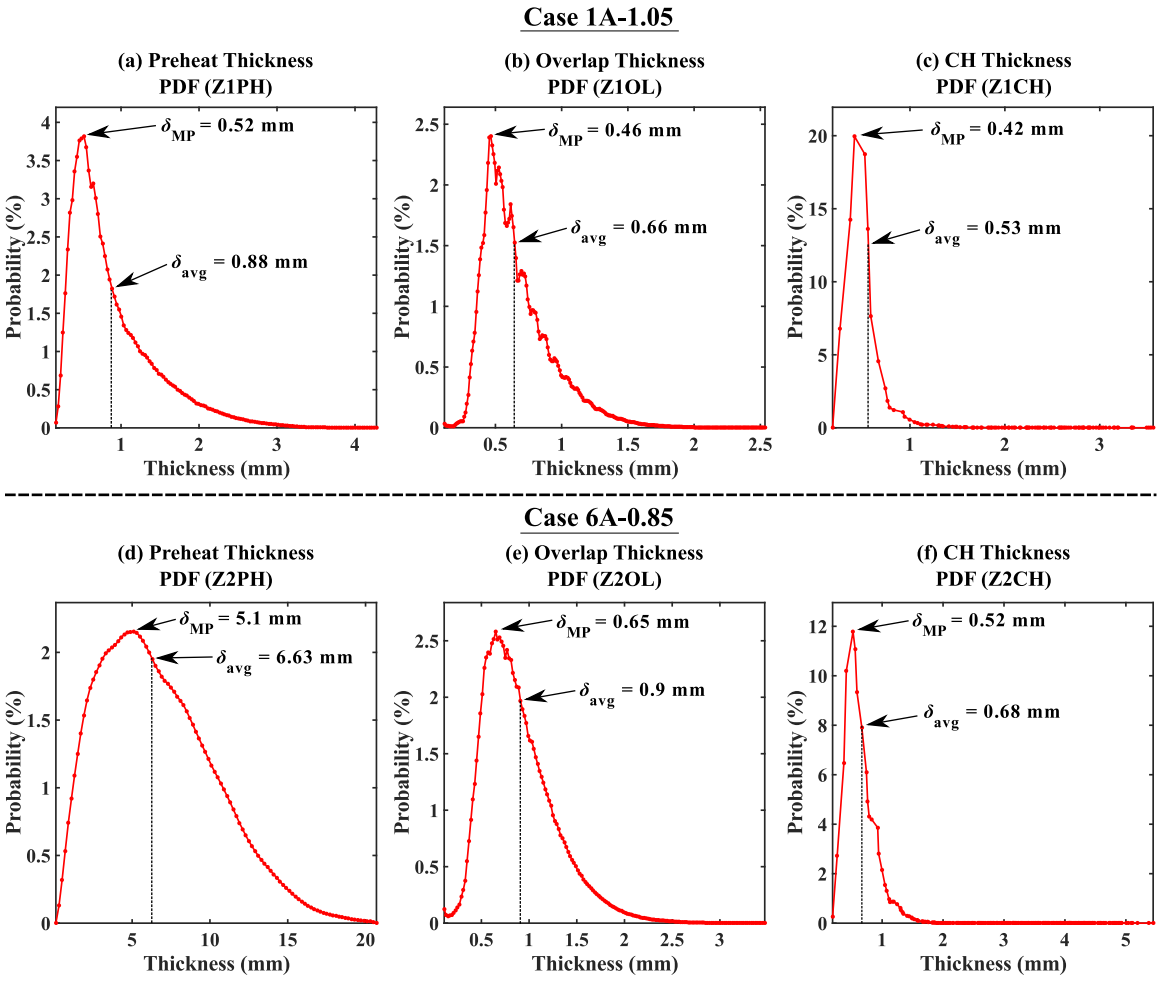

Figure 3.10: Sample PDF of preheat, overlap-, and CH-layer thicknesses from Case 1A-1.05 acquired from the lowest zones for each of those diagnostics in (a) – (c), respectively. Sample PDF of preheat, overlap-, and CH-layer thicknesses from Case 6A-0.85 acquired from the 2nd lowest zones for each of those diagnostics in (d) – (f), respectively.

While this approach certainly minimizes discrepancies between average measured $\delta_{F,L,2D}$ values and the actual average $\delta_{F,L,3D}$ value, it does not eliminate them entirely. Thus, to estimate the remaining uncertainty, PDFs like the one in Fig. 3.9a were generated by considering: 1) a Gaussian distribution of thicknesses with means set to the average measured layer thicknesses in Table 2.2 and standard deviations of 0.01 mm (which is approximately the standard deviation of the measured laminar overlap-layer thickness); 2) the laser sheet thicknesses in Table 2.4; and 3) a Gaussian

distribution of crossing angles with a standard deviation of 45 degrees. Specifically, the relative uncertainty estimates provided in Table 3.1, which range from 3% to 6%, represent the percent difference between the most probable value of those simulated PDFs and the known layer thicknesses in Table 2.2. Of course, such an approach is merely approximate; however, it does account for variations between the thicknesses of the separate layers as well as the varying sheet thicknesses used to measure them.

3.4 Rayleigh scattering measurement details

This section presents details regarding the conversion of Rayleigh scattering images into temperature field images and then provides a quantification of the resolution and uncertainty in these measurements.

3.4.1 Converting Rayleigh scattering signal into temperature

As mentioned in Section 2.2.2.3, many studies (see, for example, Refs. [2–7, 11, 13, 17–19, 111, 124, 134, 135]) have implemented Rayleigh scattering imaging to acquire temperature images from a wide range of flames. Accurately converting Rayleigh scattering images to temperature field images requires some effort though. The ability to perform this conversion rests on the principles of laser-based Rayleigh scattering [136, 144, 145] and the assumptions that: 1) the ideal gas law accurately describes the flow in question; and 2) that the pressure (P) is uniform throughout that flow. Rayleigh scattering theory describes the elastic scattering of light from particles with diameters that are much smaller than the wavelength of the incident radiation (e.g. from a laser) [136, 144, 145]. Under practical laser-based techniques (e.g. using the visible and ultra-violet (UV) outputs from pulsed Nd:YAG lasers) atoms and molecules constitute as such particles (i.e. their diameters are $\mathcal{O}(10^{-1})$ nm); thus, Rayleigh scattering signal can be acquired from a gas subjected to a sustained electromagnetic field (e.g. laser light).

The intensity of Rayleigh scattering signal (I_{Ray}) as a result of incident laser radiation through a gas is described by the following equation [134]:

$$I_{Ray} = C_{opt} I_{inc} N_0 \overline{\sigma_{mix}}, \tag{3.3}$$

where C_{opt} is a constant that incorporates factors relating to the efficiency of the optics and the collection volume, I_{inc} represents the intensity of incident laser light, N_0 is the number density of the gas, and $\overline{\sigma_{mix}}$ signifies the mixture-averaged differential Rayleigh scattering cross-section of the gas (see below for details). If the ideal gas law ($N_0 = P/kT$, where k is the Boltzmann constant, and T represents the temperature) accurately describes the flow in question, then Eq. 3.3 can be re-written as:

$$I_{Ray} = C_{opt} I_{inc} \frac{P}{kT} \overline{\sigma_{mix}}, \tag{3.4}$$

which, when solved for T, gives:

$$T = C_{opt} I_{inc} \frac{P}{k I_{Ray}} \overline{\sigma_{mix}}. \tag{3.5}$$

In order to utilize Eq. 3.5 to convert Rayleigh scattering signal acquired from a flame to temperature, P and C_{opt} must be accounted for. As mentioned above, the former is typically achieved by assuming that the pressure is constant throughout the flame and equal to that of the ambient environment. This, of course, is a fairly reasonable assumption for low Mach number flames that are open to the atmosphere, such as the ones considered in this dissertation. To account for C_{opt}, the Rayleigh scattering signal obtained from a flame is typically normalized by such signal acquired from a gas of known temperature and composition with the same optical configuration.

With this normalization, and assuming that P is the same in the flame and reference images, the equation for converting Rayleigh scattering signal to temperature is:

$$T_F = T_{ref} \frac{\overline{\sigma_F}}{\overline{\sigma_{ref}}} E_L \frac{I_{ref}}{I_F}, \tag{3.6}$$

where T_F is the measured temperature of the flame, T_{ref} is the known temperature of the reference gas (which is generally the same as that of the reactants within the flame), I_{ref} and I_F indicate the Rayleigh scattering signal intensities acquired from the reference gas and flame, respectively, E_L is the ratio of incident laser intensity between instances in which I_{ref} and I_F were obtained, and finally $\overline{\sigma_F}$ and $\overline{\sigma_{ref}}$ are the mixture-averaged differential Rayleigh scattering cross-sections for the flame and the reference gas, respectively.

In this dissertation, a slightly modified version of Eq. 3.6 was employed to convert Rayleigh scattering images to temperature field images. Specifically, the equation used here, which is similar to that employed by Yuen and Gülder [4] and Tamadonfar and Gülder [2], is:

$$T_F = T_0 \frac{\overline{\sigma_F}}{\overline{\sigma_A}} E_L \frac{\overline{I_A} - (\overline{I_D} + \overline{I_S})}{I_F - (\overline{I_{FB}} + \overline{I_S})}, \tag{3.7}$$

where the reference image ($\overline{I_A}$) was taken to be the average of 100 Rayleigh scattering images acquired in air (hence the "A," instead of "ref," subscripts) just downstream of the burner at a temperature of T_0, which was measured with a thermocouple. The terms $\overline{I_D}$ and $\overline{I_{FB}}$ in Eq. 3.7 are the same as those in Eq. 3.1, while the term $\overline{I_S}$ represents an average scattering background image. Here, as in Ref. [146], $\overline{I_S}$ was determined by acquiring Rayleigh scattering images in uniform fields of both air and helium and extrapolating to a zero Rayleigh scattering cross section. Note that the

average signal level in $\overline{I_S}$ was ∼40 counts, which is ∼2% of the average signal in $\overline{I_A}$. A final note regarding Eq. 3.7 is that the term E_L was based on the ratio of relative laser intensity (determined from the photodiode shown in Fig. 2.9) between each single-shot Rayleigh scattering image in the flame and the average intensity taken over the 100 images used to generate $\overline{I_A}$; note that the value of this term was never less nor greater than 0.94 and 1.06, receptively.

The mixture-averaged differential Rayleigh scattering cross-sections for the reference ($\overline{\sigma_A}$) and the flame ($\overline{\sigma_F}$) images were determined by solving the following equations:

$$\overline{\sigma_A} = \left(\sum_i \sigma_i \chi_i \right)_A , \tag{3.8}$$

$$\overline{\sigma_F} = \left(\sum_i \sigma_i \chi_i \right)_F , \tag{3.9}$$

where subscripts "A" and "F" indicate terms associated with air and the flame, respectively, and σ_i and χ_i represent the Rayleigh scattering cross-section and mole fraction of the ith species, respectively. A total of 4 (i.e. N_2, O_2, CO_2, and Ar) and 17 species were considered when determining $\overline{\sigma_A}$ and $\overline{\sigma_F}$, respectively. These species as well their Rayleigh scattering cross sections are listed in Table 3.2. The individual Rayleigh scattering cross-sections listed in Table 3.2 were determined via the manner outlined in Ref. [145]. Namely, for nearly every species considered, the following equation was solved:

$$\sigma_i = \sigma_{VV} + \sigma_{VH} = (1 + \rho_{\nu,i}) \frac{4\pi^2 (n_0 - 1)_i^2}{N_0^2 \lambda_{inc}^4} \left(\frac{3}{3 - 4\rho_{\nu,i}} \right) , \tag{3.10}$$

Species	σ_i/σ_{N_2}	$\rho_{\nu,i}$ $(\times 10^2)^{\ddagger}$	a_i $(\times 10^{12})^{\ddagger\ddagger}$	b_i $(\times 10^6)^{\ddagger\ddagger}$
N_2	1	1.0612	562.45	1.9097
O_2	0.859	2.9434	380.37	1.4334
CO_2	2.427	4.0798	686.50	1.5571
Ar	0.865	0	520.33	1.8768
H_2O-vapor	0.695	0.03	291.48	1.1869
CH_4	2.134	0.02	559.53	1.2964
CO	1.245	0.5132	404.39	1.2356
H_2	0.216	0.9044	187.53	1.3783
OH	1.486	0	105.76	0.3209
C_2H_4	5.803	1.2411	603.59	0.8721
He	0.013	0	134.89	3.893
HCN	1.689	0	488.79	1.2734
H	0.148	0	87.47	0.7839
NO	0.983	0	393.40	1.3648
O	0.171	1.54	71.63	0.6049
CH_3 †	1.577	0	525.39	1.4124
$CH_2O^{\dagger\dagger}$	1.990	0	-	-

Table 3.2: Chemical species and their differential Rayleigh scattering cross sections used to determine $\overline{\sigma_A}$ and $\overline{\sigma_F}$. ‡ The *depolarization* values ($\rho_{\nu,i}$) were taken from Table A.5 of Ref. [37]. ‡‡ The a_i and b_i values were taken from Table 1 of Gardiner et al. [38]. † Information for CH_3 was acquired from Table 2 and Table A.5 of Refs. [38] and [37], respectively. †† Information for CH_2O was acquired from Table A.5 of Ref. [37].

where σ_{VV} and σ_{VH} represent the Rayleigh scattering cross sections corresponding to vertically polarized incident laser light (i.e. as was the case in this study) and the resulting vertically and horizontally polarized scattering signals, respectively, λ_{inc} is the wavelength of the incident laser light (which was 532 nm in this study), $\rho_{\nu i}$ is the *depolarization* for specie i, and n_0 is the index of refraction. In order to solve Eq. 3.10, the values of $\rho_{\nu,i}$ were taken from Table A.5 of Ref. [37] and the quantity $(n_0 - 1)_i$ was determined for each species based on the following equation:

$$(n_0 - 1)_i = \frac{a_i}{b_i - \lambda_{inc}^{-2}}, \tag{3.11}$$

where a_i and b_i were taken from Table 1 of Gardiner et al. [38]. The only species

for which σ_i was not determined from Eqs. 3.10 and 3.11 was CH_2O; instead, its differential Rayleigh scattering cross section was taken to be that which is listed in Table A.5 of Ref. [37].

The method outlined above for determining the σ_i values is relatively insensitive to temperature variations across the flames considered here [145], thus it holds true in both their reactant and product fields. However, mole fractions of species obviously change quite considerably across a flame front. Hence, Eq. 3.9 implies that $\overline{\sigma_F}$ is not, in general, constant through a flame. To account for any variations in $\overline{\sigma_F}$, the species mole factions from the CHEMKIN simulations described in Section 2.1 were used to generate mapping relations between $\overline{\sigma_F}$ and the temperature through simulated laminar flames. These mapping relations are displayed in Fig. 3.11, which plots $\overline{\sigma_F}/\overline{\sigma_A}$ as function of the temperature through simulated laminar flames with the three equivalence ratios considered in this dissertation.

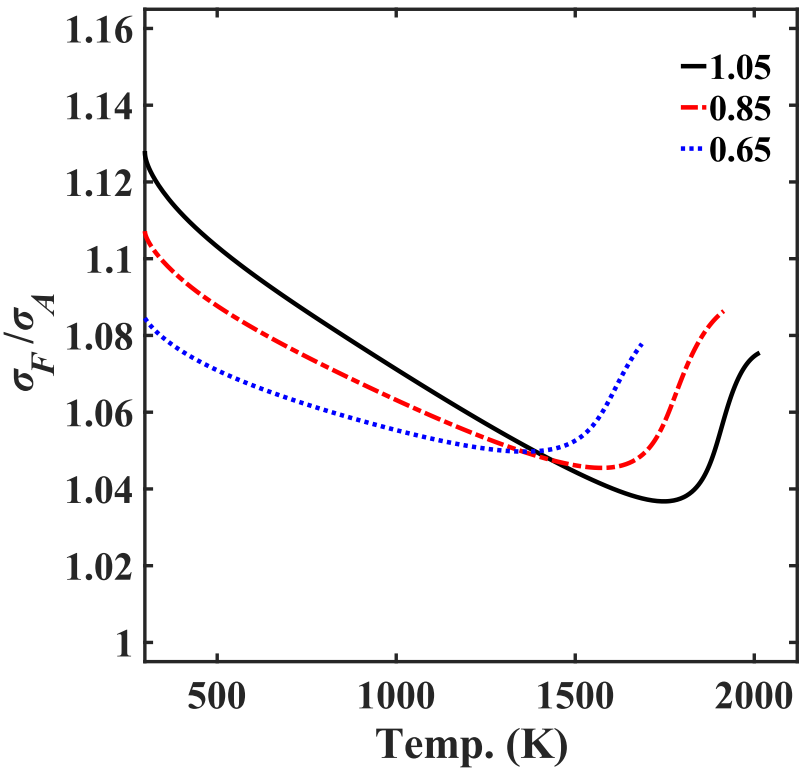

Figure 3.11: Ratio of the mixture-average Rayleigh cross-section as a function of temperature.

Based on Fig. 3.11 it is apparent that the ratio $\overline{\sigma_F}/\overline{\sigma_A}$ does not drastically change through the flames considered here (i.e. less than $\sim$8%). However, this variation was still accounted for by solving Eq. 3.7 in an iterative fashion. Specifically, the temperature images were determined via the following steps.

1. First, Eq. 3.7 was solved with the value of $\overline{\sigma_F}/\overline{\sigma_A}$ being based on the reactants of the flame in question (i.e. the left most points of the functions in Fig. 3.11).

2. The result of step 1 and the mapping function in Fig. 3.11 were then used to update the value of $\overline{\sigma_F}/\overline{\sigma_A}$.

3. The updated value of $\overline{\sigma_F}/\overline{\sigma_A}$ from step 2 was then utilized to adjust the temperature image obtained from step 1.

4. Finally, steps 2 and 3 were iterated until the percent difference between temperature images from successive iterations was less than a percent, which usually only took 3 to 4 iterations.

The only additional processing applied to the results of those steps was 3×3 median filtering, which helped reduce salt-and-pepper noise.

One assumption inherent to the iterative process outlined above, however, is that the mapping relation derived from laminar flame simulations holds true for the extremely turbulent flames considered in this dissertation. While the validity of this assumption is still an unanswered question facing the combustion science community, there is a growing body of evidence that suggests such an assumption does in fact capture the average structure (i.e. the distribution of chemical species within temperature space) of highly turbulent premixed flames [31, 147, 148]. Thus, iteratively solving Eq. 3.7 with the above mapping relation appears to be reasonable.

3.4.2 Resolution and uncertainty of Rayleigh scattering measurements

The in-plane resolution of the Rayleigh scattering measurements was determined in the same way as those corresponding to the high-resolution CH_2O- and OH-PLIF images. Namely, the scanning knife-edge technique outlined in in Refs. [138–140] was used to obtain the discrete SRF for the Rayleigh imaging system. An error function was fit to that SRF and subsequently differentiated to yield the LSF associated with that imaging system. This SRF, the function fit to it, and the resulting LSF are provided in Fig. 3.12.

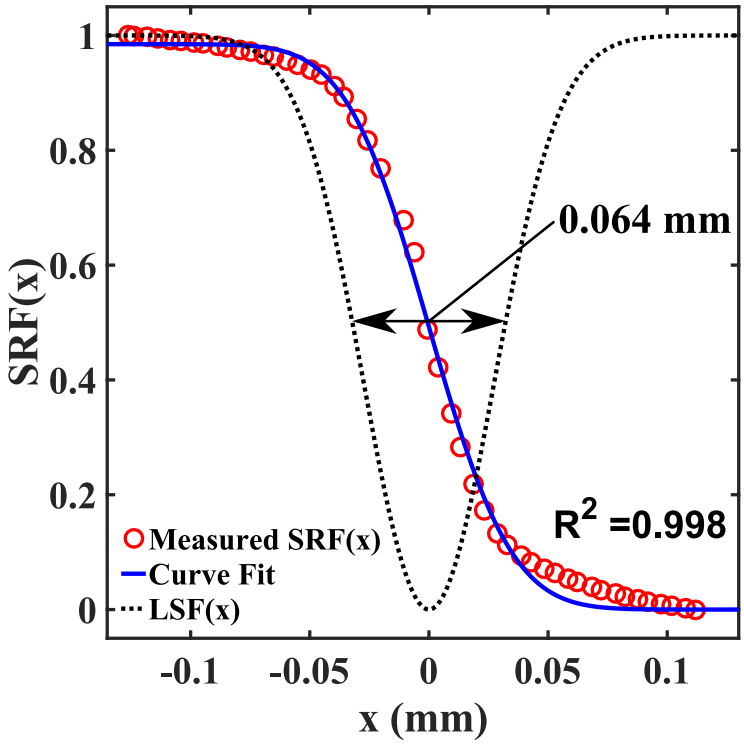

Figure 3.12: Measured SRF, the function fit to it, and the resulting LSF associated with the Rayleigh scattering imaging system.

As Fig. 3.12 indicates, the FWHM of the LSF associated with the Rayleigh scattering imaging system is 64 μm, which is taken to represent its in-plane resolution. The out-of-plane resolution for the Rayleigh scattering images (i.e. the laser sheet thickness) was determined to be 160 μm (FWHM) by scanning a knife-edge through the laser

sheet and monitoring the relative laser intensity with a photodiode. Thus, the out-of-plane resolution represents the limiting spatial resolution of this diagnostic.

The uncertainty in the Rayleigh scattering measurements was determined by comparing measured results from a laminar flame with $\phi = 0.85$ to those acquired from a CHEMKIN simulation with same ϕ (see Section 2.1 for simulation details). In order to make these comparisons at more than one location with respect to the flame front, the progress variable (c) was used as mapping relation between the measured and simulated data. Here, c is defined as:

$$c = \frac{T - T_0}{T_p - T_0}, \tag{3.12}$$

where T_0 and T_p represent the reactant and product temperatures, respectively. To determine the percent differences between the measured and simulated results three profiles, which are shown in Fig. 3.13, were obtained from the laminar temperature field images.

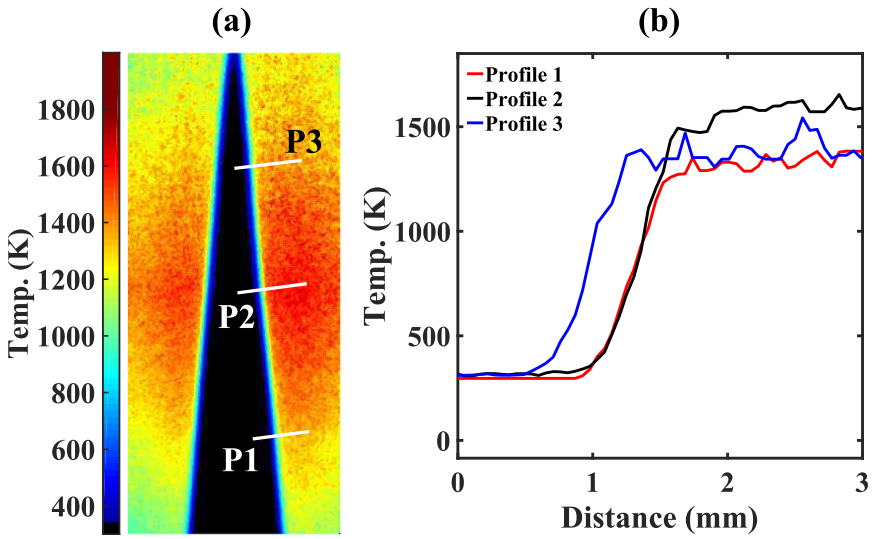

Figure 3.13: (a) Sample temperature image from a laminar flame with $\phi = 0.85$. The white lines in (a) represent the paths from which the profiles in (b) were derived from. Note that "P1" stands for "Profile 1," etc.

Once those profiles were obtained, a progress variable based on Eq. 3.12 was determined for each of them as well as the simulated results. A plot of temperature as a function of c for each of those profiles and the simulated results are provided in Fig. 3.14.

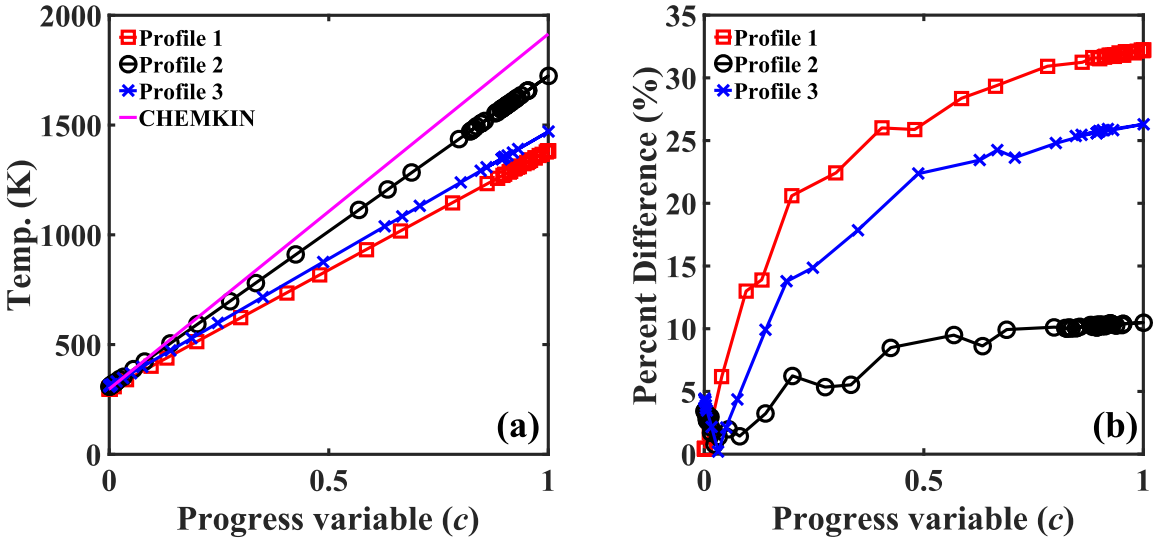

Figure 3.14: (a) Temperature from the three profiles in Fig. 3.13 as well as the CHEMKIN simulation plotted as a function of c. (b) The percent differences between the measured profiles and the simulated profile in (a) as a function of c.

Based on Fig. 3.14a, it is apparent that the variation between the measured and simulated data increases as one traverses the flame front (i.e. from the reactants to the products). Specifically, the percent differences between the measured and simulated results, which are plotted as a function of c in Fig. 3.14b, increase from $\sim$5% in the reactants to $\sim$32% in the products. A portion of this error stems from the fact that, rather than actually being measured, many of the rate coefficients within the chemical mechanism utilized in the CHEMKIN simulation were merely "tuned" to give accurate ignition delay times and S_L values. Yet, most of this error is likely a result of the non-ideal background subtractions, which were implemented in the fashion described by Eq. 3.7. For instance, though we attempted to account for the background scattering with $\overline{I_S}$, determining that image required a slightly different burner configuration

than was used to generate the laminar and turbulent flames. Thus, the background scattering many not have been exactly the same between the separate setups, which likely contributed to the relative errors presented in Fig. 3.14b. Furthermore, it is clear from Fig. 3.14b that the relative error between the measured and simulated results is not the same for each profile (i.e. location in the laminar flame). A likely and partial explanation for this is the fact that the simulation represented a very idealized situation in which a 1-D flame was freely propagating though a premixed fluid void of any boundary disturbances. This, of course, is not the case for the laminar flame the measurements were made in, which was likely subjected to slight degrees of stretch and was potentially affected by its surrounding environment. However, it is quite possible that the non-ideal background subtractions also contributed to the variations in the percent difference values determined for the separate profiles.

Though the relative error plotted in Fig. 3.14b was derived from a single image (i.e. Fig. 3.13a), all of the images acquired in that data set are very similar. Namely, the average standard deviation taken over that whole data set at a given pixel within the reactants and products is $\sim$10 K and $\sim$50 K, respectively (i.e. the precision was $\sim$3%). Thus, the relative error in Fig. 3.14b serves to represent that of the Rayleigh scattering measurements in general. While the relative error between the simulated and measured results is quite high in the product field, that within the preheat zone region, which is the primary region of interest concerning the Rayleigh measurements in this dissertation, is a bit more reasonable. In general, the preheat zone is marked by $0.2 < c < 0.4$ [2, 4, 5, 7]. Thus, the relative uncertainty of the Rayleigh scattering measurements made here is taken to be $\sim$23%, which is the worst case error at $c \approx 0.3$ in Fig. 3.14b.

3.5 Verification of preheat zone imaging

The notion that CH_2O-LIF signals serve as a marker of the preheat zone in turbulent premixed methane–air flames has been invoked in many experimental studies [17–19, 22, 111, 124, 149, 150]. Yet, to the best of the author's knowledge, support for this notion has primarily been derived from chemical kinetic mechanisms (e.g. GRI-Mech 3.0 [34]), qualitative observations from experiments [17–19, 21], and results from numerical flamelet simulations [21]. Therefore, to provide more substantial support for the notion that CH_2O-LIF signals mark the preheat region within turbulent premixed methane–air flames, particularly those subjected to extreme levels of turbulence, both qualitative and quantitative comparisons are made between simultaneously acquired preheat and Rayleigh scattering images.

Such comparisons were made in three separate cases, which included a laminar flame with $\phi = 0.85$ and two turbulent cases: Case 1A-0.85 and Case 6A-0.85. Note that only images from Z1PH (see Fig. 2.2) were considered when making these comparisons in the turbulent cases. Sample images from the laminar flame and those cases are presented in Figs. 3.15 – 3.17, respectively.

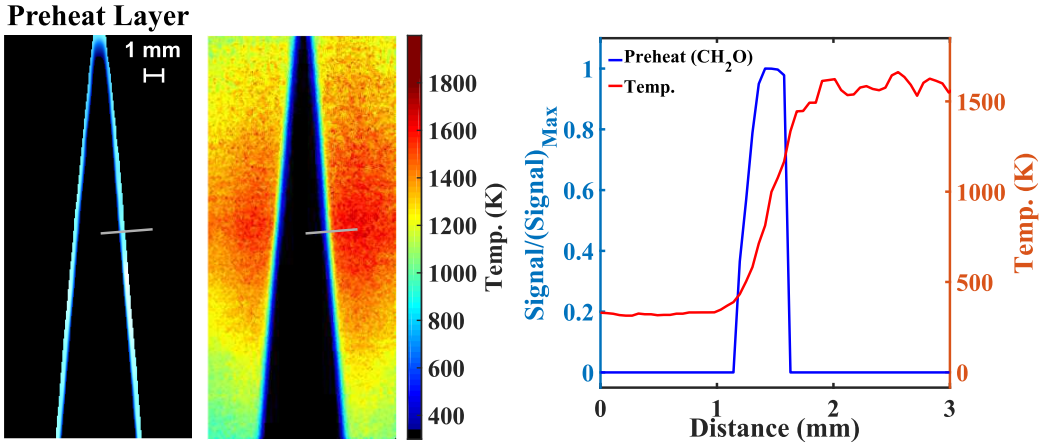

Figure 3.15: Sample preheat and temperature images from a laminar flame with $\phi = 0.85$. The black and blue colors in the temperature field image represent regions that are below and above 340 K, respectively. The gray line in the preheat and temperature images indicate the paths along which the plot to the right was derived from.

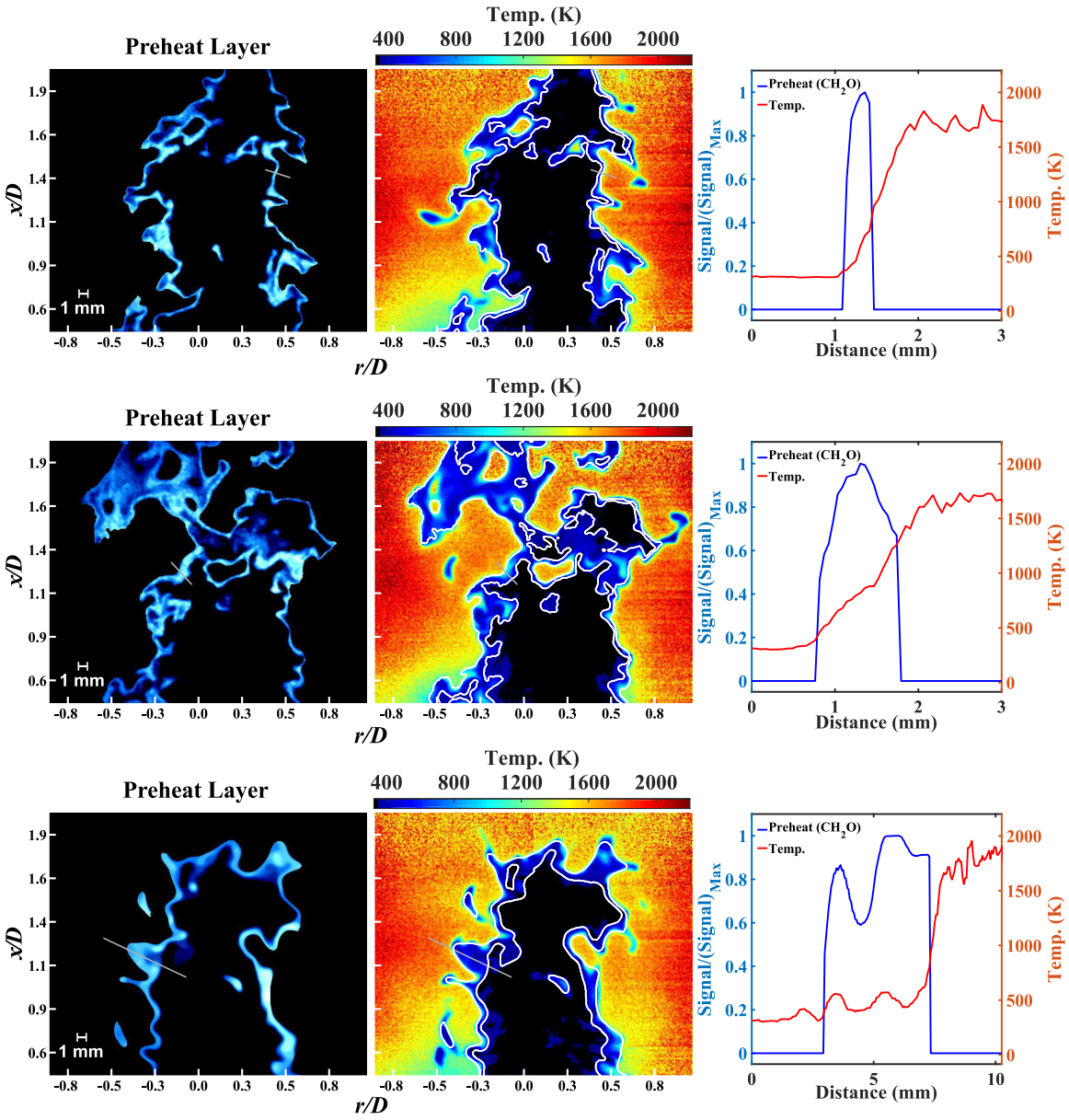

Figure 3.16: Sample preheat and temperature images from Z1PH of Case 1A-0.85. The white lines superimposed on the temperature images indicate the boundaries of the preheat layers. The black and blue colors in the temperature field images represent regions that are below and above 330 K, respectively. The gray lines in the preheat and temperature images indicate the paths along which the plots to the right were derived from.

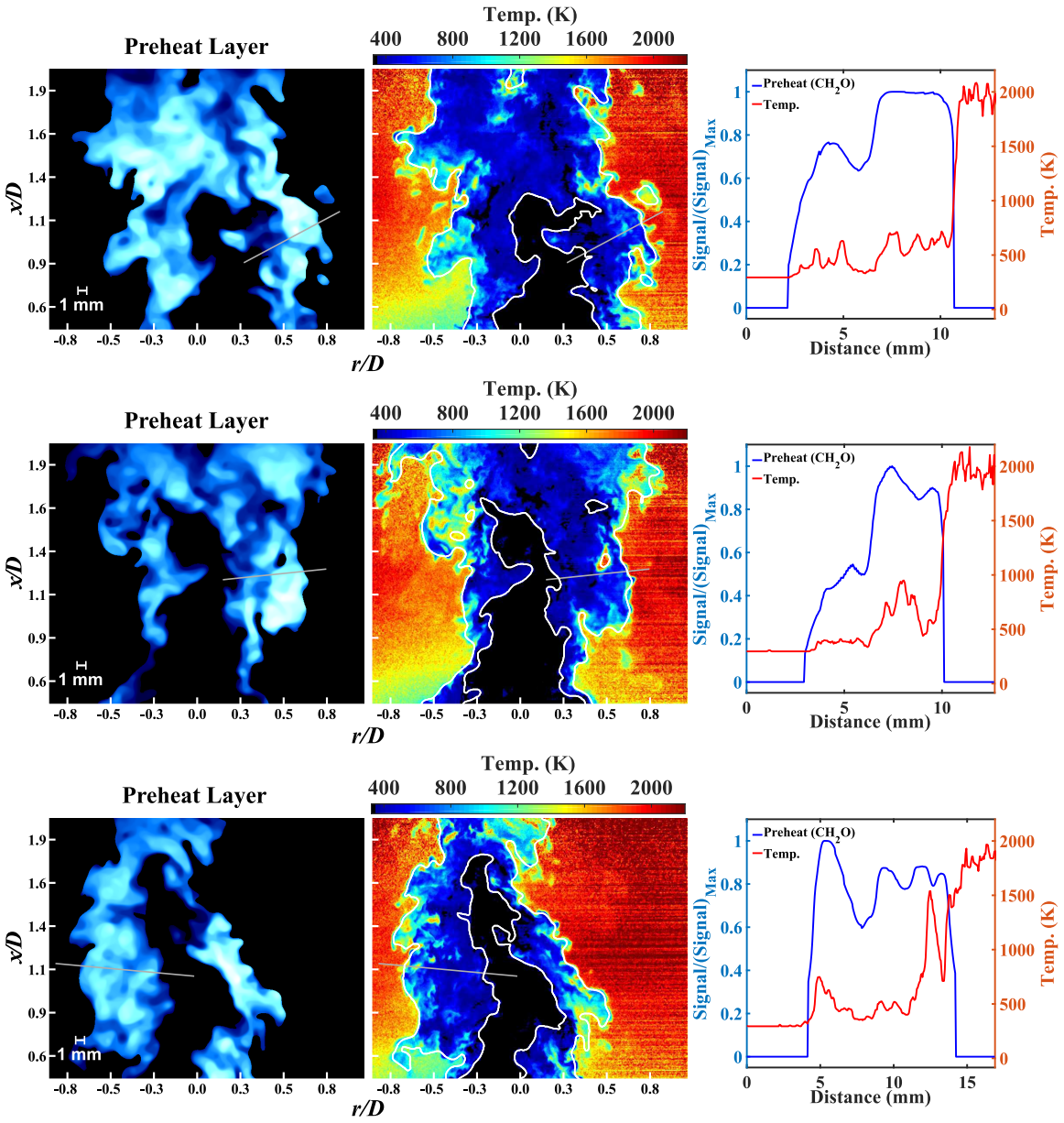

Figure 3.17: Sample preheat and temperature images from Z1PH of Case 6A-0.85. The white lines superimposed on the temperature images indicate the boundaries of the preheat layers. The black and blue colors in the temperature field images represent regions that are below and above 330 K, respectively. The gray lines in the preheat and temperature images indicate the paths along which the plots to the right were derived from.

The straight gray lines in Figs. 3.15 – 3.17 identify the paths from which the information in the plots on the right hand side of each figure was derived. Furthermore, the white lines superimposed on the temperature images in the figures from the turbulent

flames mark the boundaries of the corresponding preheat layers. Based on the plot in Fig. 3.15, it is apparent that the preheat layer derived from the CH_2O-LIF signal (i.e. see Sections 2.2.2.3 and 3.1.2 for details) marks an elevated temperature region within that laminar flame. Specifically, the edges of the preheat layer taken from the specific path in Fig. 3.15 correspond to temperatures of ∼450 K and ∼1200 K. Likewise, the plots in Figs. 3.16 and 3.17 indicate that the preheat layers along the specific trajectories for those turbulent flames span a range of temperatures bounded by ∼350 K and ∼1100 K. Beyond those specific trajectories, it is rather apparent from the white lines in the temperature images of Figs. 3.16 and 3.17, which clearly isolate blue and teal regions (i.e. regions in which the temperature falls between 330 K and ∼1100 K), that the preheat layers based on the CH_2O-LIF signal track elevated temperature regions throughout the entire flame. Thus, from a qualitative stand point, Figs. 3.15 – 3.17 imply that the definition invoked here for identifying preheat layers is robust.

However, to provide quantitative experimental support for this notion, the probability distributions of temperatures along the preheat layer boundaries were determined from a total of 100 images taken from the three specific cases considered here. These distributions are plotted in Fig. 3.18.

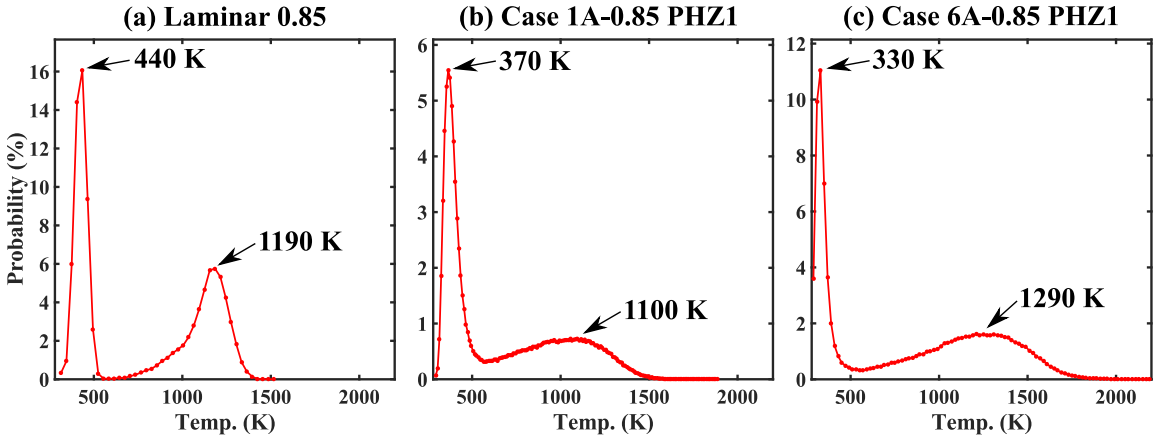

Figure 3.18: PDFs of the temperature along the edges of the preheat layers within: (a) a laminar flame with $\phi = 0.85$; (b) Case 1A-0.85; and (c) Case 6aA-0.85.

All three subplots in Fig. 3.18 exhibit two distinct peaks, one at lower (∼370 K) and another at higher temperatures (∼1100 to ∼1300 K). Clearly, the former correspond to the upstream edges of the preheat layers, while the latter represent their downstream edges. It is interesting that in all three cases considered here, even the laminar case, the distributions of temperature at the downstream edges are much broader than those at the upstream edges. Furthermore, based on Fig. 3.18 it appears that turbulence has a greater effect on the temperature distributions at the downstream edges than at the upstream edges, since the downstream distributions are significantly broader in the turbulent cases.

In order to characterize the range of temperatures over which the preheat layers were most likely to exist, the most probable temperature values of the two peaks were identified and are labeled in Fig. 3.18. Based on these temperatures, it is apparent that the preheat layers (as defined here) typically reside within a range of temperatures that spans from ∼350 K to ∼1200 K. Quite strikingly, this range is even consistent between the laminar flame and one of the most turbulent cases considered in this dissertation (i.e. Case 6A-0.85). While the upstream edges of these preheat layers reside in a lower temperature region than is expected from a laminar flame simulation (e.g. Fig. 2.8), it is apparent that they do lie within regions where the local temperature is elevated above that of the incoming reactants. Additionally, since the probability of finding downstream preheat layer edges above ∼1400 K is quite low, the majority of them are situated below the theoretical crossover temperature (i.e. the temperature that separates reactants and products) associated with premixed methane–air flames (i.e. 1500 K [1]). Therefore, it is apparent that preheat layers based on thresholded CH_2O-LIF signals bound regions of elevated temperature that do not incorporate those associated with the primary reaction zones. Furthermore, this fact is observed to be true for both laminar and extremely turbulent flames. Thus, the qualitative and quantitative results presented in this section demonstrate

that thresholded CH_2O-LIF signals serve as robust surrogates for marking the preheat layers of the flames considered in this dissertation.

3.6 Robustness of reaction layer imaging

In this section, results from a recent study (i.e. Ref. [132]), which focused on a subset of the data collected in this dissertation, are presented in order to demonstrate the robustness of the reaction layer visualization techniques implemented here. Specifically, overlap- and CH-layer data from Cases 2A-1.05, 3A-1.05, 4A-1.05, and 5A-1.05 (see Table 2.1 for details), are compared to show that both techniques provide consistent results, which, based on Fig. 2.8, is expected. The particular parameter that is compared is the flame surface density (FSD, Σ), which represents the average flame-surface area per unit volume. As was briefly mentioned in Section 1.4, the FSD is often used in numerical models of turbulent premixed combustion to close the average chemical source terms [76, 77, 79]. The reason for this is that the integral of Σ is related to the total surface area of a wrinkled flame front, and thus, under the flamelet assumption, it is also proportional to the turbulent burning velocity (S_T) [73, 91, 151, 152]. For this reason and because Σ is a statistical quantity [78, 79] (i.e. it is based on the *average* flame surface area within an appropriately sized volume), its distribution for a specific flame should be the same regardless of the diagnostic used to visualize the flame front. Thus, if the layers obtained from the CH- and overlap-layer imaging techniques implemented here are properly, or at least consistently, tracking flame fronts, the spatial distributions Σ derived from them, as well as the integrated values of those distributions, should be similar.

In general, the FSD is a 3-D quantity; however, since only 2-D reaction layer information was obtained from the CH- and overlap-layer techniques, here the FSD is represented by its in-plane component ($\Sigma_{x,r}$). In this dissertation, $\Sigma_{x,r}$ is defined as:

$$\Sigma_{x,r} = \frac{\Delta_L}{\Delta x^2}, \tag{3.13}$$

where Δ_L is the ensemble-averaged length of a flame front within an interrogation box of size Δx. Here, Δx was taken to be 16 pixels, which corresponds to 0.91 mm in the overlap-images and 1.5 mm in the CH-images. To compute Δ_L, the number of skeletal-points that lied within the interrogation box were identified and that value was subsequently divided by the width of the skeleton (i.e. 1 pixel). Computing Δ_L in this way eliminates bias caused by differences in the average reaction layer thicknesses and it also reflects the assumption made when FSD is used to model reaction rates (i.e. that the flame front is infinitely thin [73, 76, 77, 151, 152]).

To provide a fair comparison between FSDs determined from the overlap-layer and CH-PLIF images (Σ_{OL} and Σ_{CH}, respectively), the CH-PLIF dataset was reduced by only considering every 10th imagine (i.e. a total of 409 images were used to compute Σ_{CH} for each case listed above). Qualitative comparison between Σ_{OL} to Σ_{CH} are based on radial profiles acquired from two separate axial locations above the burner, namely, one with $x = 42$ mm and another with $x = 47$ mm. The reason for choosing these specific axial locations is because, as Fig. 2.2 depicts, Z1CH and Z2CH overlap within that region. Therefore, at those axial locations, an estimation of the uncertainty in determining Σ_{CH} from two independent samples can be acquired and used to gauge the severity of any variations between Σ_{CH} and Σ_{OL}. Profiles of Σ_{OL} to Σ_{CH} from the cases listed above are plotted in Fig. 3.19.

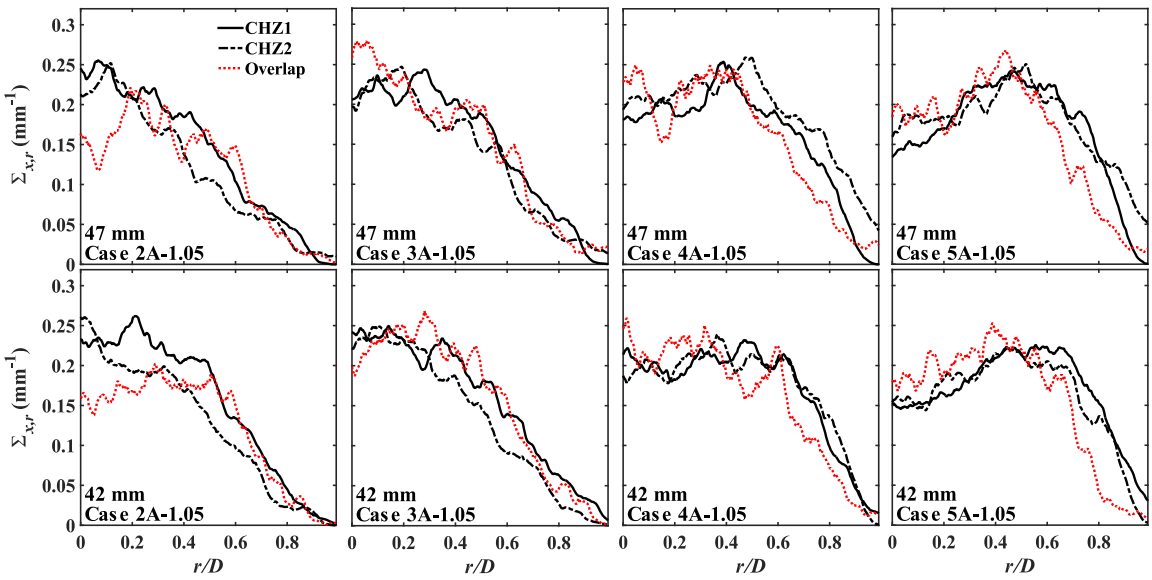

Figure 3.19: Profiles of FSD acquired from Cases 2A-1.05, 3A-1.05, 4A-1.05, and 5A-1.05 at two separate axial locations ($x = 42$ mm and $x = 47$ mm). The dotted red lines indicated results derived from overlap-layers, while the solid and dashed black lines represent profiles determined from CH-PLIF measurements made in CHZ1 and CHZ2, respectively. Note that $D = 21.6$ mm, is the inner diameter of the nozzle at the Burner's exit.

Based on Fig. 3.19, it is apparent that the radial profiles of Σ_{OL} (dotted red line) closely follow those of Σ_{CH} from CHZ1 and CHZ2 (solid and dashed black lines, respectively) for each case and axial location considered. The consistency between profiles of Σ_{OL} and Σ_{CH} in Fig. 3.19, suggest, that both of these diagnostics provided qualitatively similar results. Yet, a more rigorous assessment can be made by considering values obtained by integrating those profiles over the radial direction. Specifically, consider the value Ω, which is defined as:

$$\Omega = \int_0^\infty \Sigma_{x,r}(x)dr, \tag{3.14}$$

where x and r represent the axial and radial locations, respectively. According to Refs. [128, 151] Ω is related to the degree of wrinkling associated with a flame front,

and based on the discussion above, it also represents a portion of the average area of a turbulent flame front [91]. The values of Ω determined for the profiles of Σ_{OL} and Σ_{CH} from CHZ1 and CHZ2 in Fig. 3.19 (Ω_{OL}, Ω_{CHZ1}, and Ω_{CHZ2}, respectively) are provided in Table 3.3.

Case	x (mm)	Ω_{OL}	Ω_{CHZ1}	Ω_{CHZ2}
2A-1.05	42	2.49	2.93	2.48
	47	2.64	3.24	2.65
3A-1.05	42	3.14	3.14	2.87
	47	3.32	3.32	2.85
4A-1.05	42	3.34	3.43	4.01
	47	3.39	3.61	3.64
5A-1.05	42	3.40	3.60	3.76
	47	3.35	3.61	3.34

Table 3.3: Ω values obtained by applying Eq. 3.14 to the profiles in Fig. 3.19.

Upon inspection of the values in Table 3.3, one finds that the percent differences between Ω_{OL} and Ω_{CHZ1} range from 0.1% to 20.7%, while those between Ω_{OL} and Ω_{CHZ2} span from 0.4% to 18.2%. In comparison, those percent differences are no greater than the ones between Ω_{CHZ1} and Ω_{CHZ2}, which range from 0.1% to 20.2%. Thus, the Ω_{OL} values clearly agree well with both the Ω_{CHZ1} and Ω_{CHZ2} values derived from the two axial locations and four cases considered here. Given the qualitative and quantitative agreement between FSD-profiles in Fig. 3.19 and the computed values of Ω in Table 3.3, respectively, it is apparent that the CH-PLIF and overlap-layer imaging techniques implemented here provide consistent results. This fact, in conjunction with the qualitative and quantitative structural results presented in the next Chapter, lends support to the notion that the CH-PLIF and overlap-layer imaging techniques employed in this dissertation are robust tools for visualizing reaction layers in extremely turbulent premixed methane–air flames.

CHAPTER IV

Preheat and Reaction Layer Structure

This Chapter presents both qualitative and quantitative results from applying the diagnostic techniques described in Chapters II and III to the cases listed in Table 2.1. First, sample images of preheat and reaction layers are provided and their general qualities are examined. Then quantitative thickness values are presented and discussed. Following that discussion, a time sequence of CH-OH images is presented to show the development of locally extinguished reaction layers.

4.1 Preheat zone structure

Sample preheat layers from eight different cases are presented in Fig. 4.1.

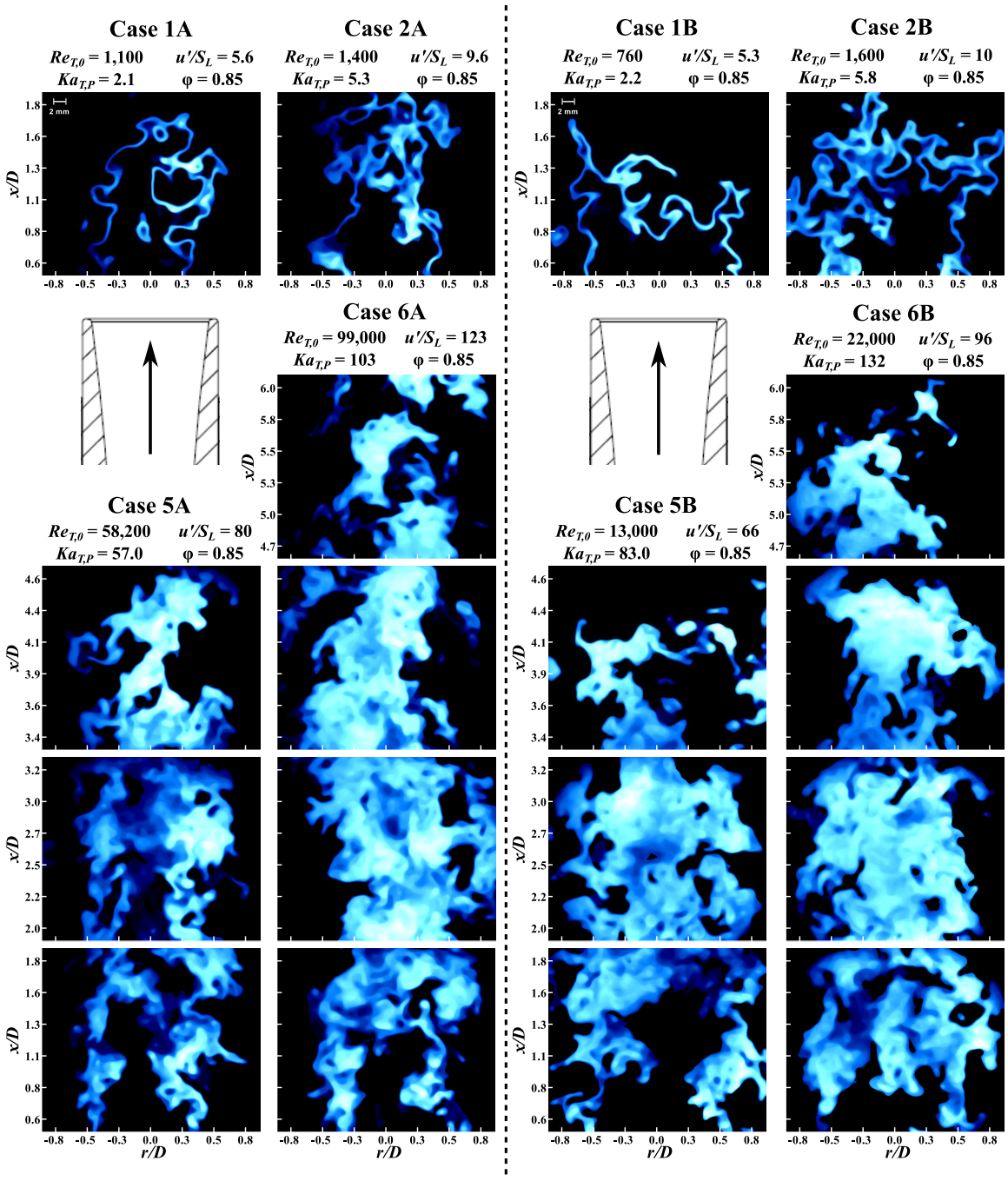

Figure 4.1: Sample preheat zone images (i.e. CH_2O-PLIF images). Case details are provided above each set of panels. Note that $D = 21.6$ mm, is the inner diameter of the nozzle at the Burner's exit.

It is evident from Fig. 4.1 that as the turbulence intensity increases, the preheat layers become extremely broad. In fact, in our most turbulent cases (cases 5 and 6) the preheat layers are so broad that they fill the entire central core of the flame brush,

particularly in the downstream regions of those flames. In addition to increasing with turbulence intensity, the sample images provided in Fig. 4.1 also show that the preheat zone thicknesses increase with axial distance from the burner. This broadening of preheat layers with increasing turbulence intensity and height above the burner is consistent with results from prior experimental [13, 14, 17–21] and numerical [24, 26–32, 94] studies. For example, Zhou et al. [17–19] observed broadened CH_2O-layers in all of their conditions and also noticed thicker CH_2O-layers at locations further from the exit of their burner. Similar observations were also pointed out in a recent study that focused on a subset of the data considered here [22]. This broadening of preheat layers with increasing axial distance suggests that upstream history effects [18] and a characteristic residence time (x/U_0) [22] may play a role in determining the structure of flames.

The fact that the highest turbulence intensity cases in Fig. 4.1 exhibit very broad preheat layers is consistent with the theoretical Borghi Diagram, since each of those cases are classified into either the theoretical BP-TR or the Broadened Reactions regimes (i.e. they have $Ka_{T,P} > 1$). Yet, the least turbulent cases in Fig. 4.1 (i.e. Case1A-0.85 and Case1B-0.85) appear to be in contradiction with the Borghi Diagram. Specifically, though both of those cases are classified into the theoretical BP-TR regime, their preheat layers appear to be rather thin. Such an observation is corroborated by the quantitative results presented in Section 4.3.

4.2 Reaction zone structure

Unlike the preheat layers of the flames studied here, their reaction layers, represented by CH- and overlap-layers, remained thin even though the turbulence intensity increased by nearly a factor of 60. Typical overlap-layers from "A" and "B" cases are presented in Figs. 4.2 and 4.3, respectively, while sample CH-layers from "A" cases are displayed in Figs. 4.4 and 4.5.

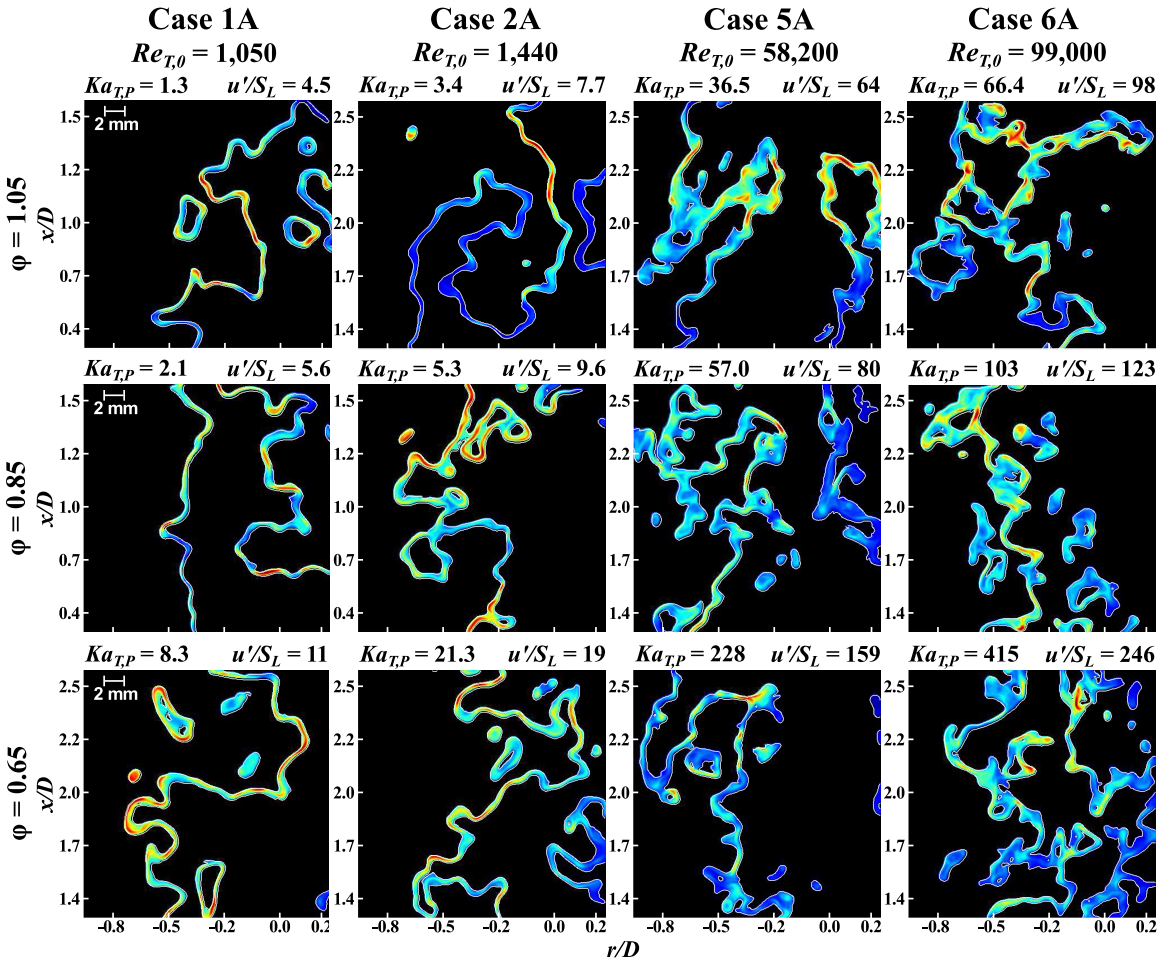

Figure 4.2: Sample reaction layers derived from the overlap method. Case details are provided above each panel.

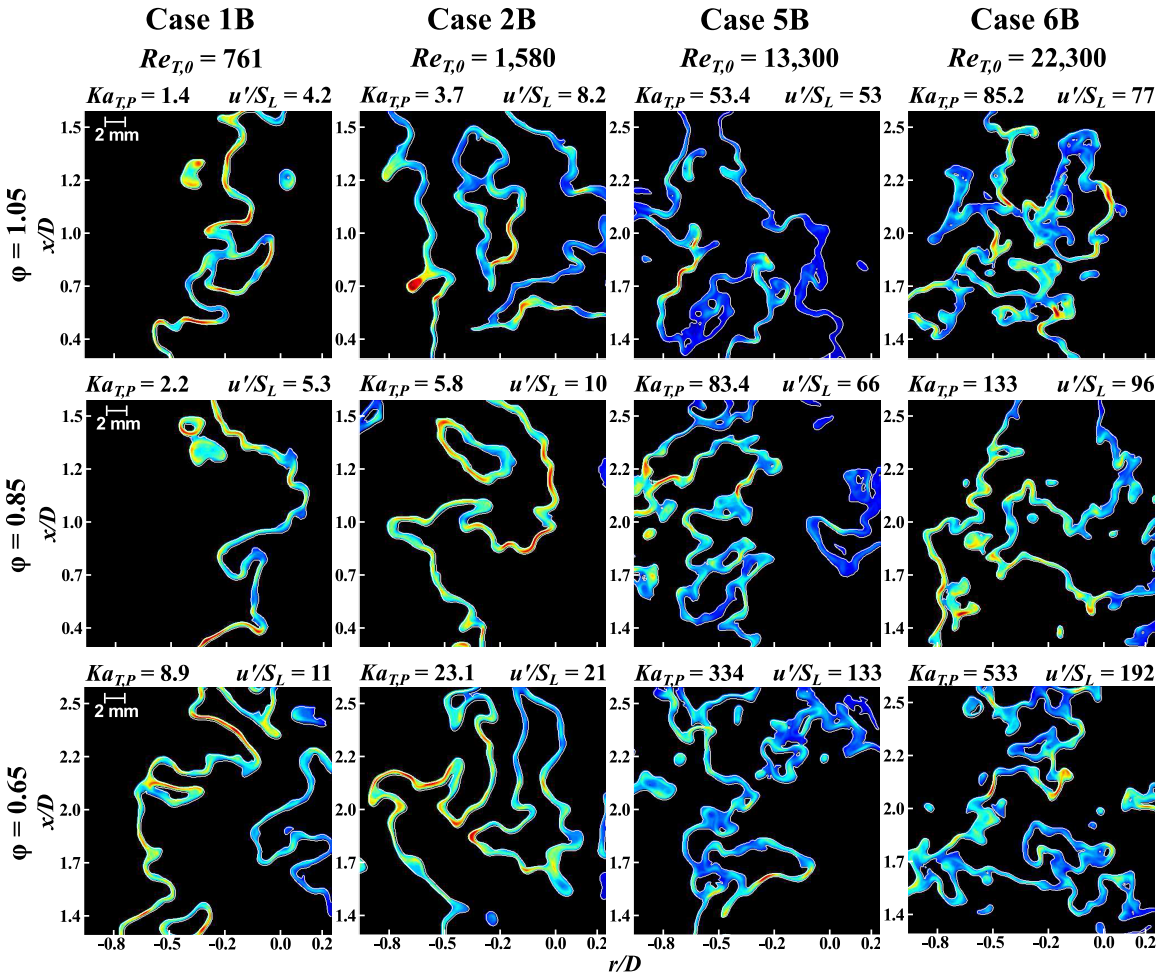

Figure 4.3: Additional reaction layers derived from the overlap method. Case details are provided above each panel.

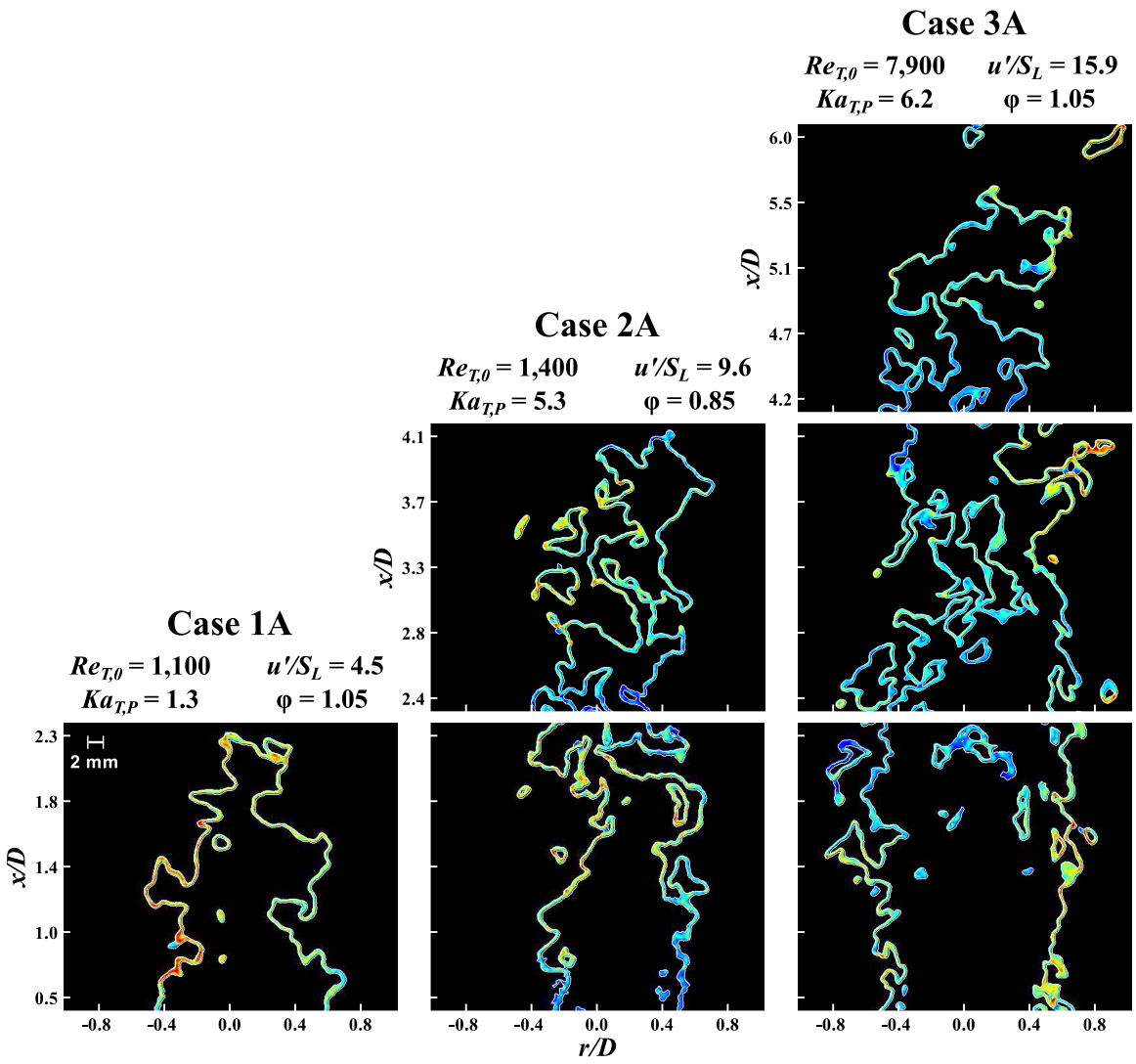

Figure 4.4: Sample reaction layers, based on the CH-PLIF technique, for Cases 1A to 3A. Case details are provided at the top of each column.

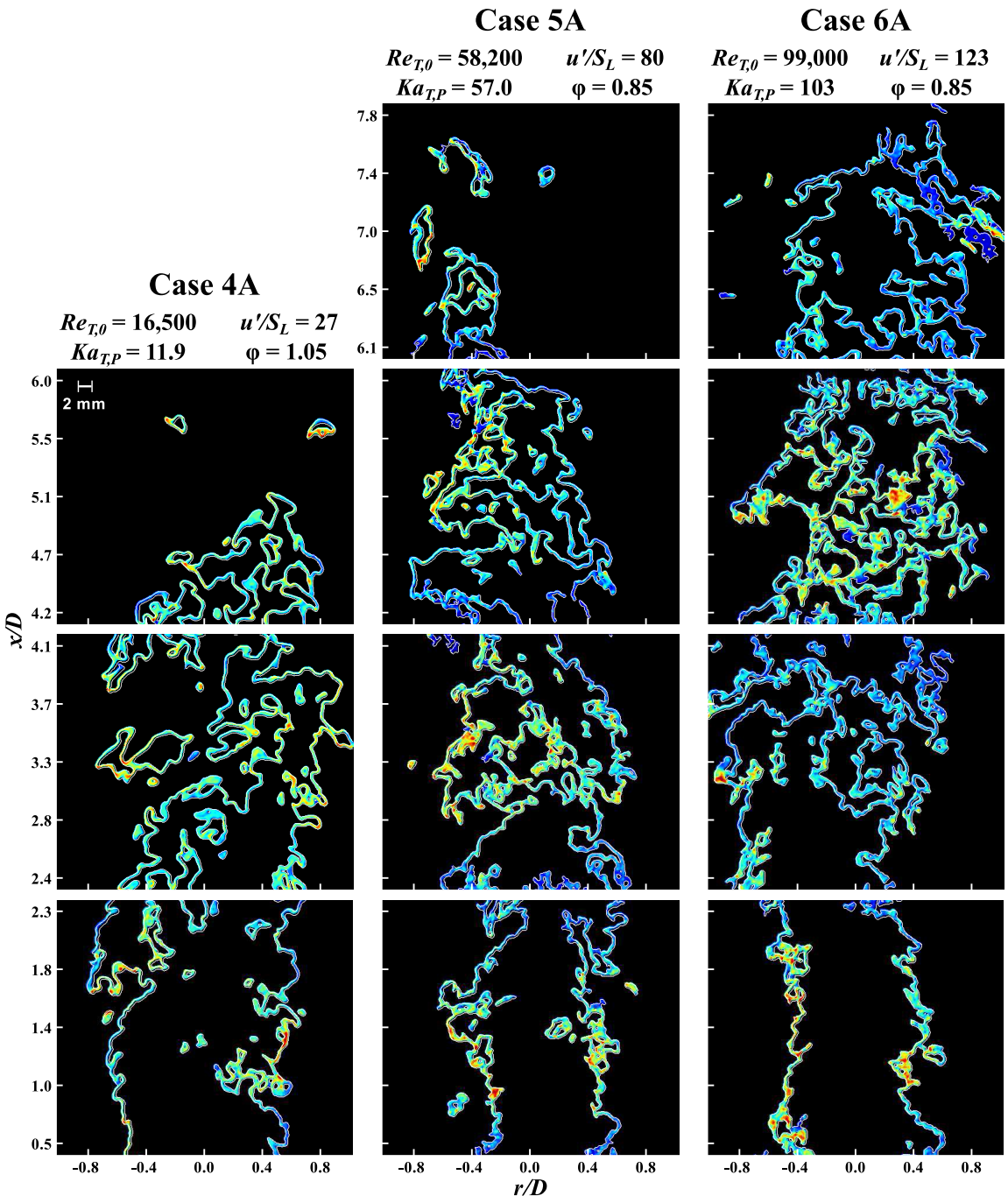

Figure 4.5: Sample reaction layers, based on the CH-PLIF technique, for Cases 4A to 6A. Case details are provided at the top of each column.

As can be seen from Figs. 4.2–4.5, one of the primary attributes of the flames studied in this dissertation is that their reaction layers were relatively thin (i.e. less than twice that of their laminar counterparts). Yet, locally broadened reaction layers (i.e.

those that are more than twice as thick as their laminar counterpart) can be seen in select regions of Figs. 4.2–4.5. And though a comparison of Figs. 4.2 and 4.3 to Figs. 4.4 and 4.5 suggests that the overlap-layers tend to exhibit more local broadening, as is presented in Section 4.3, the average overlap- and CH-layer thicknesses, normalized by their respective measured laminar values, are very similar.

Figures 4.2–4.5 also demonstrate that as the turbulence level increases, the reaction layers become more and more contorted and corrugated. This is particularly evident in the series of CH-PLIF images shown in Figs. 4.4 and 4.5. Specifically, while the lower level turbulence cases in Fig. 4.4 are wrinkled and slightly corrugated, the reaction layers of Case5A-0.85 and Case6A-0.85 in Fig. 4.5 are so convoluted and densely packed that it is nearly impossible to distinguish reactants from products in certain locations. Overlap-layers from cases 5 and 6 are also highly wrinkled and twisted, though notice that those from cases 5A and 6A (see the two right most columns of Fig. 4.2) are very similar in appearance to those from cases 5B and 6B (see the two right most columns of Fig. 4.3). In fact, upon comparing Fig. 4.2 to Fig. 4.3, it is apparent that overlap-layers from "A" cases (relatively large L_x values) are qualitatively the same as those from "B" cases (relatively small L_x values). Furthermore, though they are not shown (for brevity), CH-layers from "B" cases appear no different than those from the "A" cases in Figs. 4.4 and 4.5. This is interesting because "A" cases possess values of L_x that are up to four times as larger as those in the "B" cases (see Table 2.1). Thus, it appears that varying L_x over the range of values considered here has little qualitative effect on the reaction layer structure.

The fact that the reaction layers displayed in Figs. 4.2–4.5 are all relatively thin is partially consistent with their locations on the theoretical Borghi Diagram, since the majority of them possess $Ka_{T,P}$ values that are greater than 1 but are less than 100. However, the 6 cases in Figs. 4.2–4.5 with $Ka_{T,P}$ values in the range of 103 to 533 are clearly in contradiction with the predictions made for their reaction layers by the

Borghi Diagram. That is, though they are classified into the Broadened Reactions regime, their reaction layers do not appear to be broad, and at the very least are no thicker than those in cases subjected to modest turbulence levels. Experiments by Dunn et al. [11–13] and simulations by Aspden et al. [26] and Lapointe et al. [32] also found reaction layers in conditions where $Ka_{T,P} > 100$ to be relatively thin and continuous. Hence, the line defined by $Ka_{T,P} = 100$ does not appear to be the correct boundary between the BP-TR and Broadened Reactions regimes, although it should be mentioned that recent experimental studies by Zhou et al. [17–19, 126] indicated that broadened reactions can exist when $Ka_{T,P} \approx 100$. Further discussions regarding the location of boundary to the Broadened Reactions regime are provided in Section 5.2.

Though results from our study and those from these other studies with high $Ka_{T,P}$ values [11–13, 17–19, 26, 27, 32, 126] are somewhat conflicting in terms of when broadened reactions will exists, one consistency amongst them is that their reaction layers remained continuous so long as they were properly shielded by hot products. For example, notice that none of the reaction layers in Figs. 4.2–4.5 display a significant degree of localized extinction. Likewise, the reaction layers in studies by Dunn et al. [13] and Zhou et al. [17–19] remained continuous regardless of the fact that their cases possessed $Ka_{T,P}$ values that greatly exceeded 100. Thus, Peters' hypothesis that reaction layers will locally extinguish once $Ka_{T,P} > 100$ [1] appears to be incorrect, at least for burner geometries that incorporate significantly large pilots/co-flows to properly shroud the flame in hot products. However, as was shown by others [18, 21, 126] and as will be demonstrated in Section 4.4, in the absence of such shielding, room air entertainment can lead to localized extinctions.

4.3 Average preheat and reaction layer thicknesses

While the reaction layer images presented in Section 4.2 indicate that there are inconsistencies between observations and what is predicted by the Borghi Diagram, such evidence is by nature anecdotal. Proof that preheat and/or reaction layers broaden or remain thin requires rigorous statistical evidence. Such evidence is provided in Fig. 4.6a, which plots preheat and reaction layer thicknesses normalized by their respective measured laminar values (see Table 2.2) as a function of u'/S_L.

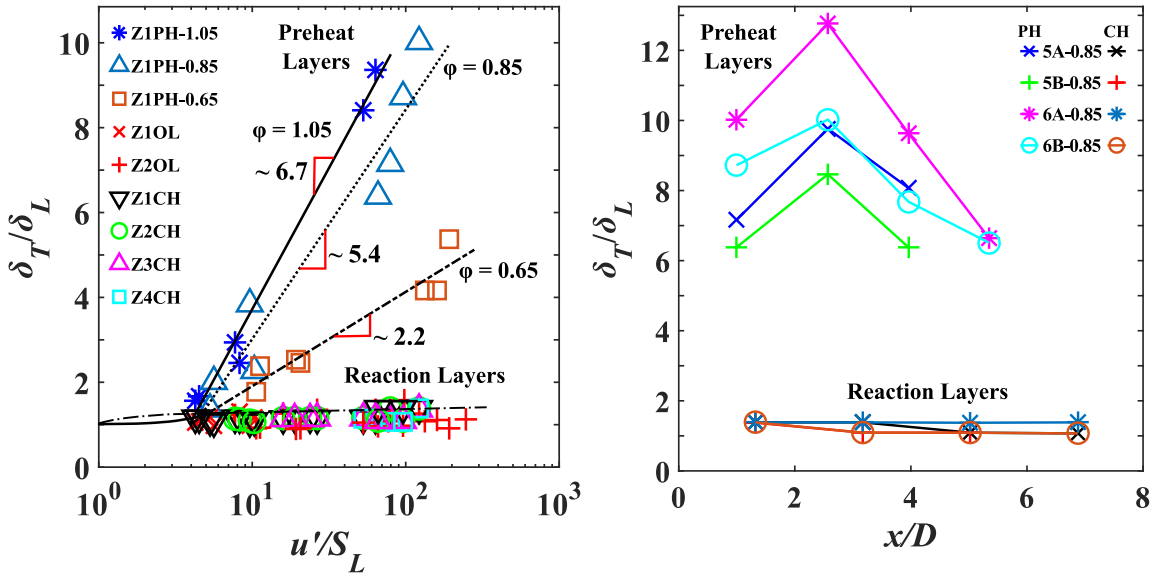

Figure 4.6: Average preheat and reaction layer thicknesses normalized by their respective laminar values (δ_L) and plotted as function of u'/S_L in (a), and as a function of axial distance for select cases in (b). ZnPH, ZnOL, and ZnCH indicate that the data were collected from Zone n (n = 1, 2, 3, or 4) of the preheat, overlap, and CH interrogation regions, respectively, where a larger value of n implies a zone that is further downstream. Note that the axial locations in (b) were defined as the midpoint of the separate zones (see Fig. 2.2).

It is clear from Fig. 4.6a that the preheat layer thickness dramatically increases with turbulence intensity, which is consistent with the preheat layer images shown in Fig. 4.1. In fact, the data points suggest that preheat layer thicknesses increase exponentially with u'/S_L, since the plot is semilogarithmic. Yet, a detailed inspection

of Fig. 4.6a suggests that several of the cases considered here possess thin preheat layers. Specifically, four of the preheat layer data points in Fig. 4.6a lie below a value of 2, and thus the cases from which those points were derived are considered to have thin (i.e. not broadened) preheat layers. The fact that several of the cases are found to possess thin preheat layers is also consistent with observations drawn from Fig. 4.1. Namely, recall that the preheat layers of the least turbulent cases considered in Fig. 4.1 appeared to be rather thin, at least in comparisons to the other cases presented therein. And, as was alluded to in Section 4.1, the fact that these four cases with thin preheat layers possess $Ka_{T,P}$ values that are greater than unity, implies that their structures are inconsistent with the Klimov-Williams criterion.

Another interesting observation from Fig. 4.6a is that the preheat layer thicknesses of cases with larger equivalence ratios increase more rapidly than those with lower equivalence ratios. This can be explained by recognizing that in the most turbulent cases the preheat layers are so broad that they fill the entire core of the flame brush (see Fig. 4.1). This implies that beyond a particular value of u'/S_L the preheat layer thicknesses will plateau, which is precisely what is observed if the preheat layer thicknesses are not normalized. But since the measured laminar preheat layer thicknesses increase as the equivalence ratio decreases (see Table 2.2), normalization of the turbulent thicknesses yields lower values for lower equivalence ratio cases. Thus, the trend of decreasing normalized preheat zone thicknesses with decreasing equivalence ratio, which was also observed by Tamadonfar and Gülder [2], is primarily a result of geometric constraints placed on the flames studied here.

The preheat layer trends in Fig. 4.6b, are also a result of geometric constraints. Specifically, notice that initially the average preheat layer thicknesses increase with axial distance, which is consistent with the preheat layer structures observed in Fig. 4.1. However, because the flame brush narrows at its tip, and since the preheat layers fill the entire core of the flames studied here, their thicknesses decrease after a partic-

ular axial distance from the burner. Yet, in contrast to the preheat layer thicknesses, the average CH-layer (i.e. reaction layer) thicknesses do not vary significantly with axial distance from the burner. In addition to not increasing with axial distance, it is evident from Fig. 4.6a that the average reaction (both CH and overlap) layer thicknesses are insensitive to increasing levels of turbulence. Moreover, the reaction layer data points in Fig. 4.6a indicate that the reaction layers remained relatively thin on average. In fact, in none of the cases studied here, even those with u'/S_L and $Ka_{T,P}$ values that exceed 100, are the average reaction layer thicknesses greater than twice that of their laminar counterpart. Hence, none of the cases considered in this dissertation are considered to possess broadened reactions. Thus, this statistical evidence clearly indicates that there are contradictions between observed and predicted reaction layer thicknesses for the six cases in Fig. 4.6a that are classified into the theoretical Broadened Reactions regime. In fact, based on the results presented here, the BP-TR regime should be extended to $Ka_{T,P}$ values that are as large as 533.

Though broadened reactions were not observed in this study, both Dunn et al. [12] and Zhou et al. [17–19] observed broadened reaction layers under highly turbulent conditions. Furthermore, the width of their reaction layers substantially increased with both turbulence intensity and axial distance from their burners. While Dunn et al. [12] only observed broadened reactions in cases with u'/S_L and $Ka_{T,P}$ values that were much larger than those studied here, Zhou et al. [17–19] observed them when u'/S_L and $Ka_{T,P}$ were roughly the same as and even less than those considered here. For example, recently Zhou et al. [19] observed broadened overlap-layers under conditions in which u'/S_L and $Ka_{T,P}$ were less than those in at least two of the cases studied here.

One difference between the work presented here and that of Dunn et al. [12] and Zhou et al. [17–19], which may explain these differences in observed reaction layer structure, is the fact that they employed a much different burner configuration

(i.e. jet-burners) than was utilized here (Bunsen-type burner). Namely, while the turbulence that interacted with their flames was primarily generated by the intense shear layers that developed around the jets issuing from their burners, the majority of the turbulence that interacted with the flames studied here was produced relatively far upstream of the flame fronts. These different turbulence generating mechanisms may permit different turbulence–flame interactions, which in turn lead to different turbulent flame structures. If this is indeed the case, predicting the structure of turbulent premixed flames will likely require knowledge of the particular burner-geometry/turbulence-generation-mechanism being used. In fact, as will be shown in the next section, this is already the case for determining the likelihood of observing broken reactions.

One thing to note, however, is that in an attempt to emulate the results of Zhou et al. [17–19], we created a small diameter (inner nozzle diameter of ∼1.75 mm) jet-burner and applied the CH-PLIF technique outlined in Section 2.2.2.2 to the flames it produced. Since the results of that investigation are not pertinent to the story told by this dissertation, they are presented in Appendix D rather than here. Nevertheless, the results suggest, quite contrary to what is presented by Zhou et al. [17–19], that even the reaction layers of those flames remain thin.

4.4 Local extinctions

The CH and overlap images displayed in Figs. 4.2–4.5 suggest that local extinction is not a common phenomenon in the flames studied here. In fact, based on comparisons between the length of the overlap-layers and the "hot-edge" of the CH_2O-layers, no more than 2% of the overlap-layers in any case were identified as being broken. Obtaining such statistical information from the CH-layers alone is a challenging task, however rough estimates from observations suggest that they exhibit a similar degree of local quenching. The fact that our six cases with $Ka_{T,P} > 100$ do not exhibit a

substantial degree of localized extinction suggests that Peters' notion, that local extinction will dominate once $Ka_{T,P} > 100$, is incorrect. As was mentioned in Section 4.2, this is further corroborated by numerical and experimental results from others [11–13, 17–19, 26, 27, 32, 126], who found local extinctions to be rare even when $Ka_{T,P} > 100$.

A likely reason those flames, and ours, remained relatively continuous is that they were all immersed within a field of hot products, which for experimental studies is a result of the particular burner used. For example, our burner and those of Dunn et al. [11–13] and Zhou et al. [17–19, 126] possess pilot-flames/hot-co-flows that are relatively large in comparison to the diameter of their primary flows. These large pilot-flames shroud the primary flames in fields of hot combustion products, which help to mitigate the entrainment of room air to the reaction layers. As was shown by Li et al. [21], and pointed out by Zhou et al. [18, 19], such entrainment is the most likely reason for localized extinction in Bunsen and jet-type burners. While their evidence was inferred from single shot images taken after an extinction event had occurred, Fig. 4.7 demonstrates the evolution of such an event and provides more substantial evidence that local extinctions are the result of cool gas entrainment in these flames.

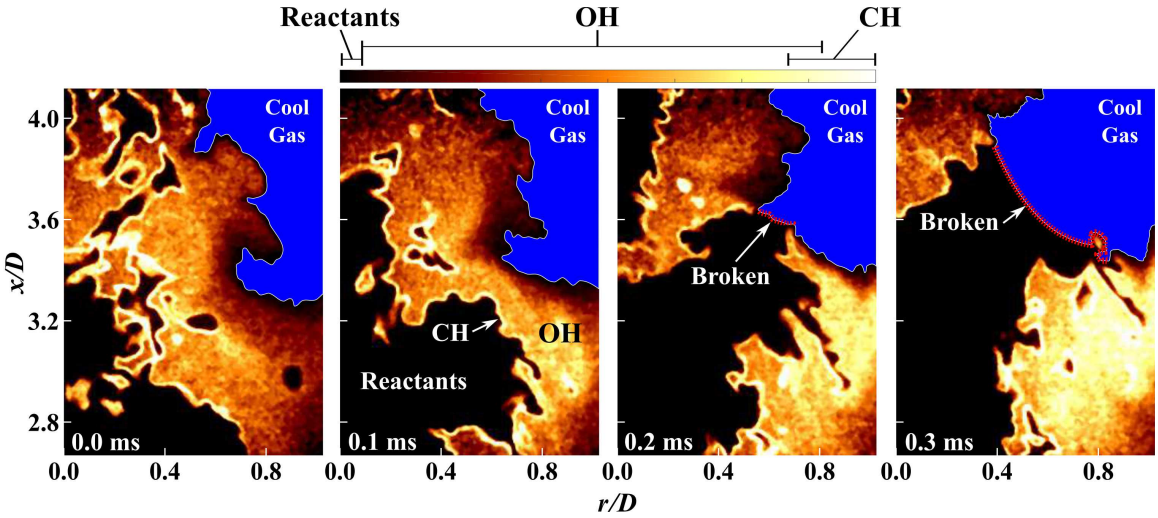

Figure 4.7: Time sequence of CH-OH images from Case5A-1.05 demonstrating how cool-gas entrainment can lead to local extinction. Note that the images have been cropped to focus in on the region of localized extinction.

Figure 4.7 presents a sequence of CH-OH PLIF images from Case5A-1.05, and like the sample CH-OH PLIF image shown in Fig. 2.6, higher intensity regions mark CH-layers, while regions with OH present are represented by low to high signal levels. The blue regions in Fig. 4.7 represent cool, entrained gas (most likely air), which were distinguished from the low-level signal regions (i.e. those where the signal was less than ~6% of an average value obtained from regions of OH) that corresponded to the reactants based on their location. The fact that the CH-OH PLIF images in Fig. 4.7 were only separated by 0.1 ms facilitated the tracking of interactions between the entrained cool gas and the CH-layers. Specifically, in the first two frames of Fig. 4.7 all of the CH-layers are continuous and are isolated from the cool gas by a region of hot products (i.e. OH). In the third frame, however, a portion of one of the CH-layers came in contact with the cool gas, and as can be seen, this resulted in a local break in the CH-layer (i.e. the reaction layer locally extinguished). Going from the third to the fourth frame, it is evident that that small break grew over time as a larger portion of the CH layer interacted with the cool gas. Yet, notice that even in the last two frames of Fig. 4.7 the CH-layers properly "back-supported" by hot products

remained continuous, only when the layers came in contact with the cool gas did their reactions cease. As mentioned above, such events were rare, but when they were observed it was generally evident that an interaction like the one in Fig. 4.7 had occurred. Thus, a lack of shielding from cool gas is the primary source of local extinctions in the flames studied here.

Other than in piloted Bunsen flames, local extinctions have also been observed in swirl stabilized [126], counterflow [117], and bluff body stabilized flames [23, 115]. While in some instances the local extinctions in those flames were the result of room air entrainment, particularly in swirl and bluff body stabilized flames [115, 126], local extinctions were also observed when the flames were properly back-supported. For instance, in the counterflow flames of Coriton et al. [117], local breaks in the reaction layers were observed even when their OH fields showed no evidence of cool gas entrainment. However, such counterflow flames are subjected to high strain rates over longer durations than in Bunsen-type flames. That is, high strain rates may need to be applied for sufficiently long periods before extinction can occur; thus, due to their particular configurations, counterflow flames may experience localized extinction more frequently than Bunsen flames, though further investigations are required to confirm this hypothesis. Nevertheless, it is apparent that burner geometry plays a significant role in determining the likelihood of localized extinction events, which means the location of the Broken Reaction Zones regime also depends on burner geometry and not just the turbulence characteristics of a particular flow-field. Therefore, incorporating the Broken Reaction Zones regime into the theoretical Borghi Diagram will likely require an additional axis that accounts for the degree of product-stratification (i.e. the amount and frequency of cool gas entrainment) and/or burner-geometry. However, the addition of such an axis is outside the scope of this dissertation, since it would require detailed results from a wide range of burner configurations. Furthermore, a universal diagram covering all burner geometries may

not exist, in which case a specific diagram for each burner type would be necessary.

CHAPTER V

Measured Regime Diagram

Based on the results presented in Sections 4.2 and 4.3, it is apparent that some of our findings are in contradiction with what is predicted by the theoretical Borghi Diagram. As was indicated in Chapter I, this is not the only experimental study to have observed inconsistencies between experimental results and the predictions made by the Borghi diagram. For example, Refs. [2–11, 22] each present at least one case that does not comply with the theoretical boundaries displayed in Fig. 1.2a. Additionally, many DNS studies (e.g. Refs. [24–32]) have also identified flaws in the theoretical Borghi Diagram. To illistrate this, consider Fig. 5.1, which is similar to Fig. 1.2b, only the points from the results presented here as well as from previous investigations have been modified in order to indicate the flame structure that was ascribed to them.

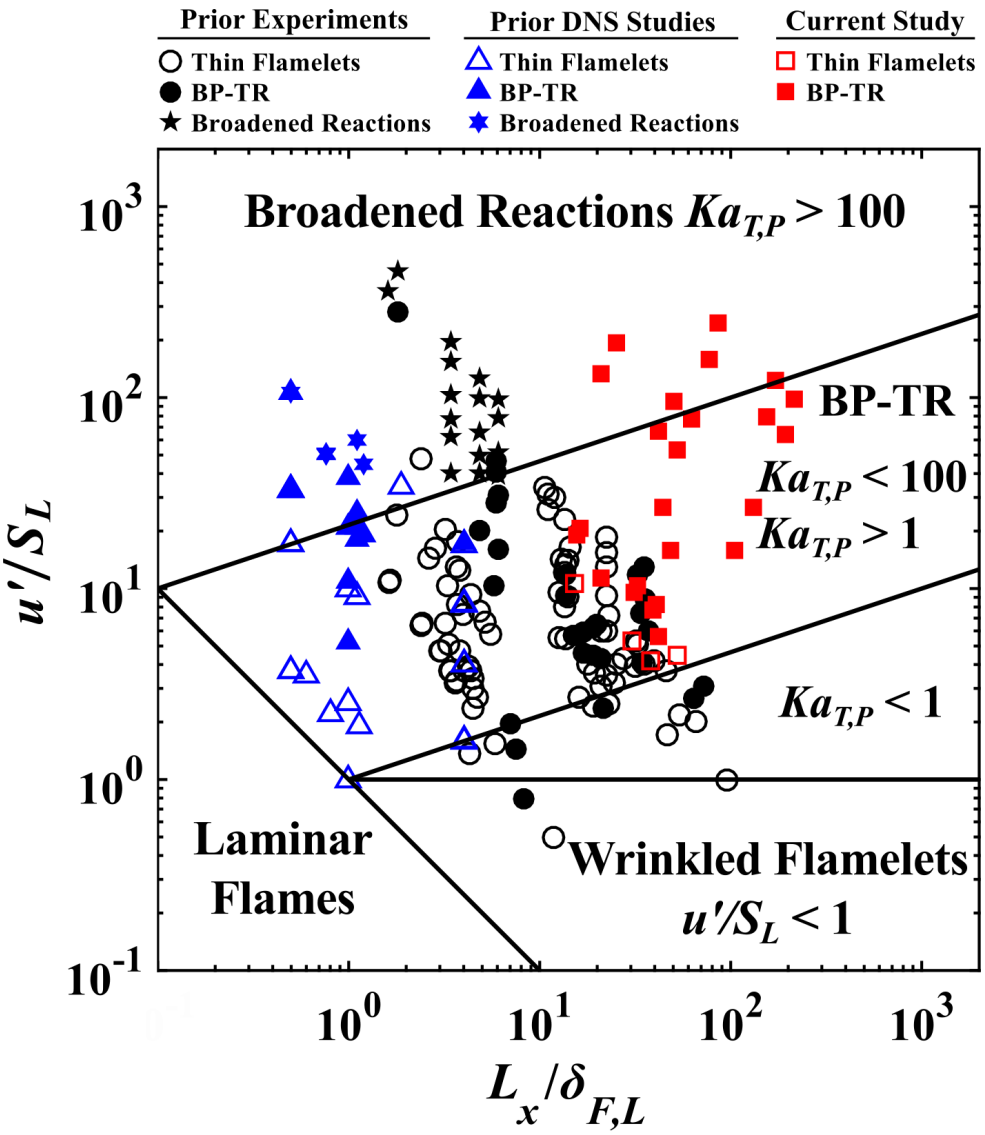

Figure 5.1: Theoretical Borghi Diagram adopted from Ref. [1] with prior and current cases included. Black circles represent prior experimental cases (See Refs. [2–23]), blue triangles mark prior DNS studies (see Refs. [24–32]), and the red squares indicate the experimental cases presented in this investigation. Open symbols indicate thin flamelets, closed symbols refer to Broadened Preheat – Thin Reaction (BP-TR) zone flames, and filled hexagrams/pentagrams represent broadened reactions. The definition for $Ka_{T,P}$ is provided in Eq. 1.6.

The different symbol types in Fig. 5.1 indicate the type of study each case was from and what type of flame structure was associated with it (note that a more detailed diagram linking each case to its specific study is provided in Appendix C). In

general, open symbols indicate thin flamelets (i.e. thin preheat and reaction zones), closed symbols refer to BP-TR flames (i.e. broadened preheat and thin reaction zones), and closed pentagrams and hexagrams indicate broadened reactions from prior experimental and DNS studies, respectively. Here, a BP-TR flame is defined as one where its preheat layer or total flame thickness is, on average, a factor of two times larger than its measured laminar value. Likewise, a broadened reaction layer is identified as one possessing a heat release zone or an appropriate surrogate for one (e.g. CH-, HCO-, overlap-layer, etc. [45]) that is, on average, two times thicker than its measured laminar value. It should also be mentioned that the locations of the cases in Fig. 5.1 are based upon the information provided in Refs. [2–10, 13, 14, 18, 20, 21, 23–30, 32, 94], but since each study reports different variants of u'/S_L and $L_x/\delta_{F,L,P}$, those locations are somewhat approximate. For details regarding the positioning of the cases in Fig. 5.1 as well as how particular structures were associated to them, see Appendix C.

Upon inspection of the data points in Fig. 5.1, it is apparent that the Klimov-Williams criterion (i.e. $Ka_{T,P} = 1$) fails to isolate thin flamelets (open symbols) from BP-TR flames (closed symbols) as theorized. In fact, a significant number of turbulent flames classified into the theoretical BP-TR regime (e.g. those from Refs. [2–13]) were observed to be relatively thin. Yet in this study, and in many others [9, 14, 16–23], BP-TR flames where observed in cases classified into the predicted BP-TR regime. Based on Fig. 5.1, it appears as though the line separating thin flamelets and BP-TR flames must have a negative slope; hence, these inconsistencies cannot be reconciled by simply shifting the original Klimov-Williams limit to larger $Ka_{T,P}$ values. This implies that $Ka_{T,P}$ is, at the very least, not the only appropriate parameter for delineating thin flamelets from BP-TR flames.

In an attempt to overcome these inconsistencies, we have used our results and those from prior experimental studies to develop a new *Measured Regime Diagram*.

This diagram is displayed in Fig. 5.2.

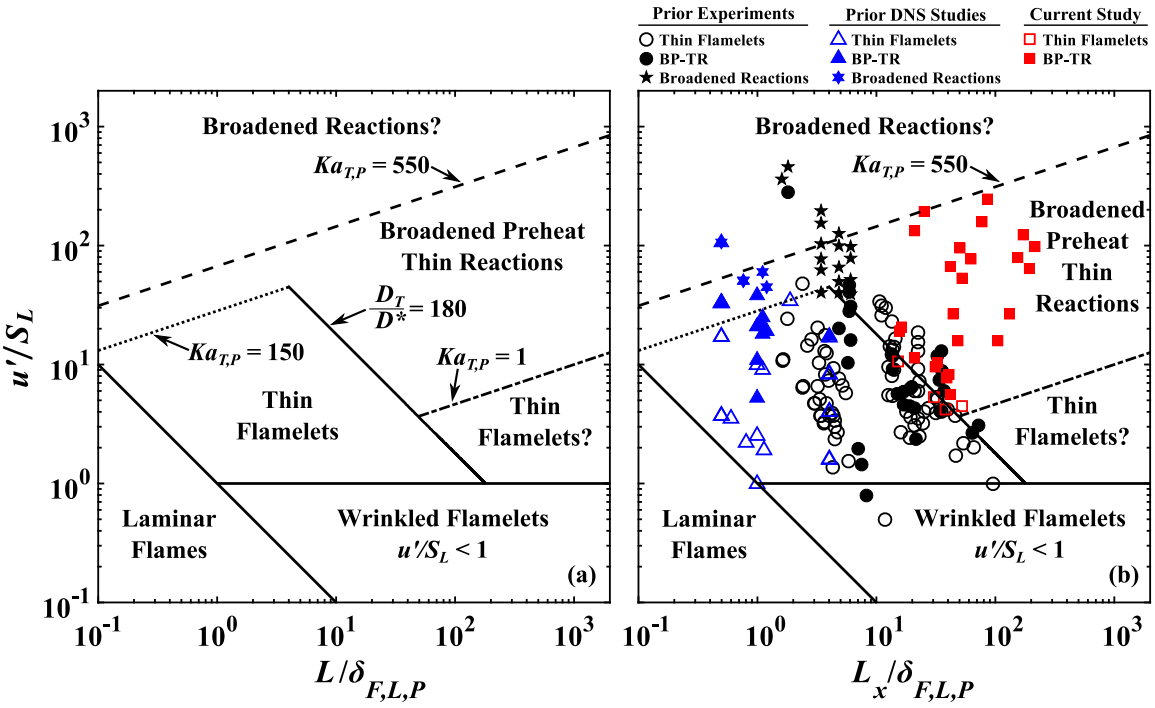

Figure 5.2: The new *Measured Regime Diagram* with prior and current cases included. Solid lines represent measured boundaries, while dashed and dotted lines refer to plausible boundaries (which are discussed in Sections 5.2 and 5.3). Open symbols indicate thin flamelets, closed symbols refer to Broadened Preheat – Thin Reaction (BP-TR) zone flames, and filled hexagrams/pentagrams represent broadened reactions. A more detailed diagram depicting which study each case was from is provided in Appendix C, while details for each of the cases in the prior studies are provided in Tables C.1 and C.2. Definitions for D^*, $Ka_{T,P}$, and D_T are provided by Eqs. 1.3, 1.6, and 5.1, respectively.

As in Fig. 5.1, open and closed symbols in Fig. 5.2b represent thin flamelets and BP-TR flames, respectively, while filled hexagrams/pentagrams represent broadened reactions. Solid lines in Fig. 5.2 indicate measured boundaries, while dashed or dotted lines signify plausible boundaries. Furthermore, the aforementioned cautions regarding the positioning and classification of cases hold true for the cases in Fig. 5.2b. And again, additional information regarding the positioning of these cases and how particular structures were ascribed to them are provided in Appendix C.

A total of 151 cases from 16 separate experimental studies (including this one)

were used to provide a detailed assessment of the Borghi Diagram and to develop the new *measured* boundary (solid line) in Fig. 5.2. These cases are included in Fig. 5.2b and though they certainly do not represent *all* experimental studies of turbulent premixed flames, to the best of the author's knowledge, they do signify all such studies that provided sufficient information on both turbulent statistics and flame structure. Furthermore, while prior DNS studies have provided insights into the structure and dynamics of turbulent premixed flames, because of their idealized configurations and other simplifications (e.g. turbulence forcing functions, periodic boundary conditions, reduced chemistry sets, etc.), their results were not utilized in the development of the measured boundary (solid line) in Fig. 5.2. However, since multiple DNS studies cover the region of small $L_x/\delta_{F,L,P}$ and large u'/S_L, which is void of experimental cases, their results are used in Sections 5.2 and 5.3 to support the addition of plausible boundaries (dotted or dashed lines) within this region of Fig. 5.2.

5.1 Measured boundary separating thin flamelets and BP-TR flames

Inspection of Fig. 5.2b indicates that a better metric for distinguishing thin flames from those with broadened preheat layers exists. Specifically, we hypothesize that preheat zone broadening should occur when the turbulent diffusivity (D_T) sufficiently exceeds the molecular diffusivity within the preheat layer (i.e. D^*). That is, the boundary separating regimes of thin flamelets and BP-TR flames should be defined by:

$$\frac{D_T}{D^*} = \frac{u'L}{S_L\delta_{F,L,P}} \geq C, \tag{5.1}$$

where C is a constant to be determined from experiments and D_T is chosen in terms of u' and L (after Pope [48]). However, note that defining D_T in terms of Taylor scale quantities will yield the same expression as that given in Eq. 5.1 – the only difference being the value of C. Also, notice that in defining D_T and D^* in this way, their ratio is equivalent to $Re_{T,P}$ (see Eq. 1.4).

To assess our hypothesis, we have incorporated Eq. 5.1 into Fig. 5.2. As can be seen, when $C \approx 180$ this metric does a substantially better job of dividing cases with thin flamelets (open symbols) from those with BP-TR flames (close symbols) than the Klimov-Williams criterion. In fact, if one looks closely, one will notice that this metric does a good job of separating the cases in this study that posses thin preheat layers from those with broadened preheat layers. Furthermore, the notion that the onset of preheat zone broadening should be marked by a diffusivity parameter is consistent with results from numerical flamelet simulations preformed by Li et al. [21]. Namely, by replacing the molecular diffusion coefficients with increasing values of D_T they found that the CH_2O- (i.e. preheat) layer thicknesses increased dramatically while the CH- (i.e. reaction) layer thicknesses increased only modestly (see Fig. 11 of Ref. [21]). As to why D_T/D^* must exceed the specific value of 180 for preheat zone broadening to occur is still an open question, and answering it will require additional detailed experiments and simulations. However, it is interesting to note that the results from the flamelet simulations performed by Li et al. [21] also demonstrated that the overall flame thickness did not substantially increase once D_T/D^* exceeded a value of 180. This indicates that the preheat zones of their flamelets transitioned to a fully broadened state once $D_T/D^* \geq 180$, which provides further support for our metric.

Beyond the fact that our metric is consistent with the results provided in Fig. 5.2, it, unlike the Klimov-Williams criterion, which is based on intuitive scaling arguments, stems from physical reasoning and has ties to laminar flame theory. Specifically, the

fact that the structure of a laminar preheat zone is controlled by molecular diffusive properties is what gave rise to the hypothesis that preheat zone broadening should be governed by a metric based on the turbulent diffusivity. Yet, in addition to having ties to laminar flame theory, this metric is more physically sound than the classical notion that preheat layers will broaden as soon as Kolmogorov eddies are small enough to fit within them. It is reasonable that this classical notion fails to capture the broadening of preheat layers because the constraint it posits, while likely to be necessary, is probably not sufficient. That is, just because the Kolmogorov scale, or some other scale that is arbitrarily larger than η, is smaller than $\delta_{PH,L}$ does not mean that there is sufficient energy at that scale to severely disrupt the structure of the preheat zone. However, it makes sense that preheat zone broadening will occur if the flow field provides enough energy, mixing, or inertia (recall that $D_T/D^* = Re_{T,P}$) to permit the diffusion of warm species (e.g. CH_2O, HO_2, etc.) further upstream of the reaction layer than molecular diffusion will allow on its own. Thus, based on: 1) the physical reasoning laid out here, which is linked to the well-established, premixed laminar flame theory; 2) the ability of our metric to properly distinguish thin flamelets from BP-TR flames in Fig. 5.2b; and 3) its consistency with numerical results from Li et al. [21], we argue that Eq. 5.1 with $C \approx 180$ is the most reasonable metric by which thin flamelets should be segregated from BP-TR flames.

Since our metric is validated by experimental results, it is considered to be a *measured* boundary. Such boundaries are represented by solid black lines in Fig. 5.2, while dotted or dashed lines represent plausible boundaries. The reason those boundaries are merely considered to be plausible is that there is simply not enough experimental evidence to verify them. For example, the lower boundary given to the Broadened Reactions regime is considered to be plausible because, to the best of the author's knowledge, only two experimental studies (i.e. those by Dunn et al. [11–13] and Zhou et al. [17–19]) have provided sufficient evidence for the existence

of broadened reactions. Therefore, at this time some speculations are required to develop those boundaries, which are discussed in the following sections.

5.2 Plausible boundary to the Broadened Reactions regime

In contrast to broadened preheat zones, conclusive experimental evidence for the existence of broadened reactions is rare. In fact, to the best of the authors' knowledge, the only two experimental studies to have provided definitive evidence of broadened reactions are those by Zhou et. al. [17–19] and Dunn et al. [11–13]. However, since multiple DNS studies (see Refs. [26, 27, 32]) have provided evidence of broadened reactions, their results were used when developing the plausible boundary to the Broadened Reactions regime in Fig. 5.2. Yet, even with these additional DNS cases, there is not enough evidence to properly locate the lower boundary of the Broadened Reactions regime. In fact, one cannot draw a straight line that reasonably separates BP-TR cases from those with broadened reactions. Nonetheless, as Fig. 5.2 shows, we suggest that the lower boundary to the Broadened Reactions regime should be defined by a constant value of $Ka_{T,P}$, specifically: $Ka_{T,P} \geq 550$. This is because the boundary $Ka_{T,P} = 550$ is consistent with all of our results and contradicts as few as possible from the experimental [11–13, 17–19] and DNS [26, 27, 32] studies with broadened reactions.

The reason we have chosen to mark the boundary to the Broadened Reactions regime with a constant value of $Ka_{T,P}$, instead of some other parameter, is based on the following notions. For one, the fact that the majority of cases to have exhibited broadened reactions possessed $Ka_{T,P}$ values that were much greater than 100 (see, for example, Refs. [11–13, 26, 27, 32]) along with the fact that none of our cases with $Ka_{T,P} > 100$ exhibited broadened reactions suggests that the theoretical limit typically cited for the Broadened Reactions regime – $Ka_{T,P} = 100$ – is flawed. In other words, the notion that a reaction layer will broaden as soon as η^* becomes

smaller than $\delta_{RZ,L,P}$ is not in agreement with the presently available measurements[1]. This can be understood by invoking the same reasoning put forth above for preheat layer broadening. Namely, just because eddies can penetrate a characteristic reaction layer does not mean that they possess enough energy to critically disrupt its structure. Furthermore, as was pointed out by Poinsot et al. [53], Roberts et al. [153], and Soika et al. [5], the Kolmogorov scale is particularly unsuited for determining the transition into the Broadened Reactions regime. This is because viscous dissipation significantly increases at the Kolmogorov scale, and thus eddies at this scale are likely annihilated before they can severely perturb the reaction layers. Therefore, we too argue that the Kolmogorov scale should not be considered when defining boundaries on the regime diagram.

Instead, we believe that the onset of reaction layer broadening will occur when a scale larger than the Kolmogorov length scale, which we will refer to as ℓ, is both capable of penetrating characteristic reaction layers (with thickness $\delta_{RL} < \delta_{F,L}$) and contains enough turbulent kinetic energy to severely disturb them. That is, we hypothesize that reaction layer broadening will only occur if both of the following relations are satisfied:

$$\ell \leq \delta_{RL} = C_1 \delta_{F,L} \tag{5.2}$$

and

$$u'_\ell \geq C_2 S_L, \tag{5.3}$$

where C_1 (which depends on the particular definitions of δ_{RL} and $\delta_{F,L}$) and C_2 are constants and u'_ℓ is the RMS of the velocity fluctuations at scale ℓ, which, in assuming

[1]Recall that η^* is determined from Eq. 1.8 where the kinematic viscosity was assumed to be equivalent to $D^* \approx 7.2 \times 10^{-5}$ m^2/s. Furthermore, based on Peters' definition: $\delta_{RZ,L,P} = 0.1\delta_{F,L,P}$ mm, which is nearly an order of magnitude smaller than the FWHM of CH-layers determined from measurements and a 1-D laminar flame simulation (see Table 2.2 and Ref. [131]).

homogeneous, isotropic turbulence (HIT), is related to the turbulent kinetic energy at scale ℓ. Though ℓ represents an arbitrary length scale, if one assumes that ℓ lies within the inertial subrange of turbulence (which is reasonable since in most practical combustion devices the integral length scale is likely much lager than the flame thickness), both it and u'_ℓ can be related to tangible quantities (i.e. u' and L). Specifically, by Kolmogorov's notion of a turbulent cascade, we know that $u'^3/L = u'^3_\ell/\ell$, thus from Eqs. 5.2 and 5.3 it follows that:

$$\frac{u'}{S_L} = \frac{C_2}{C_1^{\frac{1}{3}}} \left(\frac{L}{\delta_{F,L}} \right)^{\frac{1}{3}}. \tag{5.4}$$

Of course, inspection of Eq. 5.4 indicates that C_1 and C_2 are related to $Ka_{T,P}$. Specifically, based on the right most term in Eq. 1.6 and Eq. 5.4 we find that:

$$Ka_{T,P} = \left(\frac{C_2^3}{C_1} \right)^{\frac{1}{2}}. \tag{5.5}$$

Thus, our hypothesis that both Eqs. 5.2 and 5.3 must be satisfied in order for reaction layer broadening to occur is identical to saying that such a phenomenon will occur only if $Ka_{T,P}$ exceeds the critical value $\sqrt{C_2^3/C_1}$[2]. Specifically, notice that C_1 and C_2 are related to the right most term in Eq. 1.6, which is repeated here for convenience:

$$Ka_{T,P} = \left(\frac{u'^3 \delta_{F,L,P}}{S_L^3 L} \right)^{\frac{1}{2}}. \tag{5.6}$$

In order to arrive at the specific term in Eq. 5.6 Peters assumed a specific form for

[2]Unfortunately, the values of C_1 and C_2 cannot be known a priori; thus, identifying the value that $Ka_{T,P}$ must exceed for broadened reactions to exist requires experimental measurements. Though as noted above, based on the presently available data, no constant value of $Ka_{T,P}$ perfectly divides cases with broadened from those with thin reaction layers. Hence, we simply speculate that the boundary to the Broadened Reactions regime should be defined by a line satisfying $Ka_{T,P} \geq 550$.

$\delta_{F,L}$ and that the Kolmogorov scale should be represented by η^*, which is based on $\nu^* = D^* \approx 7.2 \times 10^{-5}$ m^2/s. However, as we have shown, one can arrive at the specific definition in Eq. 5.6, or at least something similar (i.e. $C_2/C_1^{\frac{1}{3}} = Ka_{T,P}^{\frac{2}{3}}$), without considering the Kolmogorov scale and without invoking Peters' specific assumptions. If instead one assumes that the Kolmogorov scale is irrelevant in terms of turbulence–flame interactions and that eddies within the inertial subrange are the most likely to affect the structure of practical flames, then ϵ is the only relevant parameter associated with the turbulent flow. Then if one assumes that the scaling $\epsilon \sim u'^3/L$ [1] holds true near a reacting flame front (i.e. where it may not be valid to assume HIT) and that S_L and $\delta_{F,L}$ are the primary parameters for characterizing combustion processes, via dimensional reasoning, one arrives at a dimensionless parameter similar to that in Eq. 5.6. Since this parameter represents the ratio of a characteristic rate associated with the flow field (i.e. ϵ) to one corresponding to the combustion chemistry (i.e. $S_L^3/\delta_{F,L}$) it is of course best described as a Karlovitz number.

However, Peters' definition for $\delta_{F,L}$ and his assumption that the Kolmogorov scale should be based on $\nu^* = D^*$ are not commonly invoked. Instead, the laminar thermal thickness ($\delta_{th,L} = (T_p - T_0)/\frac{dT}{dx}|_{max}$, where T_p is the temperature of the products), which is often more than twice as large as $\delta_{F,L,P}$ (see, for example, Table 2.2), is generally used to represent $\delta_{F,L}$, and the Kolmogorov length scale is typically determined from ν_0 (η_0). When using $\delta_{th,L}$ and η_0, the turbulent Karlovitz number takes on the following form:

$$Ka_{T,0} = \frac{\tau_{th,L}}{\tau_{\eta_0}} = \frac{\nu_0}{S_L}\frac{\delta_{th,L}}{\eta_0^2} = \left(\frac{S_L\delta_{th,L}}{\nu_0}\right)^{\frac{1}{2}}\left(\frac{u'^3\delta_{th,L}}{S_L^3 L}\right)^{\frac{1}{2}}, \tag{5.7}$$

where $\tau_{th,L} = \delta_{th,L}/S_L$ is a characteristic flame time scale based on the thermal thickness and τ_{η_0} is the Kolmogorov time scale based on ν_0. While the various terms in Eq. 5.7, or some variant of them, are commonly used to define the turbulent

Karlovitz number, like Aspden [94][3], we believe that Eq. 5.6 provides the most appropriate definition for the turbulent Karlovitz number and that with this definition it represents the most appropriate parameter for bounding the Broadened Reactions regime. The reasons for this are that: 1) it summarizes our hypothesis regarding the onset of reaction layer broadening (i.e. Eqs. 5.2 and 5.3); 2) for a particular flame, a constant value of the parameter in Eq. 5.6 identifies the level of turbulence that interacts at a particular scale associated with that flame (see Refs. [26, 29, 94]), which is not necessarily true of Eq. 5.7; 3) it is not based upon the ratio between a characteristic flame scale and the Kolmogorov scale within cool reactants (e.g. $(\delta_{F,L}/\eta_0)^2$), which, as Table 2.1 indicates, results in unrealistically high Ka_T values[4] ; 4) it is directly linked to the parameters that makeup the axes of the regime diagram; and 5) it provides a clearer and more general definition than that in Eq. 5.7 (i.e. there is no need to determine approximate values for η, $\delta_{F,L}$, and/or δ_{RL}).

Our reasoning for basing this hypothesis on turbulent kinetic energy rather than turbulent diffusion was motivated by the fact that all of the broadened reaction cases in Fig. 5.2 possess lower values of D_T/D^* than our cases, which all have thin reaction layers. Further motivation for not using D_T/D^* to mark the boundary of the Broadened Reactions regime stems from the results of the flamelet simulations preformed by Li et al. [21], which demonstrated that increased diffusivity does not affect the reaction layers as much as the preheat layers (see Fig. 11 of Ref. [21]). Thus, we hypothesized that the turbulent kinetic energy at a scale comparable to the reaction layer thickness (e.g. u'_ℓ) needs to be sufficiently large in order for a

[3]Note that the only difference between the Ka_T Aspden [94] proposed and the one in Eq. 5.6 is the choice of $\delta_{F,L}$. While this difference will result in a slightly different value of C_1 (and hence critical Karlovitz number) that marks the boundary to the Broadened Reactions regime, based on the discussion in Section 5.4, clearly such a minor difference is trivial.

[4]Take for example, Case5B-0.85, its $Ka_{T,P}$ and $Ka_{T,0}$ values are 83 and 751, respectively. While the former correctly suggests that this case falls within the BP-TR regime, the latter implies that this case should lie well within the Broadened Reactions regime, though based on Fig. 4.6 it clearly does not. Furthermore, the notion that it is incorrect to define the relevant turbulent Karlovitz number in terms of η_0 is consistent with the arguments put forth by Lapointe et al. [32].

reaction layer to broaden. As we have shown above, this leads to $Ka_{T,P}$ being the governing parameter for dictating the onset of reaction layer broadening. Because $Ka_{T,P}$ represents a comparison between a rate associated with the turbulence and one corresponding to the reaction processes, the above hypothesis is also consistent with laminar flame theory. That is, unlike the structure of a laminar preheat layer, which is primarily governed by a convective-diffusive balance (i.e. the molecular transport of heat upstream of the reaction layer), the laminar reaction layer structure is also controlled by the rates of key reactions (see pages 27 and 28 of Ref. [1]). Therefore, it would be expected that a parameter comparing rates (e.g. $Ka_{T,P}$), rather than one comparing diffusivities (e.g. D_T/D^*), would dictate the onset of reaction layer broadening.

5.3 Plausible boundaries to the BP-TR regime

In addition to the plausible boundary defined by $Ka_{T,P} \geq 550$, several others have been incorporated into Fig. 5.2. The first is the boundary defined by $Ka_{T,P} = 1$ and $D_T/D^* \geq 180$. The reason we have included this plausible boundary stems from our notion that a reaction layer will only broaden if both turbulent scales smaller than it exist within the flow field and those scales contain sufficient energy. Though instead of turbulent kinetic energy, we have shown that preheat zone broadening is governed by a parameter based on the turbulent diffusivity (see Section 5.1). Thus, it is plausible that preheat zone broadening will only occur if both the turbulent diffusivity is sufficiently large and scales smaller than $\delta_{F,L,P}$ exist within the reactants' flow field[5]. Since all of the turbulent scales are larger than $\delta_{F,L,P}$ within the region defined by $Ka_{T,P} < 1$, $D_T/D^* \geq 180$, and $u'/S_L > 1$, and since only one experimental case exists there (see Ref. [9]), we speculate that this region should be considered

[5]Note that we are specifying the scales must be smaller than $\delta_{F,L,P}$ because its values for methane-air flames provided a better approximation of laminar preheat zone thicknesses computed from a 1-D laminar flame simulations than $\delta_{th,L}$.

a Thin Flamelet regime. The second plausible boundary incorporated into Fig. 5.2 extends the BP-TR regime to a region of large u'/S_L and small $L/\delta_{F,L,P}$, and is defined by $Ka_{T,P} = 150$ and $D_T/D^* \leq 180$. We have added this boundary because several DNS cases that lie within the region defined by $150 < Ka_{T,P} < 550$ and $D_T/D^* \leq 180$ were found to have broadened preheat layers (see Refs. [26, 27, 32]). Moreover, it makes sense that as a case goes from the Thin Flamelets regime to the Broadened Reactions regime its preheat layers will broaden before its reaction layers. Therefore, we believe that cases located within this region will possess broadened preheat yet thin reaction layers. The reason for marking this boundary by $Ka_{T,P} = 150$ is because $Ka_{T,P}$ quantifies the level of turbulence available at scales comparable to $\delta_{F,L,P}$, and because the line it defines is consistent with experimental and DNS cases.

Notice, however, that this latter plausible boundary contradicts our finding that preheat zone broadening should be controlled by turbulent diffusion. Nevertheless, it is consistent with the notion that a layer will broaden once there is enough energy contained within the scales that are of its size or smaller. Hence, we speculate that either turbulent kinetic energy or turbulent diffusion can dictate the broadening of preheat layers, depending on the magnitude of $L/\delta_{F,L,P}$. Specifically, and as can be seen from Fig. 5.2, the former governs the transition from thin to broadened preheat layers when $L/\delta_{F,L,P}$ is relatively small, but when $L/\delta_{F,L,P}$ is large, the latter controls this phenomenon. Of course, the extent of preheat layer broadening may differ between these separate metrics. For instance, based on the notion of a "*penetration-broadening-penetration cascade*" put forth by Lipatnikov [154], which posits that once a layer is broadened by a small eddy, a succession of larger eddies can broaden it until it is as thick as the largest eddies within the flow field, it would be expected that cases with larger values of $L/\delta_{F,L,P}$ will exhibit broader preheat zones. Though this idea of a "*penetration-broadening-penetration cascade*" has not been rigorously verified, it is consistent with our finding that the average preheat layer thickness increases with

axial distance from our burner. Furthermore, a comparison between our cases and those from the DNS studies of Aspden et al. [26, 27] and Lapointe et al. [32] supports the idea that cases with large $L/\delta_{F,L,P}$ will possess larger preheat zones, because our cases appear to possess much broader preheat layers than theirs. Of course, detailed preheat zone measurements from cases with the same u'/S_L but different $L/\delta_{F,L,P}$ are necessary to validate this hypothesis.

5.4 Cautions when interpreting regimes and their boundaries

Although the *Measured Regime Diagram* in Fig. 5.2 extends the Thin Flamelet and BP-TR regimes to larger u'/S_L and $Ka_{T,P}$ values than was previously theorized (see Fig. 1.2a), this does not necessarily imply that the flamelet concept [59] is valid throughout those regions. Recall that the flamelet concept is composed of two parts: 1) the reaction layers are thin; and 2) they locally propagate at the laminar flame speed. While we have shown that the former is true throughout the Thin Flamelet and BP-TR regimes in Fig. 5.2, the latter may not be. In fact, previous experimental studies (see, for example [73, 150, 155, 156]) have shown that the global turbulent consumption speeds of cases within those regimes are much greater than turbulent flame speeds derived from flamelet concepts (e.g. integral of flame surface densities). That is, multiple experiments have suggested that the reaction layers of flames within the Thin Flamelet and BP-TR regimes do not locally propagate at a value of S_L. Therefore, one should exercise caution when attempting to utilize a model based on the flamelet concept to simulate cases that fall within these regimes.

A final observation of the boundaries in Fig. 5.2 is that even though they are either plausible or verified by measurements, they do not perfectly distinguish various flame types. For instance, there are cases situated below and to the left of the measured boundary defined by $D_T/D^* \approx 180$ that, on average, were found to possess broadened preheat layers. Likewise, a few cases positioned above and to the right of

this boundary were identified as being thin. Thus, even though the boundary defined by $D_T/D^* \approx 180$ is considered to be "measured," it does not strictly separate all BP-TR cases from thin flamelet cases. Hence, this boundary, as well as the others in Fig. 5.2, should not be considered as strict demarcations. Rather, we believe that they should be viewed from a probabilistic standpoint. Specifically, we contend that the closer a case is to a particular boundary separating two regimes, the more probable it is for that case to manifest either, or potentially a combination of both, of the structural features associated with those regimes. Or to put it another way, we believe that the diagram in Fig. 5.2 should be thought of as a probability map with the likelihood that a flame will manifest the structural features forecasted by a specific regime being highest for cases located within and far away from the boundaries of that regime. Determining the functions that potentially govern such probability distributions is undoubtedly impractical, as they are likely to be affected by countless parameters such as geometrical configuration, flame stabilization mechanisms (e.g. piloted, bluff body, swirl, etc.), average eddy-flame residence-times, upstream history effects, thermo-diffusive properties, reactant preheating [32], etc. A rough estimation of such probability functions could perhaps be developed from signed distance functions that assign a probability to a case based on its proximity to particular boundaries. However, verifying the appropriateness of this view point will require future work. For now the main takeaway is that the boundaries in Fig. 5.2 should be interpenetrated as *transition regions* rather than firm delimiting boarders.

CHAPTER VI

Conclusions and Future Efforts

Overall, this dissertation has provided a wealth of knowledge on the structure of premixed flames subjected to extreme levels of turbulence. Obtaining this knowledge was facilitated by applying high-fidelity, laser-based imaging techniques to premixed methane–air flames produced by a Bunsen-type burner. This burner was capable of stabilizing flames subjected to a wide rage of turbulence levels. Specifically, 28 cases were studied with integral length scales (L_x) as large as 43 mm, turbulence levels (u'/S_L) as high as 246, and turbulent Karlovitz ($Ka_{T,P}$) and Reynolds numbers ($Re_{T,0}$) up to 533 and 99,000, respectively. Three high-fidelity PLIF based techniques were utilized to visualize the preheat and reaction layer structures of these flames. Reaction layer images were obtained from two of those techniques, which included the overlap-method (which involves taking the product of simultaneously acquired PLIF images of CH_2O and OH) and PLIF imaging of CH radicals. Preheat layer images were also derived from the overlap method, namely, thresholded CH_2O-LIF signals were used to mark the preheat layers of the flames considered here. Through the application of a novel local thresholding technique, average preheat and reaction layer thicknesses were extracted from these images, which permitted the quantitative assessment of predictions made by classical premixed combustion theories. Specifically, results from the cases studied in this dissertation as well as 166 others from prior

investigations were used to assess the theoretical boundaries of the Borghi Diagram. The primary results of this work are summarized in the following.

6.1 Flame visualization

Prior to interpreting the results from the diagnostic techniques implemented here, their ability to visualize preheat and reaction layers was assessed. In this dissertation, preheat layer information was derived from thresholded CH_2O-LIF signals. While previous studies have used CH_2O-LIF signals as a surrogate for marking preheat layers, prior justification for this has mainly stemmed from qualitative observations, chemical kinetic models, and numerical flamelet simulations. Thus, to demonstrate the robustness of using thresholded CH_2O-LIF signals as an indicator of the preheat region within the flame considered here, simultaneous Rayleigh scattering and CH_2O-PLIF imaging was preformed. Namely, both qualitative and quantitative comparisons were made in three specific cases, which included a laminar and an extremely turbulent case (i.e. Case 6A-0.85).

Qualitative comparisons were based on sample preheat and temperature filed images. Specifically, preheat layer profiles obtained from individual paths drawn normal to the preheat layers were found to only exhibit non-zero signal levels within regions of elevated temperature (e.g. between $\sim$350 K and $\sim$1100 K). To facilitate more holistic qualitative comparisons over the entire area spanned by the images, the edges of the preheat layers in the turbulent flames were superimposed onto their respective temperature fields. This indicated that these edges bounded regions wherein the temperature ranged from $\sim$330 K and $\sim$1100 K. Quantitative assessment was then performed by identifying the probability distributions of temperature along those edges in the three cases considered. All three distributions displayed two peaks, one corresponding to the upstream and the other to downstream edges of the preheat layers. The most probable values of those peaks were identified and used to char-

acterize the average range of temperatures bounded by the preheat layers. For all three of the cases considered, this range was ∼350 K to ∼1200 K. Therefore, based on the qualitative results and the fact that this range of temperatures corresponds to those in the theoretical description of preheat layers, the technique employed here for visualizing preheat layers was determined to be robust.

In addition to assessing the preheat layer visualization technique implemented here, the robustness of the two independent methods employed to image reaction layers – overlap-layer and CH-PLIF imaging – were assessed. Specifically, radial profiles of flame surface density (FSD) derived from the overlap- and CH-layers of four separate cases were compared on both a qualitative and a quantitative basis. In a qualitative sense, these profiles were found to agree in both magnitude and in their rate of decay with increasing radial distance. Quantitative assessment was based on a flame surface wrinkling parameter (Ω), which was computed by integrating those profiles over the radial direction. The percent differences between values of Ω computed from the CH-PLIF and overlap-layer imaging techniques were less than 21% in all four of the cases considered. The fact that those percent differences were no greater than the ones computed from independent, yet spatially coincident CH-PLIF measurements, clearly indicates that these profiles were also similar in a quantitative sense. Given such similarity between FSD-profiles derived from the overlap- and CH-layers, as well as the similar structural features exhibited by those layers, it is concluded that both techniques are robust tools for visualizing reaction layers in extremely turbulent premixed methane–air flames.

6.2 Preheat and reaction layer structure

One of the primary objectives of this dissertation was to understand the effects intense ($4.2 < u'/S_L < 25$) and extreme ($25 < u'/S_L < 246$) levels of turbulence have on the structural features of premixed flames. To this end, the aforementioned diag-

nostic tools were applied to premixed methane–air flames subjected to a wide range of turbulence levels. The application of those diagnostics provided both qualitative and quantitative information; the primary results derived from that information is listed below.

1. Sample preheat layer images suggested that the width of the preheat layers within the least turbulent cases considered in this dissertation (i.e. $Re_{T,P} < 180$) were thin and laminar-like. In contrast, such images clearly indicated that preheat layers become very broad as turbulence level increases. In fact, in the most turbulent cases considered in this study ($Re_{T,P} \gtrsim 2500$) the preheat layers were observed to fill the entire core of the flame brush. In addition to increasing with turbulence intensity, the width of preheat layers were also observed to increase with axial distance from the burner (x/D). Thus suggesting that factors beyond turbulence level (e.g. upstream history effects) can play a substantial role in determining the structure of preheat layers.

2. Sample overlap-layer and CH-PLIF images told a much different story regarding the structure of reaction layers within the flames considered here. Specifically, in all of the cases considered in this dissertation, the reaction layers did not change significantly in appearance and were, for the most part, thin. However, the sample overlap- and CH-layer images did indicate that as turbulence intensity increases the reaction layers became more wrinkled and contorted. In fact, sample CH-PLIF images from some of the most turbulent cases considered here, demonstrated that the reaction layers can become very densely packed and so convoluted that the reactants cannot be discerned from products with reaction layer images alone.

3. To corroborate the previously listed qualitative results, a novel local thresholding algorithm was implemented to extract average preheat and reaction layer

thicknesses from the flames studied in this dissertation. Consistent with observations from the sample preheat layer images, the average preheat layer thicknesses were found to increase exponentially with increasing values of u'/S_L (up to ∼10 times their measured laminar value). Additionally, average preheat layer thicknesses initially increased with axial distance from the burner, but subsequently decreased as the tip of the flame was approached. All but four of the cases considered in this dissertation possessed average preheat layer thicknesses that were greater than twice that of a corresponding laminar flame, and thus those cases are considered to possess broadened preheat layers. Since each case studied here had $Ka_{T,P}$ values that were greater than unity, the prior fact implies that many of the cases were consistent with prediction made by the theoretical Borghi Diagram. However, this also implies that the four cases that were identified as having thin preheat layers are in contradiction with the classical notion that preheat layers will broaden once $Ka_{T,P}$ exceeds a value of one.

4. Consistent with sample reaction layer images, the average reaction layer thickness in all 28 cases studied here remained thin. In fact, none of them were found to possess average reaction layer thicknesses in execess of twice their respective measured laminar values, even though the turbulence level (u'/S_L) increased by a factor of ∼60. Also, unlike the average preheat layer thicknesses, the average reaction layer thicknesses (based on CH-PLIF images only) were found to be relatively insensitive to increases in x/D. The fact the reaction layers of each flame considered here were all relatively thin is somewhat consistent with prediction from the theoretical Borghi Diagram, since most of them had $Ka_{T,P}$ values that were less than 100. However, the six flames that possessed $Ka_{T,P}$ in excess of 100 – which are thus classified into the predicted Broadened Reactions regime – are clearly in contradiction with the notion that reaction

layers will broaden once $Ka_{T,P}$ exceeds a value of 100 (i.e. η becomes smaller than $\delta_{RZ,L,P}$).

5. Provided that there was sufficient shielding from room air entrainment (i.e. no stratification of products), locally extinguished reaction layers were rarely observed. In fact, the percentage of locally extinguished overlap-layers (i.e. reaction layers) was no greater than 2%. However, broken reactions were observed in cases wherein cool gases were entrained and allowed to interact with the reaction layers. This was made evident by combined CH-OH PLIF images acquired at a rate of 10 kHz. Specifically, a time series of these images showed a pocket of entrained cool gas coming in contact with CH-layers (i.e. the reaction zones) and subsequently causing them to extinguish. Though local extinction events were rare, their occurrences were typically associated with such entrainment. Hence, applications wherein cool species are mixed with the products – such as Rich-Quench-Lean gas turbine engines – should account for possible localized extinction events.

6.3 Measured Regime Diagram

The aforementioned inconsistencies between the results presented here and the theoretical Borghi diagram suggest that this diagram requires modifications if it is to server as robust tool for distinguishing regimes of turbulent premixed combustion. However, the results of this study span only a portion of the Borghi Diagram; therefore, to facilitate a more comprehensive assessment of its boundaries, results from 23 prior experimental and numerical investigations of turbulent premixed flames were considered. The primary results stemming from this assessment are provided in what follows.

1. Results from the 28 cases considered here and those from 15 prior experimen-

tal studies, indicated that the Klimov-Williams criterion (i.e. preheat zones broaden when $\eta^* \leq \delta_{F,L,P}$ or equivalently when $Ka_{T,P} \geq 1$) fails to distinguish thin flamelets (i.e. thin preheat and reaction zones) from BP-TR flames (i.e. those with broadened preheat yet thin reaction zones). Furthermore, the results clearly indicate that a boundary with a negative slope is required to separate these regimes, thus a simple shift of the Klimov-Williams to a larger $Ka_{T,P}$ value is not a sufficient solution. Instead, a new boundary is proposed, which possess a slope of -1 and is based on the idea that the turbulent diffusivity ($D_T = u'L_x$) must sufficiently exceed the molecular diffusivity within the preheat layer ($D^* = S_L\delta_{F,L,P}$). This metric was observed to agree far better with experimental results than the traditional Klimov-Williams criterion when $D_T/D^* \approx 180$. Therefore, it is concluded that the metric: $D_T/D^* \approx 180$ is the appropriate criterion for delimiting regimes of thin flamelets and BP-TR flames.

2. Since the number of experimental studies either to have observed broadened reactions or to have possessed considerably large $Ka_{T,P}$ values (i.e. $Ka_{T,P} > 100$) are sparse, a comprehensive assessment of the boundary to the Broadened Reactions regime is not possible at this time. However, results from several experimental (including this one) and DNS studies clearly indicate that the theoretical boundary defined by $Ka_{T,P} = 100$ does not separate the BP-TR regime from the Broadened Reactions regime. For example, none of our six cases having $Ka_{T,P} \geq 100$ (i.e. $\eta^* \leq \delta_{RZ,L,P} = 0.1\delta_{F,L,P}$) displayed evidence of broadened reactions. Yet, since prior numerical and experimental studies have reported the existence of broadened reactions, such a boundary likely exists. Furthermore, we hypothesize that this boundary should be based on the notion that a reaction layer will only broaden if there are both scales smaller than it and if those scales possess enough turbulent kinetic energy to significantly disrupt the

reaction processes. As was demonstrated, this is equivalent to saying that reaction layer broadening will occur only when $Ka_{T,P} = (u'/S_L)^{3/2} (L/\delta_{F,L,P})^{-1/2}$ exceeds a critical value. Based on the currently available data, that value is estimated to be $Ka_{T,P} \geq 550$, which implies that the BP-TR regime extends well beyond what was previously theorized.

3. Based on the conclusions outlined in points 1 and 2, we were able to develop a new *Measured Regime Diagram*. While this diagram possesses measured and plausible boundaries, this does not mean that as soon as one of them is crossed a flame will immediately exhibit a new structural configuration. For example, the measured boundary defined by $D_T/D^* \approx 180$ does not perfectly separate all thin flamelet cases from BP-TR cases; hence, it, and the other boundaries, should not be thought of as absolute demarcations. Rather, we believe that these boundaries should be viewed from a probabilistic standpoint. Namely, the probability of observing the particular flame structure predicted by a regime is higher for cases positioned within and further from its boundaries than those located closer to or outside of them. Though determining the functions governing these probabilities will require future work, it is likely that multiple factors such as burner geometry, Lewis number, axial distance from the flame base, etc., will influence them.

6.4 Looking to the Future

Though this dissertation deepens our understanding of the effects extreme levels of turbulence (e.g. those found in practical combustion devices) have on the structure of premixed flames, there is still a tremendous amount of physical phenomena surrounding premixed combustion that requires elucidation. For instance, several questions that still lack definitive answers include:

1. What is the structure of extremely turbulent premixed flames in temperature space, and do flamelet models capture this structure?

2. How are the structure and dynamics of premixed heavy-hydrocarbon flames affected by turbulence, and how, if at all, is this effect different from that in more simplistic hydrocarbon fuels? Namely, note that the majority of the cases considered in Fig. 5.2 consisted of relatively simple, gaseous hydrocarbon fuels (e.g. methane and propane). However, practical combustion devices operate with heavy-hydrocarbon fuels that begin in liquid form (e.g. kerosene, JP-8, Jet-A1, etc.). Thus, there is a pressing need to study highly-turbulent heavy-hydrocarbon flames.

3. Is there a universal formula for turbulent consumption speeds of envelope-type flames (i.e. those generated by Bunsen burners) that is independent of fuel type?

4. How does increased pressure affect the structure and dynamics of extremely turbulent premixed flames? Specifically, note that while the majority of the cases in Fig. 5.2 were conducted at atmospheric pressure, most practical combustion devices operate at pressures that are five to ten times greater than that of the standard atmosphere.

5. Is there a concrete and simplistic way to emulate the geometric dependence of the structure and dynamics of premixed flames?

6. What leads to the onset of unstable phenomenon such as autoignition, blow out, and thermoacoustic instabilities, and can such phenomenon be predicted and controlled?

Certainly, this list of questions is far from complete, but it does provide a sense of the challenges that still face the combustion science community. While pursuing answers

to these questions will undoubtedly require a significant amount of effort, expending such effort is warranted. This, as was discussed in Section 1.1, is because the ability to harness energy from combustion processes in a manner that is affordable, efficient, and environmentally friendly is paramount to the advancement and survival of our civilization. And each answer that is obtained and rigorously verified for the questions above brings us one step closer to realizing that ability.

Sure, detailed answers to several, if not all, of the aforementioned questions will likely remain elusive for decades to come. Nevertheless, the advances made and the understanding attained by the combustion science community over the past +60 years should provide hope that one day such answers will indeed be obtained. Of course, at that point in time, new questions will arise and combustion scientists will undoubtedly labor vigorously to identify answers to them. This process of answers leading to more questions is true for every science. Each bit of understanding that is gained often leads to even more unanswered questions. Such a *vicious circle* is quite frustrating. Moreover, it is unlikely that human beings will ever be able to grasp every facet of the universe we live in. However, there should be solace in the fact that with each advancement in science, however small or grand, our understanding of the cosmos and the physical laws that govern it deepens. Most of all, hopefully, in gaining such understanding we are able to improve the world we call home.

APPENDICES

APPENDIX A

Example demonstrating the time and cost of a fully resolved numerical simulation

Estimating the time and cost of performing a DNS of the turbulent flow through a practical device requires knowledge of the range of spatiotemporal scales expected to exist within a turbulent flow. Figure A.1 illustrates this by presenting a sample grid of a simulation and various turbulent "structures" that are either resolved (blue whorls) or unresolved (maize whorls).

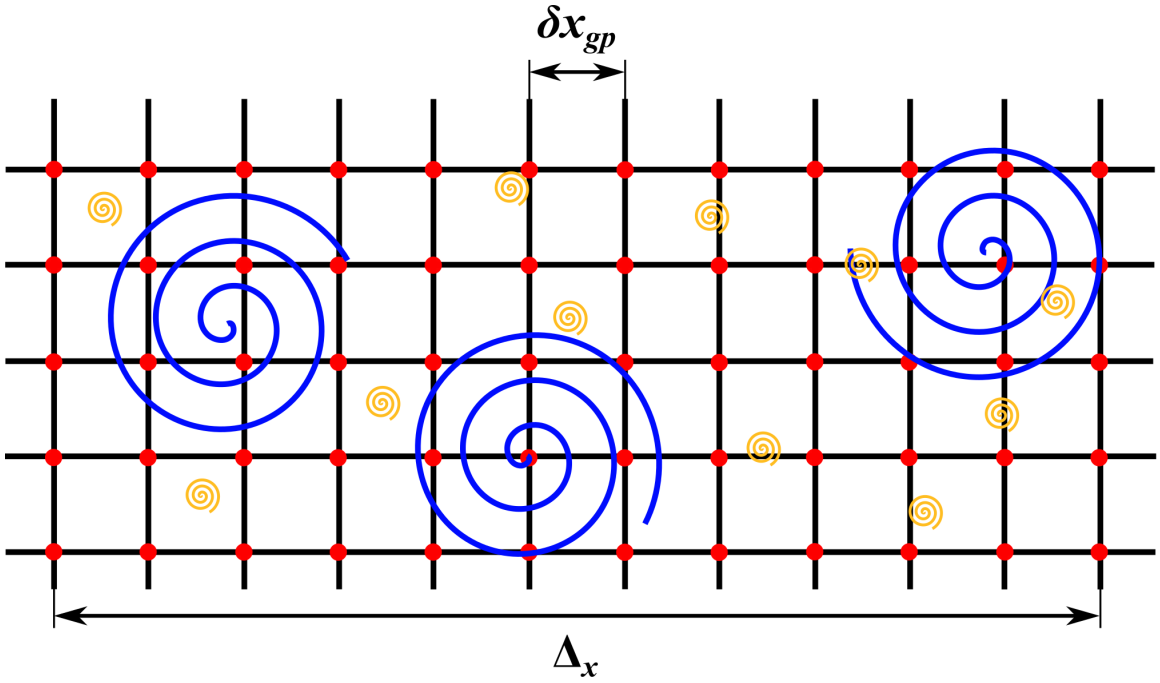

Figure A.1: Sketch depicting the discrete grid of a computational domain in a DNS. The red dots indicate the grid points at which the computations are solved and the blue and maize "whorls" represent resolved and unresolved turbulent structures, respectively.

Each red dot in Fig. A.1 represents a single grid point at which the governing equations of a turbulent reacting flow (i.e. the Navier-Stokes equations [1, 47, 48]) can be solved. Because these equations can only be solved at those discrete points, any information of the turbulent flow that does not overlap with them cannot be accessed. For example, because the blue whorls in Fig. A.1 overlap ∼6 grid points their characteristics can be ascertained via the computation. However, because the maize whorls only exist in the regions between each grid point, their attributes cannot be obtained from the simulation. Therefore, in order to solve a turbulent flow problem in its entirety, the domain of the computation must be as large as the physical size of the device in question and the spacing between its grid points (δx_{gp}) needs to be sufficiently small so that the smallest scales are fully resolved. This latter point is met by ensuring that the Nyquist criterion is satisfied; namely, δx_{gp} must be less than half of the smallest expected structures within a turbulent flow.

The size of the smallest structures within a turbulent flow can be estimated from Kolmogorov's first similarity hypothesis, which suggests that their statistics are universal and are solely dictated by the viscosity (ν) and the dissipation rate of turbulent kinetic energy (ϵ) [46]. Thus, based on dimensional reasoning, the approximate length scale of the smallest structures within a turbulent flow (i.e. the Kolmogorov length scale) is defined by:

$$\eta = \left(\frac{\nu^3}{\epsilon}\right)^{\frac{1}{4}}. \tag{A.1}$$

This implies that $\delta x_{gp} < 0.5\eta$ must be satisfied in order for a DNS to be capable of resolving the smallest expected structures within a turbulent flow.

The ratio of the overall size of the computational grid in one direction (Δ_x) to δx_{gp} is what determines the number of grid points necessary in that direction (N_x). The size of Δ_x is of course set by the geometry of particular problem being solved. Typically, Δ_x is slightly larger than the integral length scale (L), which represents the scale that contains most of the turbulent kinetic energy (TKE). Thus, the number of grid points in one direction is given by the following:

$$N_x = \frac{\Delta_x}{\delta x_{gp}} \gtrsim \frac{L}{\eta}. \tag{A.2}$$

Then, from Eq. A.3 and the definition given for the turbulent Reynolds number (Re_T) in Eq. 1.2, one can show that:

$$N_x \gtrsim \frac{L}{\eta} = Re_T^{\frac{3}{4}}. \tag{A.3}$$

Finally, because turbulent flow problems occur in 3-D space, the total number of grid

points necessary is approximately: $N_x^3 \sim Re_T^{\frac{9}{4}}$. Note, however, that this approximation assumes that the size of the device in question is the same in all directions, which is not necessarily true. Nevertheless, this approximation should be sufficient for the order of magnitude analysis considered here.

As was mentioned in Section 1.1, a DNS is solved by numerically integrating the Navier-Stokes equations at each grid point in the computational domain. In order to capture the smallest temporal scales associated with a flow, the time between each discreet integration step (δt_i) must be sufficiently short. Specifically, δt_i must be less than the time it takes a fluid element to travel the shortest expected scales within the flow; that is, $\delta t_i \lesssim \eta/u'$. If it is assumed that the size of the device being considered is approximately L, the time it would take for a fluid element to traverse the length of the devices is $\sim L/u'$. Therefore, the total number of integration steps necessary to solve the turbulent flow through this device is proportional to L/η, which is equivalent to $Re_T^{\frac{3}{4}}$. Again, as was pointed out in Section 1.1, this indicates that the total number of floating point operations that are necessary to explicitly compute the properties of a turbulent flow is *proportional* to Re_T^3.

Estimations for the duration and cost of performing a DNS of the flow through a gas turbine were provided in Section 1.1. These estimations were obtained by considering the notion that within practical gas turbines $Re_T \sim \mathcal{O}(10^8)$ [33]. This, of course, implies that solving for the turbulent flow properties through such devices requires $\mathcal{O}(10^{24})$ floating point operations[1]. If all 11,472 nodes available to Pleiades, the largest supercomputer owned by NASA, are allocated to one problem, it can perform $\sim 6\times10^{15}$ floating point operations per second (FLOPS) [49]. Thus, if Pleiades was employed to solve this problem, it would take $\sim$5.5 years to do so. Additionally, the cost to perform such a computation can be determined from pricing listed in Ref.

[1] As noted in Section 1.1, this is merely just an estimate. The number of floating point operations required to solve a turbulent flow problem is *proportional*, not equal, to Re_T^3. Thus, the values determined in this exercise should be considered as order of magnitude ($\mathcal{O}(\cdot)$) estimates, rather than exact values.

[50]. Namely, the total cost is the product of: 1) the number of nodes used (i.e. 11,472 in this case); 2) the cost per node ($ 0.24); 3) the duration of the computation (in hours); and 4) a scaling factor to account for the efficiency of the particular computer being used (i.e. 4.04 for Pleiades) [50]. Thus, the cost to perform this computation on Pleiades is ∼500 million dollars.

As discussed in Section 1.1, such a computation only considers the turbulent flow and does not incorporate the added complexities of combustion processes. Moreover, the aforementioned analysis is only for a single computation. Optimization of practical combustion devices would require hundreds, if not thousands, of such computations. While there currently exists super computers that are faster than Pleiades (e.g. the Sunway TaihuLight computer can perform $\sim 93 \times 10^{15}$ FLOPS [157]), and though their speeds will continue to increase over time, it should be apparent that DNSs will never serve as a practical means by which to design and optimize combustion-based engines.

APPENDIX B

Reasoning for subtracting additional signal when generating preheat layer images

As mentioned in Section 3.1.2, the OH- and CH_2O-PLIF images used to generate preheat layer images had an additional amount of signal removed from them over and above the average background signals. Again, the reason for this was that subtracting average background fields in the manner outlined by Eq. 3.1 did not remove all of the background signal from those images. In order to illustrate this, sample OH- and CH_2O-PLIF images from Case2A-1.05 wherein a tungsten rod was used to block a portion of the laser sheet are presented in Fig. B.1. Even though average background fields were subtracted from the sample images in Fig. B.1 (i.e. via Eq. 3.1), the region (slit) void of laser light contains substantial levels of signal. As the profiles in the top right corner of Fig. B.1 indicate, the signal within the slit region ranged from 10% to 20% of local maximum values in the individual images. Furthermore, the sample images and plot in bottom row of Fig. B.1, which represent the average of a set of images from Case2A-1.05, demonstrate that the average signal level within the slit relative to local average maximum values was $\sim$17% for both the CH_2O- and OH-PLIF images. However, because there was no laser radiation within that region to induce any sort of fluorescence, such signal must have been the result of background

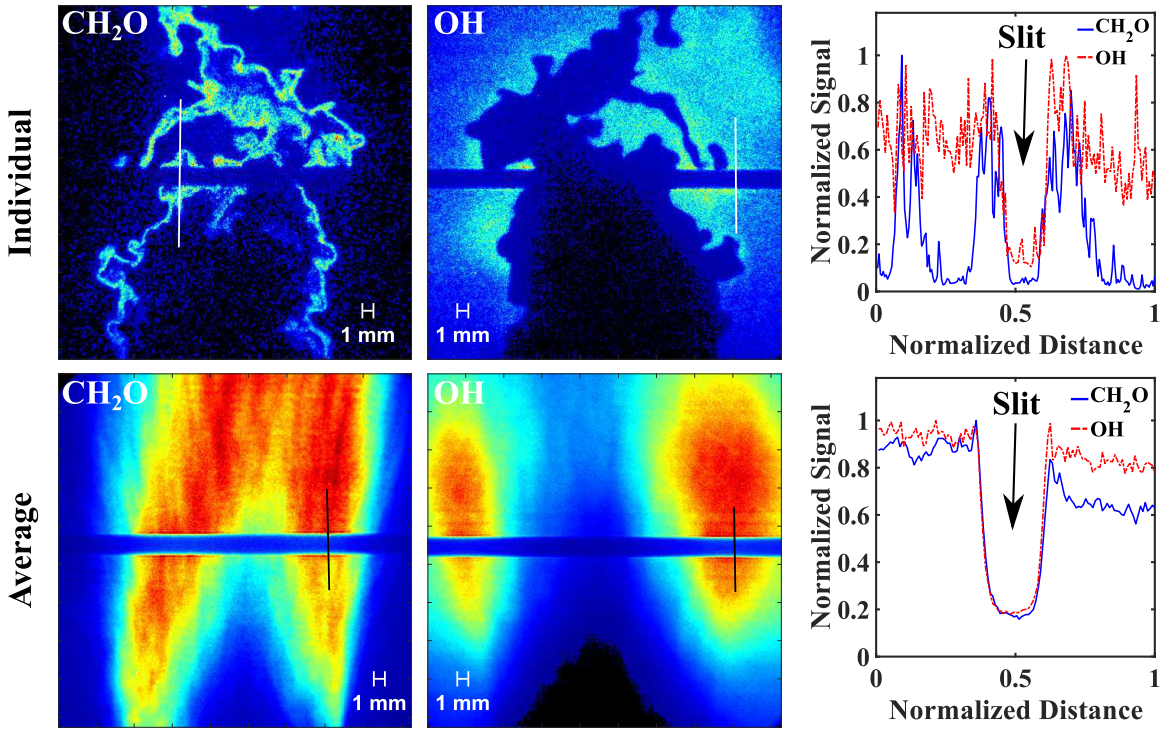

Figure B.1: Sample CH_2O- and OH-PLIF images wherein a portion of the laser sheet was blocked.

interferences over and above those accounted from in Eq. 3.1. The source of this additional background signal is unknown; however, since it is clearly not the result of primary laser-induced fluorescence and should be removed.

One thing to note, however, is that even though the images provided in Fig. B.1 were from a case studied in this dissertation, they were obtained with a slightly different diagnostic configuration than the one described in Section 2.2.2.3. Thus, the absolute values presented in Fig. B.1 do not directly apply to the CH_2O- and OH-PLIF images that were used to generate preheat layer images. Nevertheless, the sample images in Fig. B.1 are very similar to those obtained with the diagnostics outlined in Section 2.2.2.3, and hence they serve as an indicator of the fact that removing background signal via Eq. 3.1 is not always adequate. For this reason, and because there is no direct and easy way to accurately quantify this signal level over the whole imaging field, the additional subtraction and local thresholding steps

mentioned above were implemented to remove it.

APPENDIX C

Specification of cases from prior studies

The location, flame type, and the study associated with each case considered in Fig. 5.2 are depicted in Fig. C.1.

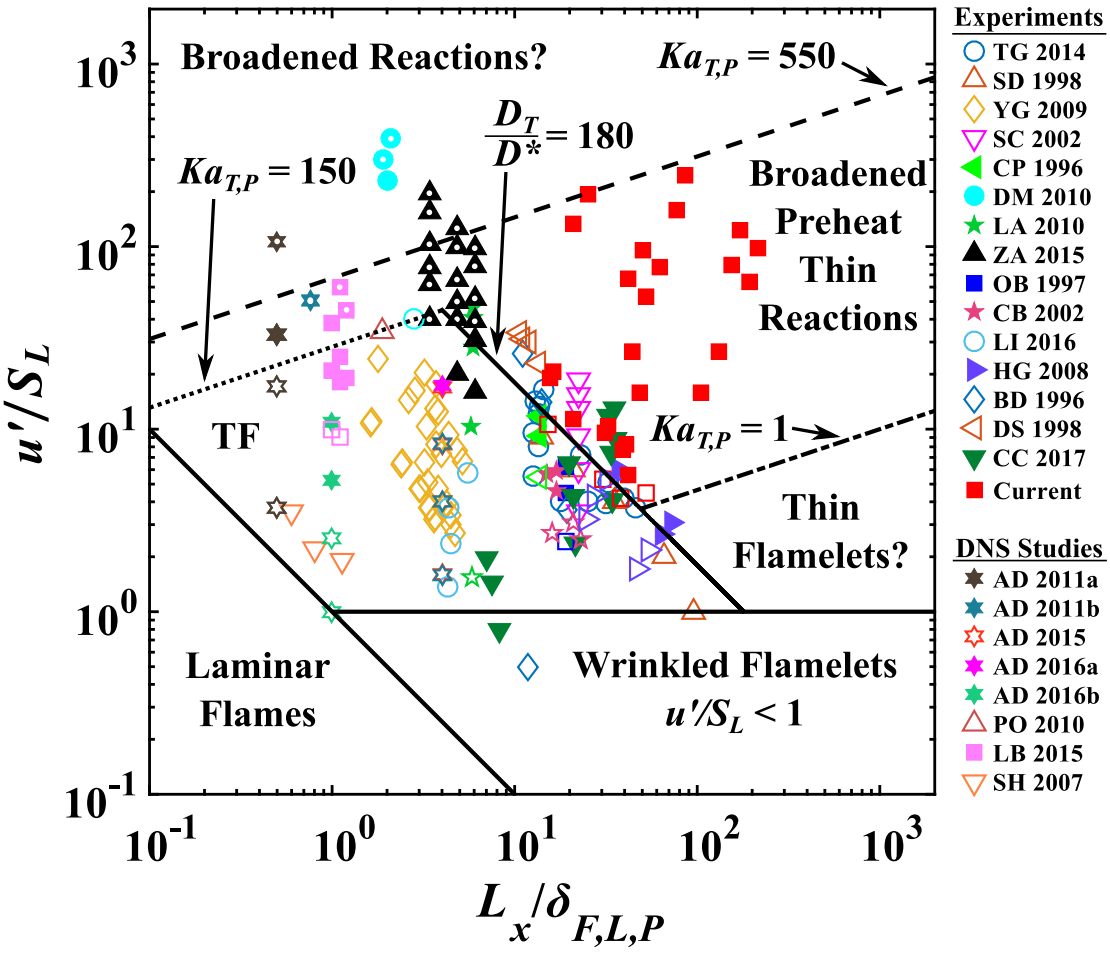

Figure C.1: The new *Measured Regime Diagram* with prior and current cases included. Solid lines represent measured boundaries, while dashed and dotted lines refer to plausible boundaries (which are discussed in Sections 5.2 and 5.3). Open symbols indicate thin flamelets, closed symbols refer to BP-TR flames, and those with white dots at the center represent broadened reactions. Details for each of the cases from prior experimental and DNS studies are provided in Tables C.1 and C.2, respectively. Definitions for D^*, $Ka_{T,P}$, and D_T are provided by Eqs. 1.3, 1.6, and 5.1, respectively.

As in the *Measured Regime Diagram* displayed in Fig. 5.2, open and closed symbols in Fig. C.1 represent thin flamelets and BP-TR flames, respectively, though cases with broadened reactions are indicated by symbols with white dots at the center. And again, solid lines in Fig. C.1 indicate measured boundaries, while dashed or dotted lines are plausible boundaries. Details of how particular preheat and reaction

zone structures were ascribed to cases from the prior experimental and DNS studies included in Figs. 5.2 and C.1 are provided in Tables C.1 and C.2, respectively.

Code & Ref.	Diagnostic	Flamelet Type	Metric
TG 2014 [2]	2-D R	TF	$\delta_{th}/\delta_{th,L}$ (see Fig. 12)
SD 1998 [5]	DS 2-D R	TF	$\delta_{th}/\delta_{th,L}$ (see Figs. 5 & 6)
YG 2009 [4]	2-D R	TF	$\delta_{th}/\delta_{th,L}$ (see Figs. 3–6)
SC 2002 [8]	2-D R	TF	Area between c contours see Table 1
CP 1996 [14]	2-D R	TF/BP-TR	Figs. 9, 11, & 16 (& Figs. 2 & 3 in [15])
DM 2010 [11–13]	R/F-PLIF	TF/BP-TR/BR	Fig. 4 in [12] & Figs. 6 & 4 from [11] & [13], respectively
LA 2010 [21]	F-PLIF	TF/BP-TR	Interpreted from sample images in Fig. 6
ZA 2015 [18]	2-D R/F-/C-PLIF	BP-TR/BR	Fig. 14
OB 1997 [20]	DS 2-D R	BP-TR	Interpreted from Fig. 11
CB 2002 [10]	DS 2-D R	TF/BP-TR	Interpreted from Fig. 9
LI 2016 [6]	2-D R	TF	Interpreted from PDF of δ_{th} in Fig. 11
HG 2016 [9]	2-D R	TF/BP-TR	Interpreted from δ_{th} values in Fig. 10
BD 1996 [3]	2-D R	TF	$\delta_{th}/\delta_{th,L}$ see Fig. 5
DS 1998 [7]	2-D R	TF	$\delta_{th}/\delta_{th,L}$ see Fig. 4
CC 2017 [23]	overlap method	BP-TR	δ_T/δ_L see Figs. 10 & 11

Table C.1: Details of prior experimental cases included in Figs. 5.2 and C.1. "R" stands for Rayleigh measurements and "DS R" implies dual sheet Rayleigh. "F-PLIF" and "C-PLIF" stand for CH_2O- and CH-PLIF, respectively. TF, BP-TR, and BR imply that the study observed either thin flamelets, BP-TR flames, or broadened reactions (or a combination of all three). c is the progress variable (see Eq. 3.12) and ρ is density.

Code & Ref.	Diagnostic	Flamelet Type	Metric
AD 2011a [26]	DNS	TF/BP-TR/BR	PDFs of $\|\nabla\rho\|$ (see Figs. 6 & 9) & from Figs. 5 & 8
AD 2011b [27]	DNS	BR	PDFs of $\|\nabla\rho\|$ (see Fig. 3)
AD 2015 [28]	DNS	TF	Thickness factor (see Fig. 5 of [30])
AD 2016a [29]	DNS	TF/BP-TR	Thickness factor (see Fig. 5 of [30])
AD 2016b [30]	DNS	TF/BP-TR	Thickness factor (see Fig. 5)
PO 2010 [25]	DNS	TF	Turbulent/laminar comparison in Fig. 7
LB 2015 [32]	DNS	BP-TR/BR	Fig. 4 & thicknesses reported in Table 6
SH 2007 [24]	DNS	TF	Based on $\|\nabla c\|_{c=0.3}$ & $\|\nabla c\|_{c=0.5}$ in Fig. 4

Table C.2: Details of cases from prior DNS studies included in Figs. 5.2 and C.1. "R" stands for Rayleigh measurements and "DS R" implies dual sheet Rayleigh. "F-PLIF" and "C-PLIF" stand for CH_2O- and CH-PLIF, respectively. TF, BP-TR, and BR imply that the study observed either thin flamelets, BP-TR flames, or broadened reactions (or a combination of all three). c is the progress variable (see Eq. 3.12) and ρ is density.

As was mentioned in Section 5.1, a case was classified as a BP-TR flame if its average preheat or total flame thickness exceeded twice that of its associated laminar value (see Refs. [2–9, 23]); otherwise it was considered to be a thin flamelet. If statistical thicknesses were not provided, preheat layer broadening was interpenetrated from either joint PDFs of the gradient of temperature (∇T) or progress variable (∇c), or simply from sample temperature or CH_2O-PLIF images (see Refs. [10–14, 17–21, 24–30, 32, 94]). For example, the DNS study by Sankaran et al. [24] used a plot of ∇c vs. c to demonstrate flame thickening (see Fig. 4 in Ref. [24]). Though that plot indicates that their preheat layers became thicker as the axial distance from their simulated burner increased, the $|\nabla c|_{c=0.3}$ values interpreted from that figure (which is used by others [2, 4, 5, 7] to represent the preheat layer thickness) suggests that their preheat layers were not more than twice as thick as that in a laminar

flame simulation. In contrast to that example, the ∇c vs. c plots provided in Fig. 9 of the experimental study by Chen and Bilger [10] indicate that several of the measured $|\nabla c|_{c=0.3}$ values were less than half of their laminar counterparts, and thus were considered to have broadened preheat layers. A similar approach was followed for classifying cases based on their reaction layer structures. Namely, if an average thickness value was provided for a case and that value exceeded twice that of an appropriate laminar value, that case was considered to have broadened reactions (see Refs. [2–5, 7–9, 17, 19, 23, 28–30, 32, 94]). But again, if statistical values were not provided, the reaction layers of a case were characterized by either joint PDFs of ∇T or ∇c (conditioned on temperatures or progress variables associated with reaction layers), or were interpenetrated from sample PLIF images of either CH-, HCO-, or overlap-layers (see Refs. [6, 10–14, 20, 21, 24, 25]).

As was pointed out in Section 5.1, the location of each case in Fig. 5.2 (and hence Fig. C.1) was based upon the information provided in Refs. [2–10, 13–21, 23–30, 32, 94]. The only exception to this was from the experimental study by Chen et al. [14]. Namely, though they used the lateral integral length scale to position their cases on the Borghi Diagram, to be consistent with the other data points in Figs. 5.2 and C.1, we used the longitudinal integral length scales they reported to position them. A drawback of simply using the u'/S_L and $L_x/\delta_{F,L,P}$ values directly reported in those studies is that each study provided a slightly different variation of them. For instance, while Peters' definition of $\delta_{F,L,P}$ was invoked to normalize L_x in this study (and in one other [2]), most used the laminar thermal thickness ($\delta_{th,L}$) to normalize L. Additionally, as is summarized in Table C.3, the L and u' values of the cases in Fig. 5.2 (and hence Fig. C.1) were not all acquired in the same manner.

Code & Ref.	Diagnostic	Flow Type	location
TG 2014 [2]	PIV	R/RN	x/D = 0.5
SD 1998 [5]	LDV	NA	NA
YG 2009 [4]	PIV	NA	near burner exit
SC 2002 [8]	LDV	R	15 mm above burner
CP 1996 [14]	LDV	R/NR	near burner exit
DM 2010 [11–13]	LDV	R/NR	x/D = 15 and r/D= 0.5
LA 2010 [21]	NA	NA	NA
ZA 2015 [18]	LDV	R	x/D = 30
OB 1997 [20]	LDV	R	NA
CB 2002 [10]	LDV/PIV	NR	25 mm above burner
LI 2016 [6]	NA	NA	NA
HG 2016 [9]	LDV	NR	NA
BD 1996 [3]	LDV	NR	x/D = 1.25
DS 1998 [7]	LDV	NR	NA
CC 2017 [23]	Hot Wire/Film	NR	Radially at x = 0

Table C.3: Details the the flow measurements made in the prior cases included in Fig. 5.2. R and NR imply that the data was collected under reacting and non-reacting conditions, respectively. NA signifies that either the measurements details were not not explicitly clear or results were based on estimations.

For example, in our study (and in others [3, 7, 9, 10]) u' and L values were determined from non-reacting flows, while in others [2, 11, 18, 20] they were acquired under conditions in which flames were present[1]. Furthermore, in some studies [2, 4, 14] (including this one), the u' and L values were based on measurements conducted near the exit plane of their burners, whereas in others [3, 5, 10, 11, 18, 20] they were derived from measurements made at locations closer to the average flame fronts. Of course, all of this implies that the locations of the cases in Fig. 5.2 (and hence Fig. C.1) are approximate.

It should also be mentioned that cases from studies by Dunn et al. [11–13] and Zhou et al. [17–19] are particularly difficult to interpret and place on the Borghi Diagram. This is because these studies utilize high-speed (i.e. 200 m/s to 400 m/s),

[1]Note that the latter can generate erroneous results if one is not careful to condition data on reactants only.

small diameter (i.e. 1.5 mm to 4 mm) jets to generate intense levels of shear driven turbulence. The majority of the other cases in Fig. 5.2 (and hence Fig. C.1) consist of flames subjected to more uniform turbulence that is generated far upstream of where they lie, which is more in line with the premises surrounding the development of the Borghi Diagram [11]. Furthermore, Dunn et al. [11–13] focus on highly sheared flames near the flammability limit, which possess computed laminar flame speeds and thicknesses that are questionably small and large, respectively. Thus, normalizing by these computed quantities is potentially misleading. Zhou et al. [17–19] take a more appropriate approach to generate these normalizing constants. Namely, they directly measure them from laminar flames stabilized on their burner, which should account for any affects their pilot may have had on their flames[2]. However, Zhou et al. [18] do not directly measure their integral length scales, but instead approximate them to be half of the width of their flow fields. While this is an acceptable approximation for non-reacting, turbulent jets, Dunn et al. [11] found that such approximations can differ from measured values by as much as 30%. So again, and in general, some caution is necessary when interpreting the specific positions implied in Fig. 5.2 (and hence Fig. C.1).

[2]Unfortunately, the approach could not be taken in our experiment because our burner is incapable of stabilizing a laminar flame.

APPENDIX D

Sample PLIF images from high-speed jet flame

As mentioned in Section 4.3, Zhou et al. [17–19] observed broadened reaction layers (e.g. CH-, HCO, and overlap-layers) in premixed methane–air flames produced and stabilized by a small diameter jet-burner (inner nozzle diameter of ∼2 mm). In an attempt to replicate their results, a small diameter jet-burner similar to theirs was constructed. A schematic of this burner and an image of it while it was operating are provided in Figs. D.1a and D.1b, respectively.

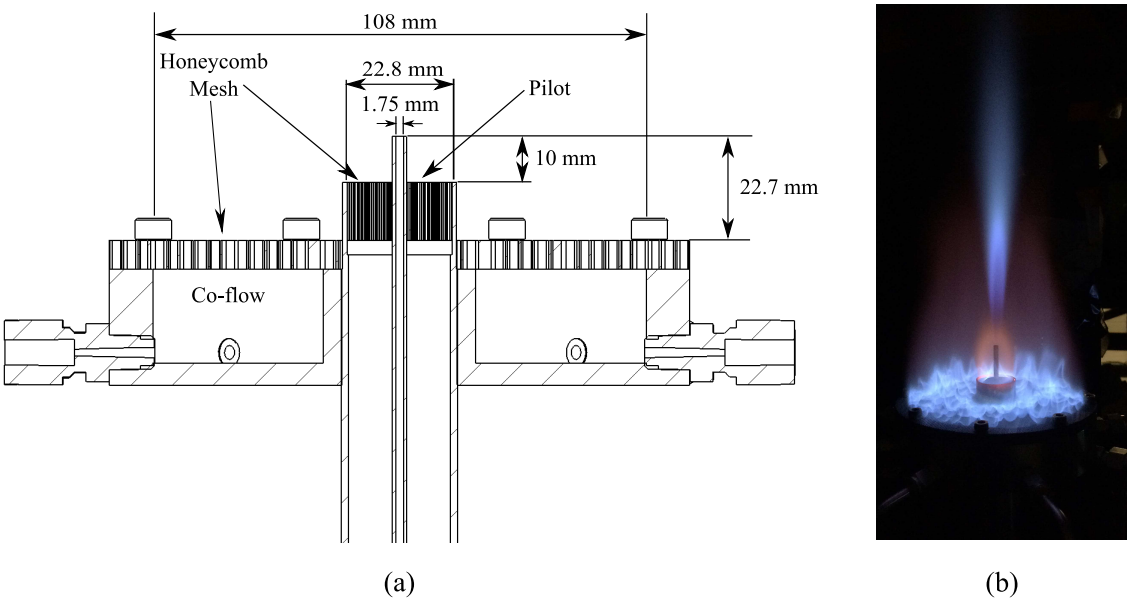

Figure D.1: (a) Schematic of high-speed jet burner. (b) Image of burner during experimentation.

The CH-PLIF imaging technique described in Section 2.2.2.2 was applied to a case very similar to that considered by Zhou et al. [17–19] (i.e. their case labeled "LUPJ1-418"). Specifically, here the bulk flow velocity and equivalence ratio of the premixed methane–air flame were set to ∼418 m/s and 1.05, respectively. Sample images from these efforts are presented in Figs. D.2 and D.3.

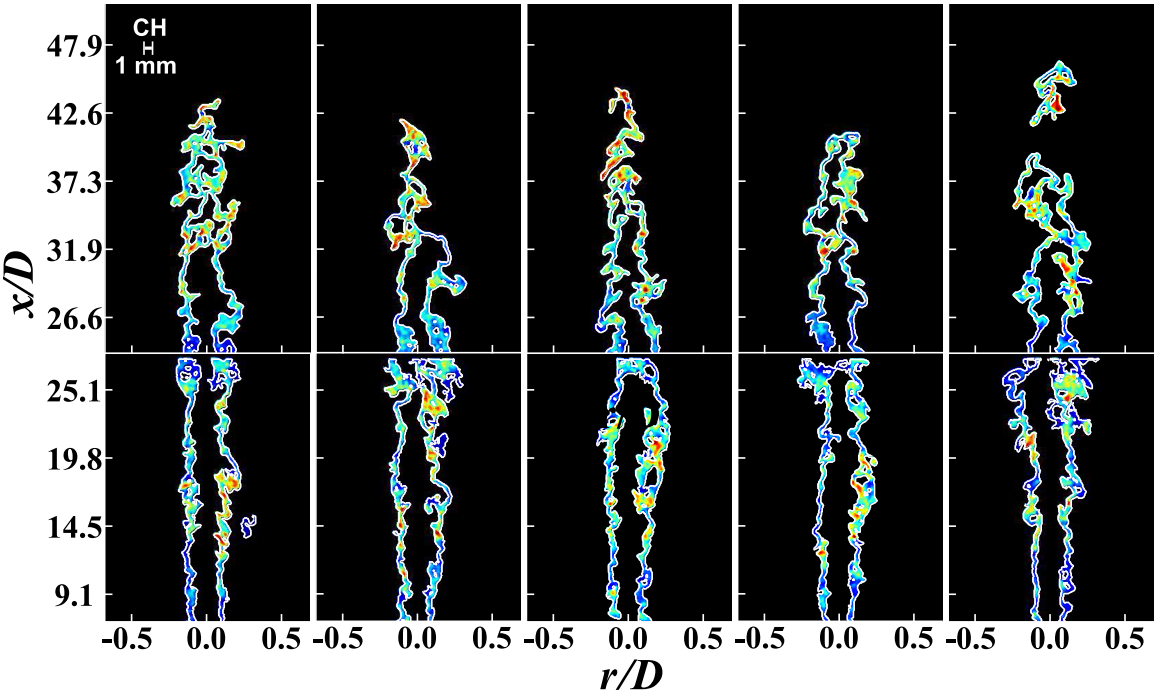

Figure D.2: Sample CH-PLIF images acquired from the high-speed jet burner. The bulk flow rate was set to ∼418 m/s and the equivalence ratio was 1.05. Note that here $D = 1.75$ mm.

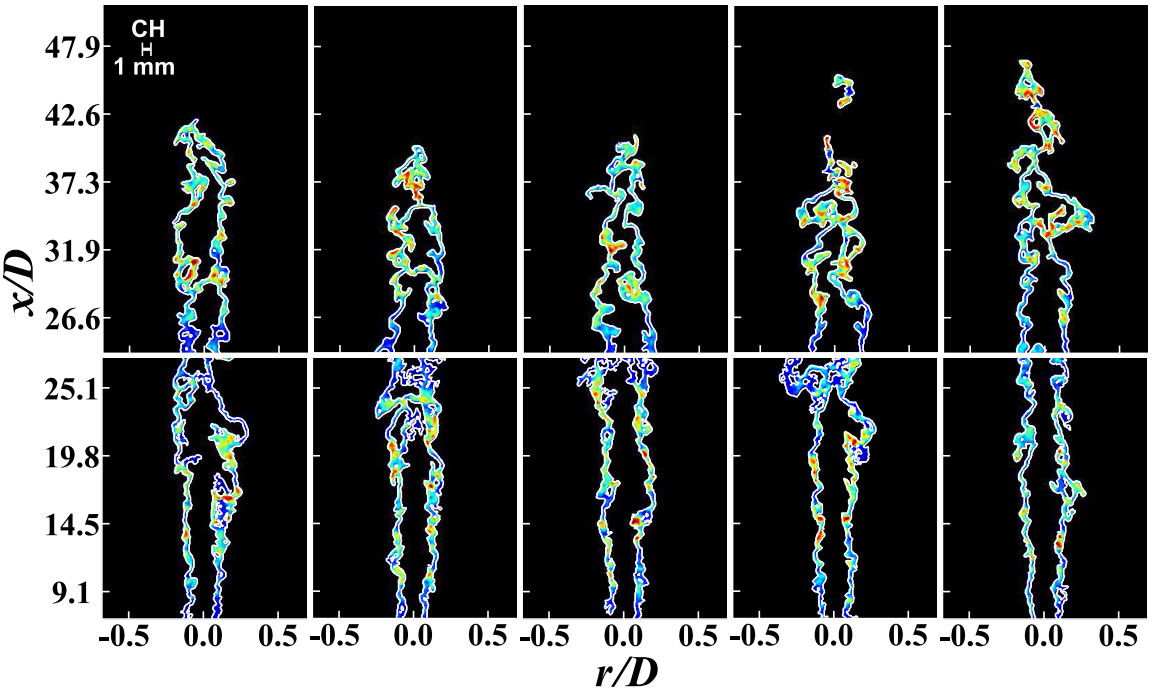

Figure D.3: Sample CH-PLIF images acquired from the high-speed jet burner. The bulk flow rate was set to ∼418 m/s and the equivalence ratio was 1.05. Note that here $D = 1.75$ mm.

Unlike the CH-layers presented by Zhou et al. [17–19] (see, for example, Figs. 2 and 7 of Refs. [17] and [18], respectively), those in Figs. D.2 and D.3 certainly do not appear to be significantly broadened. Granted, the layers in Figs. D.2 and D.3 have been locally thresholded to 50% of their local maximums. However, it is evident from Fig. D.4, which exhibits CH-PLIF images wherein only the background signal was removed and no thresholding was applied, that these reaction layers are, for the most part, relatively thin.

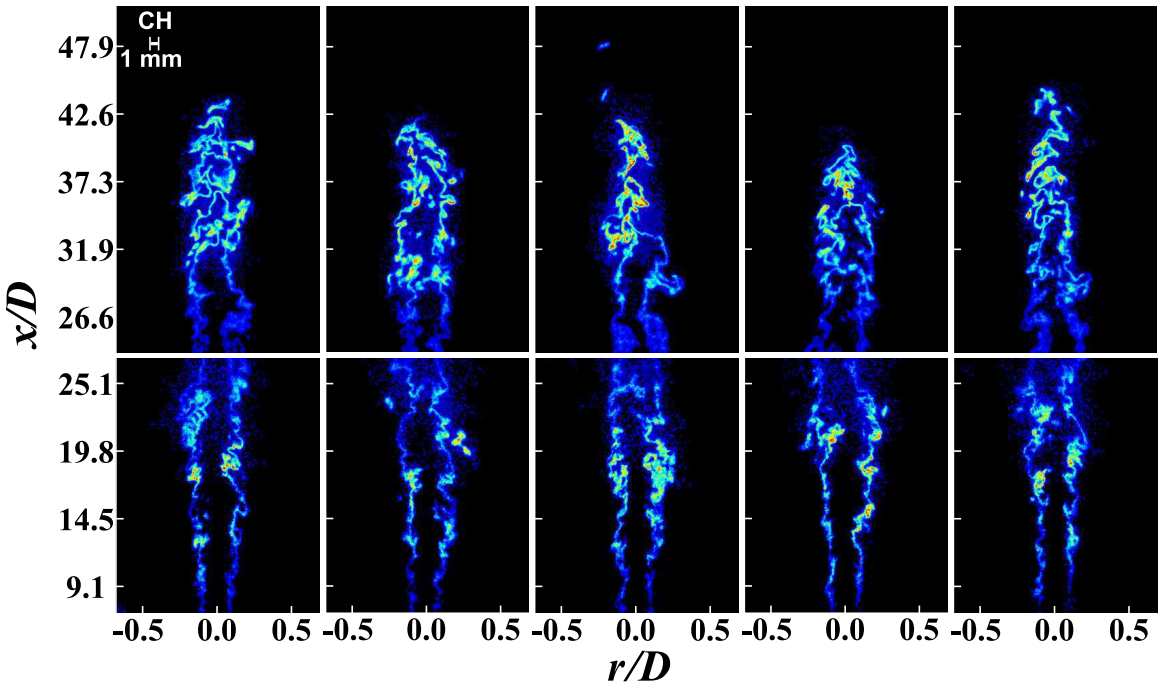

Figure D.4: Sample CH-PLIF images where the average background signal was removed but local thresholding was not applied. The conditions for these images were the same as those in Figs. D.2 and D.3.

While locally broadened regions are observed in Figs. D.2 – D.4, the average CH-layer thicknesses, which where determined by applying the methods outlined in Section 3.1.1 to ∼350 images acquired from both the upper and lower zones of Figs. D.2 – D.4, were found to be less than twice that of a laminar flame with $\phi = 1.05$. Furthermore, the average CH-layer thickness of a case with $\phi = 0.85$ was also found to be less than twice that associated with a laminar flame of the same equivalence ratio.

It is rather surprising that the specific jet-flame investigated here exhibited substantially different structural features than a very similar one studied by Zhou et al. [17–19]. The only major difference between their investigation and ours, is the particular diagnostic scheme utilized to conduct CH-PLIF imaging. As discussed in Section 2.2.2.2, in this dissertation CH-PLIF imaging was conducted by utilizing a continuously pulsed Nd:YAG pumped dye laser system to excite the overlapping

$Q_2(2)$ and $Q_2(6)$ transitions within the (0,0) band of the CH $C^2\Sigma^+$–$X^2\Pi$ system (near 314 nm). Zhou et al. [17–19], on the other hand, performed CH-PLIF imaging by using the frequency-doubled output from a pulsed alexandrite laser to excite a series of R-branch transitions within the (0,0) band of the CH $B^2\Sigma^-$–$X^2\Pi$ system (near 387 nm) [17, 158]. The laser pulses from the former system contained ∼0.2 mJ of energy and possessed a spectral linewidth and a temporal pulse width of 0.1 cm^{-1} and ∼7 ns, respectively [105]. In contrast, pulses from the latter laser system contained ∼70 mJ of energy and had a spectral linewidth and a temporal pulse duration of ∼8 cm^{-1} and ∼150 ns, respectively [158, 159].

The advantages of this latter approach are that: 1) 7 distinct transitions can be excited simultaneously; and 2) the CH radicals can relax and potentially be re-excited within the duration of a single pulse [158, 159]. However, as was pointed out by Kiefer et al. [159], a potential disadvantage of this technique is that it is susceptible to interferences from CH_2O-LIF signals. The fact that the sample CH-PLIF images presented in Figs. 2 and 7 of Refs. [17] and [18], respectively, more closely resemble the CH_2O-PLIF images that were acquired simultaneously with them than the sample images in Figs. D.2 – D.4, suggests that they were potentially affected by such interferences. Furthermore, based on the results presented in Ref. [158], which suggested that all 7 transitions can be saturated by a 15 mm tall sheet that contains pulse energies of ∼50 mJ, it is likely that Zhou et al. [17–19] was providing more energy than necessary. This, of course, could cause a reduction in the contrast between CH-LIF signals and those stemming from spurious background sources (e.g. CH_2O-LIF signals). However, these notions are merely speculations. And though the author trusts that Zhou et al. [17–19] implemented great care while performing their investigations, it is hard to rule out the possibility that their CH-PLIF images were somewhat affected by CH_2O-LIF signals until more definitive evidence that they were not is provided. For instance, implementing both approaches to CH-PLIF imaging

simultaneously would help shed light on why the results presented by Zhou et al. [17–19] differ so substantially from those presented in this dissertation.

BIBLIOGRAPHY

BIBLIOGRAPHY

[1] N. Peters, Turbulent Combustion, Cambridge Univeristy Press, 2000. xii, xv, xvii, xxii, xxiv, 5, 7, 8, 15, 16, 17, 19, 20, 21, 22, 31, 32, 92, 105, 115, 124, 126, 142

[2] P. Tamadonfar, Ö. L. Gülder, Experimental investigation of the inner structure of premixed turbulent methane/air flames in the thin reaction zones regime, Combust. Flame 162 (1) (2015) 115–128. xii, xv, 17, 24, 47, 77, 79, 87, 107, 114, 115, 116, 151, 152, 153, 154

[3] A. Buschmann, F. Dinkelacker, T. Schäfer, M. Schäfer, J. Wolfrum, Measurement of the instantaneous detailed flame structure in turbulent premixed combustion, Symp. Combust. (1996) 437–445. 24, 151, 154

[4] F. T. C. Yuen, Ö. L. Gülder, Premixed turbulent flame front structure investigation by Rayleigh scattering in the thin reaction zone regime, Proc. Combust. Inst. 32 II (2009) 1747–1754. 24, 79, 87, 151, 152, 154

[5] A. Soika, F. Dinkelacker, A. Leipertz, Measurement of the resolved flame structure of turbulent premixed flames with constant reynolds number and varied stoichiometry, Symp. (Int.) Combust. 27 (1) (1998) 785–792. 87, 122, 151, 152, 153, 154

[6] C. Leveniu, B. Renou, S. Dnil, D. Isvoranu, Accurate Measurements and Analysis of the Thermal Structure of Turbulent Methane/Air Premixed Flame, Energy Procedia 85 (2016) 329–338. 151, 153, 154

[7] F. Dinkelacker, a. Soika, D. Most, D. Hofmann, a. Leipertz, W. Polifke, K. Döbbeling, Structure of locally quenched highly turbulent lean premixed flames, Symp. (Int.) Combust. 27 (1) (1998) 857–865. 47, 62, 74, 77, 87, 151, 152, 153, 154

[8] I. Shepherd, R. Cheng, T. Plessing, C. Kortschik, N. Peters, Premixed flame front structure in intense turbulence, Proc. Combust. Inst. 29 (2) (2002) 1833–1840. 151, 154

[9] F. Halter, C. Chauveau, I. Gökalp, Investigations on the flamelet inner structure of turbulent premixed flames, Combust. Sci. Technol. 180 (4) (2008) 713–728. 116, 126, 151, 152, 153, 154

[10] Y.-C. Chen, R. W. Bilger, Experimental Investigation of Three-Dimensional Flame- Front Structure in Premixed Turbulent Combustion I : Hydrocarbon / Air Bunsen Flames, Combust. Flame 131 (2002) (2002) 400–435. 24, 116, 151, 152, 153, 154

[11] M. J. Dunn, A. R. Masri, R. W. Bilger, A new piloted premixed jet burner to study strong finite-rate chemistry effects, Combust. Flame 151 (2007) 46–60. 24, 47, 77, 105, 110, 114, 120, 121, 151, 154, 155

[12] M. J. Dunn, A. R. Masri, R. W. Bilger, R. S. Barlow, G. H. Wang, The compositional structure of highly turbulent piloted premixed flames issuing into a hot coflow, Proc. Combust. Inst. 32 II (2) (2009) 1779–1786. 24, 108, 151

[13] M. J. Dunn, A. R. Masri, R. W. Bilger, R. S. Barlow, Finite rate chemistry effects in highly sheared turbulent premixed flames, Flow, Turbul. Combust. 85 (3-4) (2010) 621–648. 24, 37, 39, 47, 77, 99, 105, 110, 116, 120, 121, 151, 153, 154, 155

[14] Y.-C. Chen, N. Peters, G. A. Schneemann, N. Wruck, U. Renz, M. S. Mansour, The detailed flame structure of highly stretched turbulent premixed methane-air flames, Combust. Flame 107 (3) (1996) 223–244. 22, 24, 99, 116, 151, 152, 153, 154

[15] M. S. Mansour, N. Peters, Y.-C. Chen, Investigation of scalar mixing in the thin reaction zones regime using a simultaneous CH-LIF/Rayleigh laser technique, Symp. (Int.) Combust. 27 (1998) 767–773. 22, 42, 151

[16] Y.-C. Chen, M. S. Mansour, Investigation of flame broadening in turbulent premixed flames in the thin-reaction-zones regime, Symp. (Int.) Combust. 27 (1) (1998) 811–818. 116

[17] B. Zhou, C. Brackmann, Z. Li, M. Aldén, X. S. Bai, Simultaneous multi-species and temperature visualization of premixed flames in the distributed reaction zone regime, Proc. Combust. Inst. 35 (2) (2015) 1409–1416. 24, 39, 42, 47, 77, 88, 99, 105, 108, 109, 110, 120, 121, 152, 153, 154, 155, 156, 157, 158, 159, 160, 161

[18] B. Zhou, C. Brackmann, Q. Li, Z. Wang, P. Petersson, Z. Li, M. Aldén, X. song Bai, Distributed reactions in highly turbulent premixed methane/air flames. Part I. Flame structure characterization, Combust. Flame 162 (7) (2015) 2937–2953. 99, 105, 110, 116, 151, 154, 155, 158, 160

[19] B. Zhou, C. Brackmann, Z. Wang, Z. Li, M. Richter, M. Aldén, X.-S. Bai, Thin reaction zone and distributed reaction zone regimes in turbulent premixed methane/air flames: Scalar distributions and correlations, Combust. Flame 175 (2017) 220–236. 24, 37, 39, 42, 47, 77, 88, 99, 105, 108, 109, 110, 120, 121, 153, 154, 155, 156, 157, 158, 159, 160, 161

[20] F. O'Young, R. W. Bilger, Scalar gradient and related quantities in turbulent premixed flames, Combust. Flame 109 (4) (1997) 682–700. 24, 116, 151, 153, 154

[21] Z. S. Li, B. Li, Z. W. Sun, X. S. Bai, M. Aldén, Turbulence and combustion interaction: High resolution local flame front structure visualization using simultaneous single-shot PLIF imaging of CH, OH, and CH2O in a piloted premixed jet flame, Combust. Flame 157 (6) (2010) 1087–1096. 23, 39, 42, 47, 49, 88, 99, 105, 110, 116, 119, 120, 125, 151, 152, 153, 154

[22] T. M. Wabel, A. W. Skiba, J. E. Temme, J. F. Driscoll, Measurements to determine the regimes of premixed flames in extreme turbulence, Proc. Combust. Inst. 36 (2017) 1809–1816. 24, 25, 37, 88, 99, 114

[23] B. Roy Chowdhury, B. M. Cetegen, Experimental study of the effects of free stream turbulence on characteristics and flame structure of bluff-body stabilized conical lean premixed flames, Combust. Flame 178 (2017) 311–328. xii, xv, 17, 24, 37, 112, 115, 116, 151, 152, 153, 154

[24] R. Sankaran, E. R. Hawkes, J. H. Chen, T. Lu, C. K. Law, Structure of a spatially developing turbulent lean methane-air Bunsen flame, Proc. Combust. Inst. 31 I (2007) 1291–1298. xii, xv, 4, 17, 24, 99, 114, 115, 152, 153

[25] The interaction of high-speed turbulence with flames: Global properties and internal flame structure, Combust. Flame 157 (5) (2010) 995–1011. 24, 152, 153

[26] A. J. Aspden, M. S. Day, J. B. Bell, Turbulence-flame interactions in lean premixed hydrogen: transition to the distributed burning regime, J. Fluid Mech. 680 (2011) 287–320. 4, 22, 25, 99, 105, 110, 121, 125, 127, 128, 152

[27] A. J. Aspden, M. S. Day, J. B. Bell, Lewis number effects in distributed flames, Proc. Combust. Inst. 33 (1) (2011) 1473–1480. 25, 105, 110, 121, 127, 128, 152

[28] A. J. Aspden, M. S. Day, J. B. Bell, Turbulence-chemistry interaction in lean premixed hydrogen combustion, Proc. Combust. Inst. 35 (2) (2015) 1321–1329. 152, 153

[29] A. J. Aspden, M. S. Day, J. B. Bell, Three-dimensional direct numerical simulation of turbulent lean premixed methane combustion with detailed kinetics, Combust. Flame 166 (2016) 266–283. 125, 152

[30] A. Aspden, J. Bell, M. Day, F. Egolfopoulos, Turbulenceflame interactions in lean premixed dodecane flames, Proc. Combust. Inst. 36 (2017) 2005–2016. 24, 39, 116, 152, 153

[31] B. Savard, G. Blanquart, Broken reaction zone and differential diffusion effects in high Karlovitz n-C7H16 premixed turbulent flames, Combust. Flame 162 (5) (2015) 2020–2033. 4, 83

[32] S. Lapointe, B. Savard, G. Blanquart, Differential diffusion effects, distributed burning, and local extinctions in high Karlovitz premixed flames, Combust. Flame 162 (9) (2015) 3341–3355. xii, xv, 4, 17, 24, 25, 99, 105, 110, 114, 115, 116, 121, 125, 127, 128, 129, 152, 153

[33] L. Y. M. Gicquel, G. Staffelbach, T. Poinsot, Large Eddy Simulations of gaseous flames in gas turbine combustion chambers, Prog. Energy Combust. Sci. 38 (6) (2012) 782–817. xii, 5, 6, 8, 17, 20, 25, 144

[34] G. P. Smith, D. M. Golden, M. Frenklach, N. W. Moriarty, B. Eiteneer, M. Goldenberg, T. C. Bowman, R. K. Hanson, S. Song, W. C. Gardiner, V. V. Lissianski, Jr., Z. Qin, Gri-mech 3.0.
URL `http://www.me.berkeley.edu/gri_mech/` xii, xiii, xvii, 32, 38, 48, 88

[35] J. Luque, D. R. Crosley, LIFBASE: Database and Spectral Simulation Program (Version 2.1.1), SRI International Report MP 99-009 (1999). xii, 43

[36] N. Peters, Length scales in laminar and turbulent flames, in: E. S. Oran, J. P. Boris (Eds.), Numerical Approaches to Combustion Modeling, *Prog. in Astronautics and Aeronautics*, AIAA, Washington, DC, 1991, pp. 155–182. xvii, xxii, xxiv, 13, 17, 18, 19, 21, 22, 32

[37] F. Fuest, R. S. Barlow, J. Y. Chen, A. Dreizler, Raman/Rayleigh scattering and CO-LIF measurements in laminar and turbulent jet flames of dimethyl ether, Combust. Flame 159 (8) (2012) 2533–2562. xviii, 81, 82

[38] W. C. Gardiner, Y. Hidaka, T. Tanzawa, Refractivity of combustion gases, Combust. Flame 40 (C) (1981) 213–219. xviii, xxii, 81

[39] U.S. Energy Information Admisistration, accessed: 2017-03-30.
URL `https://www.eia.gov/` 1, 2, 3

[40] D. Mosher, A forgotten war technology could safely power earth for millions of years. here's why we aren't using it, accessed: 2017-03-02.
URL `www.businessinsider.com/thorium-molten-salt-reactors-sorensen` 2, 3

[41] National Aeronautics and Space Admisistration, accessed: 2017-04-02.
URL `https://climate.nasa.gov/` 2

[42] National Cancer Institute, accessed: 2017-04-02.
URL `https://dceg.cancer.gov/` 3

[43] J. B. Bell, M. S. Day, J. F. Grcar, M. J. Lijewski, J. F. Driscoll, S. A. Filatyev, Numerical simulation of a laboratory-scale turbulent slot flame, Proc. Combust. Inst. 31 I (2007) 1299–1307. 4

[44] E. R. Hawkes, O. Chatakonda, H. Kolla, A. R. Kerstein, J. H. Chen, A petascale direct numerical simulation study of the modelling of flame wrinkling for large-eddy simulations in intense turbulence, Combust. Flame 159 (8) (2012) 2690–2703.

[45] H. Wang, E. R. Hawkes, B. Zhou, J. H. Chen, Z. Li, M. Aldén, A comparison between direct numerical simulation and experiment of the turbulent burning velocity-related statistics in a turbulent methane-air premixed jet flame at high Karlovitz number, Proc. Combust. Inst. 36 (2017) 2045–2053. 4, 24, 39, 42, 116

[46] A. N. Kolmogorov, The Local Structure of Turbulence in Incompressible Viscous Fluid for Very Large Reynolds Numbers, Akad. Nauk SSSR Dokl. 30 (1941) 301–305. 5, 143

[47] K. K. Kuo, Principles of Combustion, John Wiley & Sons, 2005. 5, 13, 14, 47, 48, 49, 142

[48] S. B. Pope, Turbulent Flows, Cambridge Univeristy Press, 2000. 5, 6, 119, 142

[49] National Aeronautics and Space Admisistration High-End Computing Capability, accessed: 2017-04-06.
URL `www.nas.nasa.gov/hecc/resources/pleiades.html` 6, 144

[50] National Aeronautics and Space Admisistration High-End Computing Program, accessed: 2017-04-06.
URL `hec.nasa.gov/user/policies/sbus.html` 6, 145

[51] J. O. Hinze, Turbulence, McGraw-Hill, 1975. 6, 34

[52] H. Pitsch, Large-Eddy Simulation of Turbulent Combustion, Annu. Rev. Fluid Mech. 38 (1) (2006) 453–482. 6, 8

[53] T. Poinsot, D. Veynante, S. Candel, Diagrams of premixed turbulent combustion based on direct simulation, Symp. (Int.) Combust. 23 (1) (1990) 613–619. 8, 16, 17, 18, 122

[54] M. S. Sweeney, S. Hochgreb, M. J. Dunn, R. S. Barlow, The structure of turbulent stratified and premixed methane/air flames I: Non-swirling flows, Combust. Flame 159 (9) (2012) 2896–2911. 8

[55] S. M. Correa, A Review of NOx Formation Under Gas-Turbine Combustion Conditions, Combust. Sci. Technol. 87 (1993) 329–362. 9

[56] A. H. Lefebvre, Gas Turbine Combustion, Taylor & Francis, 1999. 9

[57] The GEnx Commercial Aircraft Engine, accessed: 2017-04-01.
URL `https://www.geaviation.com/commercial/engines/genx-engine` 9

[58] N. Peters, Laminar diffusion flamelet models in non-premixed turbulent combustion, Prog. Energy Combust. Sci. 10 (3) (1984) 319–339. 12, 15, 16

[59] N. Peters, Laminar flamelet concepts in turbulent combustion, Symp. (Int.) Combust. 21 (1986) 1231–1250. 12, 15, 16, 17, 18, 20, 22, 128

[60] G. Damköhler, Der Einfluss der Turbulenz auf die Flammengeschwindigkeit in Gasgemischen. Zs Electrochemie 6 (1940) 601. 16

[61] A. Klimov, Zhournal Prikladnoi Mekchaniki i Tekhnicheskoi Fiziki 3 (1963) 49. 16, 20

[62] V. L. Zimont, Theory of turbulent combustion of a homogeneous fuel mixture at high reynolds numbers, Combustion, Explosion and Shock Waves 15 (3) (1979) 305–311.

[63] K. N. C. Bray, Turbulent flows with premixed reactants, in: P. A. Libby, F. A. Williams (Eds.), Turbulent Reacting Flows, *Topics in Applied Physics*, 1980, pp. 115–183. 17, 18

[64] R. Borghi, On the structure and morphology of turbulent premixed flames, Recent Adv. Aerosp. Sci. (1985) 117–138. 17, 22

[65] R. Borghi, Prog. Energy Combust. Sci 14 (1988) 245. 17

[66] F. Williams, Analytical and numerical methods for investigation of flow fields with chemical reactions, especially related to combustion, in: A Review of Some Theoretical Considerations of Turbulent Flame Structure., Vol. 164, AGARD Conference Proceedings, 1975, pp. II 1–1. 16, 20

[67] F. Williams, Criteria for existence of wrinkled laminar flame structure of turbulent premixed flames, Combust. Flame 26 (1976) 269. 16, 20

[68] F. Williams, Combustion Theory, Addison-Wesley, 1985. 17, 18, 22

[69] F. Williams, Turbulent combustion, in: B. J. (Ed.), Mathematics of comubstion, SIAM, 1985, pp. 97–132. 17

[70] F. A. Williams, Progress in knowledge of flamelet structure and extinction, Prog. Energy Combust. Sci. 26 (4) (2000) 657–682. 17, 20, 22

[71] J. Abraham, F. A. Williams, F. V. Bracco, A discussion of turbulent flame structure in premixed charges, in: SAE Technical Paper, SAE International, 1985. 17

[72] R. Abdel-Gayed, D. Bradley, F. Lung, Combustion Regimes and the Straining of Turbulent Premixed Flames, Combust. Flame 76 (1989) 213–218. 16, 17, 18

[73] Ö. L. Gülder, Contribution of small scale turbulence to burning velocity of flamelets in the thin reaction zone regime, Proc. Combust. Inst. 31 I (2007) 1369–1375. 16, 93, 94, 128

[74] K. N. C. Bray, J. B. Moss, A unified statistical model of the premixed turbulent flame, Acta Astronautica 4 (1977) 291–319. 16

[75] K. N. C. Bray, P. A. Libby, Recent developments in the bml model of premixed turbulent combustion, in: P. A. Libby, F. A. Williams (Eds.), Turbulent Reacting Flows, Academic Press, London, 1994, pp. 127–140. 16

[76] C. Meneveau, T. Poinsot, Stretching and quenching of flamelets in premixed turbulent combustion, Combust. Flame 86 (4) (1991) 311–332. 16, 93, 94

[77] E. Hawkes, R. Cant, A flame surface density approach to large-eddy simulation of premixed turbulent combustion, Proc. Combust. Inst. 28 (1) (2000) 51–58. 93, 94

[78] S. B. Pope, The evolution of surfaces in turbulence, Int. J. Eng. Sci. 26 (5) (1988) 445–469. 93

[79] D. Veynante, L. Vervisch, Turbulent combustion modeling, Prog. Energy Combust. Sci. 28 (3) (2002) 193–266. 16, 93

[80] T. Poinsot, D. Veynante, S. Candel, Quenching processes and premixed turbulent combustion diagrams, J. Fluid Mech. 228 (1991) 561–606. 17, 18

[81] M. D. Smooke, V. Giovangigli, Formulation of the premixed and nonpremixed test problems, Springer Berlin Heidelberg, Berlin, Heidelberg, 1991, pp. 1–28. 18

[82] M. Summerfield, S. H. Reiter, V. Kebely, R. W. Mascolo, The phsical Structure of Turbulent Flames, Jet Propuls. 24 (8) (1954) 377–384. 22

[83] M. Summerfield, S. H. Reiter, V. Kebely, R. W. Mascolo, The Structure and Propagation Mechanism of Turbulent Flames in High Speed Flow, Jet Propuls. 25 (8) (1955) 377–384. 22

[84] S. B. Pope, M. S. Anand, Flamelet and distributed combustion in premixed turbulent flames, Symp. Combust. 20 (1) (1984) 403–410. 22

[85] M. S. Mansour, Y.-C. Chen, N. Peters, The reaction zone structure of turbulent premixed methane-helium-air flames near extinction, Symp. (Int.) Combust. 1 (1992) 461–468. 22

[86] Y.-C. Chen, M. S. Mansour, Simultaneous Rayleigh scattering and laser-induced CH fluorescence for reaction zone imaging in high-speed premixed hydrocarbon flames, Appl. Phys. B Lasers Opt. 64 (5) (1997) 599–605.

[87] M. S. Mansour, Y.-C. Chen, N. Peters, Highly strained turbulent rich methane flames stabilized by hot combustion products, Combust. Flame 116 (1-2) (1999) 136–153. 22

[88] A. Cavaliere, M. De Joannon, Mild combustion, Prog. Energy Combust. Sci. 30 (4) (2004) 329–366. 23

[89] A. E. E. Khalil, A. K. Gupta, Swirling flowfield for colorless distributed combustion, Appl. Energy 113 (x) (2014) 208–218. 23

[90] R. W. Bilger, S. B. Pope, K. N. C. Bray, J. F. Driscoll, Paradigms in turbulent combustion research, Proc. Combust. Inst. 30 (1) (2005) 21–42. 23

[91] J. F. Driscoll, Turbulent premixed combustion: Flamelet structure and its effect on turbulent burning velocities, Prog. Energy Combust. Sci. 34 (1) (2008) 91–134. 23, 93, 96

[92] L. P. H. De Goey, T. Plessing, R. T. E. Hermanns, N. Peters, Analysis of the flame thickness of turbulent flamelets in the thin reaction zones regime, Proc. Combust. Inst. 30 (1) (2005) 859–865. 24

[93] J. Smolke, S. Lapointe, L. Paxton, G. Blanquart, F. Carbone, A. M. Fincham, F. N. Egolfopoulos, Experimental and numerical studies of fuel and hydrodynamic effects on piloted turbulent premixed jet flames, Proc. Combust. Inst. 36 (2017) 1877–1884. 24

[94] A. J. Aspden, A numerical study of diffusive effects in turbulent lean premixed hydrogen flames, Proc. Combust. Inst. 36 (2017) 1997–2004. 24, 99, 116, 125, 152, 153

[95] A. Marshall, P. Venkateswaran, D. Noble, J. Seitzman, T. Lieuwen, Development and characterization of a variable turbulence generation system, Exp. Fluids 51 (3) (2011) 611–620. 29, 33

[96] S. G. Saddoughi, S. V. Veeravalli, Local isotropy in turbulent boundary layers at high Reynolds number, J. Fluid Mech. 268 (1994) (1994) 333–372. 33

[97] J. Mayo, W. T., A discussion of limitations and extentions of power spectrum estimation with burst-counter ldv systems., in: Proc. Second Int. Workshop on Laser Velocimetry, West Lafayette, Indiana, Purdue University, 1974, pp. 90–101. 33

[98] M. J. Tummers, D. M. Passchier, Spectral estimation using a variable window and the slotting technique with local normalization, Meas. Sci. Technol. 7 (11) (1996) 1541–1546. 33

[99] M. J. Fisher, P. O. a. L. Davies, Correlation measurements in a non-frozen pattern of turbulence, J. Fluid Mech. 18 (01) (1964) 97. 33

[100] G. Heskestad, A Generalized Taylor Hypothesis With Application for High Reynolds Number Turbulent Shear Flows 32 (4) (1965) 735.

[101] H. Wu, G. K. Patterson, Laser-Doppler measurements of turbulent-flow parameters in a stirred mixer, Chem. Eng. Sci. 44 (10) (1989) 2207–2221.

[102] S. M. Kresta, P. E. Wood, The flow field produced by a pitched blade turbine: Characterization of the turbulence and estimation of the dissipation rate, Chem. Eng. Sci. 48 (10) (1993) 1761–1774.

[103] E. S. Wernersson, C. Tragardh, Measurements and analysis of high-intensity turbulent characteristics in a turbine-agitated tank, Exp. Fluids 28 (6) (2000) 532–545.

[104] C. M. García, M. H. García, Characterization of flow turbulence in large-scale bubble-plume experiments, Exp. Fluids 41 (1) (2006) 91–101. 33

[105] C. D. Carter, S. Hammack, T. Lee, High-speed planar laser-induced fluorescence of the CH radical using the C-X(0,0) band, Appl. Phys. B Lasers Opt. 116 (3) (2014) 515–519. 35, 42, 43, 160

[106] C. D. Carter, S. Hammack, T. Lee, High-speed flamefront imaging in premixed turbulent flames using planar laser-induced fluorescence of the CH CX band, Combust. Flame 168 (2016) 66–74. 35, 42, 43

[107] P. H. Paul, H. N. Najm, Planar laser-induced fluorescence imaging of flame heat release rate, Symp. (Int.) Combust. 27 (3) (1998) 43–50. 37, 38, 39

[108] C. M. Vagelopoulos, J. H. Frank, J. Jeffries, F. Dinkelacker, An experimental and numerical study on the adequacy of CH as a flame marker in premixed methane flames, Proc. Combust. Inst. 30 I (1) (2005) 241–249. 39, 42

[109] A. Fayoux, K. Zähringer, O. Gicquel, J. C. Rolon, C. Schulz, S. Kaiser, Experimental and numerical determination of heat release in counterflow premixed laminar flames, Proc. Combust. Inst. 30 I (2005) 251–257.

[110] I. A. Mulla, A. Dowlut, T. Hussain, Z. M. Nikolaou, S. R. Chakravarthy, N. Swaminathan, R. Balachandran, Heat release rate estimation in laminar premixed flames using laser-induced fluorescence of CH2O and H-atom, Combust. Flame 165 (2016) 373–383. 39

[111] S. Böckle, J. Kazenwadel, T. Kunzelmann, D.-I. Shin, C. Schulz, J. Wolfrum, Simultaneous single-shot laser-based imaging of formaldehyde, OH, and temperature in turbulent flames, Proc. Combust. Inst. 28 (1) (2000) 279–286. 39, 47, 77, 88

[112] M. Röder, T. Dreier, C. Schulz, Simultaneous measurement of localized heat release with OH/CH 2O-LIF imaging and spatially integrated OH* chemiluminescence in turbulent swirl flames, Appl. Phys. B Lasers Opt. 107 (2012) 611–617.

[113] M. Röder, T. Dreier, C. Schulz, Simultaneous measurement of localized heat release with OH/CH 2O-LIF imaging and spatially integrated OH* chemiluminescence in turbulent swirl flames, Proc. Combust. Inst. 34 (2013) 3549–3556.

[114] B. O. Ayoola, R. Balachandran, J. H. Frank, E. Mastorakos, C. F. Kaminski, Spatially resolved heat release rate measurements in turbulent premixed flames, Combust. Flame 144 (2006) 1–16. 38, 39

[115] J. Kariuki, A. Dowlut, R. Yuan, R. Balachandran, E. Mastorakos, Heat release imaging in turbulent premixed methane-air flames close to blow-off, Proc. Combust. Inst. 35 (2) (2015) 1443–1450. 112

[116] R. Yuan, J. Kariuki, A. Dowlut, R. Balachandran, E. Mastorakos, Reaction zone visualisation in swirling spray n-heptane flames, Proc. Combust. Inst. 35 (2) (2015) 1649–1656.

[117] B. Coriton, J. H. Frank, A. Gomez, Interaction of turbulent premixed flames with combustion products: Role of stoichiometry, Combust. Flame 170 (2016) 37–52. 37, 39, 112

[118] J. B. Jeffries, D. R. Crosley, I. J. Wysong, G. P. Smith, Laser-Induced Fluorescence Detection of HCO in a Low-Pressure Flame, Symp. (Int.) Combust. 23 (3) (1990) 1847–1854. 38

[119] H. N. Najm, P. H. Paul, C. J. Mueller, P. S. Wyckoff, On the Adequacy of Certain Experimental Observables as Measurements of Flame Burning Rate, Combust. Flame 113 (1998) 312–332. 38, 39, 42

[120] H. N. Najm, O. M. Knio, P. H. Paul, P. Wyckoff, A Study of Flame Observables in Premixed Methane - Air Flames, Combust. Sci. Technol. 140 (April) (1998) 369–403. 38

[121] Z. M. Nikolaou, N. Swaminathan, Heat release rate markers for premixed combustion, Combust. Flame 161 (12) (2014) 3073–3084. 38, 39

[122] B. Zhou, J. Kiefer, J. Zetterberg, Z. Li, M. Aldén, Strategy for PLIF single-shot HCO imaging in turbulent methane/air flames, Combust. Flame 161 (6) (2014) 1566–1574. 39

[123] S.-H. Lee, C.-I. Chen, Axis switching in the (B)over-tilde(2)A'-(X)over-tilde(2)A' transition of HCO and fluorescence lifetimes of the (B)over-tilde(2)A'(0,0,0) rotational states, J. Chem. Phys. 105 (1996) 2583–2590. 39

[124] R. L. Gordon, A. R. Masri, E. Mastorakos, Simultaneous Rayleigh temperature, OH- and CH2O-LIF imaging of methane jets in a vitiated coflow, Combust. Flame 155 (2008) 181–195. 39, 47, 77, 88

[125] C. Brackmann, J. Nygren, X. Bai, Z. Li, H. Bladh, B. Axelsson, I. Denbratt, L. Koopmans, P. E. Bengtsson, M. Aldén, Laser-induced fluorescence of formaldehyde in combustion using third harmonic Nd:YAG laser excitation 59 (14) (2003) 3347–3356. 40

[126] B. Zhou, Q. Li, Y. He, P. Petersson, Z. Li, M. Aldén, X. S. Bai, Visualization of multi-regime turbulent combustion in swirl-stabilized lean premixed flames, Combust. Flame 162 (7) (2015) 2954–2958. 42, 105, 110, 112

[127] J. Kiefer, Z. S. Li, J. Zetterberg, X. S. Bai, M. Aldén, Investigation of local flame structures and statistics in partially premixed turbulent jet flames using simultaneous single-shot CH and OH planar laser-induced fluorescence imaging, Combust. Flame 154 (4) (2008) 802–818.

[128] S. A. Filatyev, J. F. Driscoll, C. D. Carter, J. M. Donbar, Measured properties of turbulent premixed flames for model assessment, including burning velocities, stretch rates, and surface densities, Combust. Flame 141 (1-2) (2005) 1–21. 95

[129] M. Tanahashi, S. Murakami, G. M. Choi, Y. Fukuchi, T. Miyauchi, W. Meier, A. K. Agrawal, Simultaneous CH-OH PLIF and stereoscopic PIV measurements of turbulent premixed flames, Proc. Combust. Inst. 30 I (1) (2005) 1665–1672.

[130] A. Johchi, Y. Naka, M. Shimura, M. Tanahashi, T. Miyauchi, Investigation on rapid consumption of fine scale unburned mixture islands in turbulent flame via 10 kHz simultaneous CH-OH PLIF and SPIV, Proc. Combust. Inst. 35 (3) (2015) 3663–3671.

[131] P. Versailles, G. M. G. Watson, A. C. A. Lipardi, J. M. Bergthorson, Quantitative CH measurements in atmospheric-pressure, premixed flames of C1-C4 alkanes, Combust. Flame 165 (2016) 109–124. 42, 122

[132] A. W. Skiba, T. M. Wabel, C. D. Carter, S. D. Hammack, J. E. Temme, T. Lee, J. F. Driscoll, Reaction layer visualization: A comparison of two PLIF techniques and advantages of kHz-imaging, Proc. Combust. Inst. 36 (2017) 4593–4601. 42, 45, 93

[133] J. B. Jeffries, R. A. Copeland, D. R. Crosley, Transition probabilities in the C2Σ+-X2Π system of CH, J. Quant. Spectrosc. Radiat. Transf. 37 (1987) 419–423. 42, 43

[134] R. A. Patton, K. N. Gabet, N. Jiang, W. R. Lempert, J. A. Sutton, Multi-kHz temperature imaging in turbulent non-premixed flames using planar Rayleigh scattering, Appl. Phys. B Lasers Opt. 108 (2) (2012) 377–392. 47, 77, 78

[135] T. A. McManus, M. J. Papageorge, F. Fuest, J. A. Sutton, Spatio-temporal characteristics of temperature fluctuations in turbulent non-premixed jet flames, Proc. Combust. Inst. 35 (2) (2015) 1191–1198. 47, 77

[136] A. C. Eckbreth, Laser Diagnostics for Combustion Temperature and Species, Gordon and Breach Publishers, 1996. 47, 77

[137] D. Most, A. Leipertz, Simultaneos two-dimensional flow velocity and gas temperature measurements by use of a combined particle image velocimetry and filtered Rayleigh scattering technique, Appl. Opt. 40 (30) (2001) 5379–5387. 47

[138] F. Chazallet, J. Glasser, Theoretical bases and measurement of the mtf of integrated image sensors, in: Granger EM, Baker LR (eds) Image quality: An overview., P Soc Photo-Opt Inst, 1985, pp. 549:131–144. 53, 67, 84

[139] N. T. Clemens, Flow imaging, in: Encyclopedia of Imaging Science and Technology, John Wiley and Sons, Inc., 2002. 54, 57, 67, 70

[140] G.-H. Wang, N. Clemens, Effects of imaging system blur on measurements of flow scalars and scalar gradients, Exp. Fluids 37 (2) (2004) 194–205. 53, 54, 67, 70, 71, 84

[141] S. Osher, R. Fedkiw, Level Set Methods and Dynamic Implicit Surfaces, Springer, 2003. 59

[142] F. Meyer, Topographic distance and watershed lines, Signal Processing 38 (1) (1994) 113–125. 60

[143] MATLAB, version 9.4 (R2016a), The MathWorks Inc., Natick, Massachusetts, 2016a. 60, 61

[144] R. B. Miles, W. R. Lempert, J. N. Forkey, Laser rayleigh scattering, Meas. Sci. Technol. 12 (2001) R33–R51. 77

[145] C. D. Cater, Laser-based rayleigh and mie scattering methods, in: J. A. Schetz, A. E. Fuhs (Eds.), Handbook of Fluid Dynamics and Fluid Machinery, Wiley, New York, 1996, pp. 1078–1093. 77, 80, 82

[146] J. A. Sutton, J. F. Driscoll, Rayleigh scattering cross sections of combustion species at 266, 355, and 532 nm for thermometry applications., Opt. Lett. 29 (22) (2004) 2620–2622. 79

[147] B. Savard, B. Bobbitt, G. Blanquart, Structure of a high Karlovitz n-C7H16 premixed turbulent flame, Proc. Combust. Inst. 35 (2) (2015) 1377–1384. 83

[148] H. Wang, R. E. Hawkes, J. H. Chen, Direct numerical simulation of an experimental stratified turbulent methane–air premixed jet flame at high karlovitz number, private communications, April 2017. 83

[149] J. R. Osborne, S. A. Ramji, C. D. Carter, S. Peltier, S. Hammack, T. Lee, A. M. Steinberg, Simultaneous 10 kHz TPIV, OH PLIF, and CH2O PLIF measurements of turbulent flame structure and dynamics, Exp. Fluids 57 (5) (2016) 1–19. 88

[150] T. M. Wabel, A. W. Skiba, J. F. Driscoll, Turbulent burning velocity measurements: Extended to extreme levels of turbulence, Proc. Combust. Inst. 36 (2017) 1801–1808. 88, 128

[151] K. N. Bray, R. S. Cant, Some Applications of Kolmogorov's Turbulence Research in the Field Of Combustion, Proc. R. Soc. Lond. 434 (1991) 217–240. 93, 94, 95

[152] I. Shepherd, Flame surface density and burning rate in premixed turbulent flames, Symp. (Int.) Combust. 26 (1) (1996) 373–379. 93, 94

[153] W. L. Roberts, J. F. Driscoll, M. C. Drake, L. P. Goss, Images of the quenching of a flame by a vortex-To quantify regimes of turbulent combustion, Combust. Flame 94 (1993) 58–69. 122

[154] A. Lipatnikov, Fundamentals of Premixed Turbulent Combustion, CRC Press, 2012. 127

[155] Ö. L. Gülder, G. J. Smallwood, R. Wong, D. R. Snelling, R. Smith, B. M. Deschamps, J. C. Sautet, Flame front surface characteristics in turbulent premixed propane/air combustion, Combust. Flame 120 (2000) 407–416. 128

[156] Ö. L. Gülder, G. J. Smallwood, Flame Surface Densities in Premixed Combustion At Medium To High Turbulence Intensities, Combust. Sci. Technol. 179 (2007) 191–206. 128

[157] Top500 List – November 2016, accessed: 2017-04-02.
URL `https://www.top500.org/list/2016/11/` 145

[158] Z. S. Li, J. Kiefer, J. Zetterberg, M. Linvin, a. Leipertz, X. S. Bai, M. Aldén, Development of improved PLIF CH detection using an Alexandrite laser for single-shot investigation of turbulent and lean flames, Proc. Combust. Inst. 31 (2007) 727–735. 160

[159] J. Kiefer, F. Ossler, Z. S. Li, M. Aldén, Spectral interferences from formaldehyde in CH PLIF flame front imaging with broadband B-X excitation, Combust. Flame 158 (3) (2011) 583–585. 160